Onset of Dynamic Wetting Failure in the Presence of Surfactants

A DISSERTATION
SUBMITTED TO THE FACULTY OF THE GRADUATE SCHOOL
OF THE UNIVERSITY OF MINNESOTA
BY

Chen-Yu Liu

IN PARTIAL FULFILLMENT OF THE REQUIREMENTS
FOR THE DEGREE OF
DOCTOR OF PHILOSOPHY IN CHEMICAL ENGINEERING

Advisor: Satish Kumar

June, 2017

Acknowledgements

There are so many people that I would like to thank for their support during the graduate school journey. I sincerely thank my advisor, Prof. Satish Kumar, for his patient guidance and constructive feedback on my writings and presentations. A rigorous attitude toward conducting scientific research is the most important lesson I learnt from him, which I believe will continuously benefit me in the rest of my life. I am also grateful to him for his suggestions and help during my job searching process. I thank Prof. Marcio S. Carvalho for the valuable insights he provided into the finite element codes and research directions. His guidance and input helped me overcome the learning curve of the in-house CFD software COAT. I am grateful to Prof. Alon McCormick and Prof. Jeff Derby for their suggestions on my thesis work and for serving on my graduate committee.

I thank the Donors of the American Chemical Society Petroleum Research Fund for initial support of my work, and the National Science Foundation for subsequent support. I am grateful for resources provided by this department and the University of Minnesota. During my PhD I have been fortunate to participate in several workshops and short courses hosted by the Industrial Partnership for Research in Interfacial and Materials Engineering (IPRIME), Minnesota Supercomputing Institute, and College of Science and Engineering. From these events, I have gained knowledge and skills that help me conduct better research. In addition, through the annual IPRIME meeting, I have connected with people from both academia and industry and obtained their useful feedback on my research.

I consider myself lucky to have worked with great colleagues in my research group, including Dr. Eric Vandre, Dr. Aruna Ramkrishnan, Dr. Sarit Dutta, Dr. Leonardo Espin, Dr. Joonsik Park, Weihua Li, Chung-Hsuan Huang, Truong Pham, Jyun-Ting Wu,

Gokul Hariharan, Chance Parrish, Panayiotis Kolliopoulos, and Vasileios Charitatos. I really enjoy our discussions about anything such as science, movies, course work, and sports. I would like to express my gratitude to Dr. Eric Vandre for his inspirational discussions and support for my research projects. He introduced to me the experimental equipment in the coating lab and finite element codes when I first joined this group. I also thank him for the solid foundation he built for my project on wetting failure and the 3M PET substrates he provided for my coating experiments.

My family has played an important role during my graduate studies. Our weekly Skype chats have significantly reduced my homesickness and enabled me to focus and deal with challenges in graduate school. I am lucky to have my in-laws be part of this journey. Especially, I am grateful for the Taiwanese snacks they brought when they visited Minneapolis in summer 2016. Finally, I would like to thank my incredible wife, Cha-Jung Chen, for her endless support and love. We have made it through the long distance relationship and lots of difficulties in life. I cherish every moment with you and look forward to our life-long journey.

Dedication

To my dearest parents, Chang-Chi Liu and Hsiu-Chun Cheng, and my wonderful wife, Cha-Jung Chen.

Abstract

Wetting phenomena are omnipresent in nature and play an important role in various industries. During a dynamic wetting process, an ambient fluid is displaced by another one (the wetting fluid) on a solid surface. Studies have shown that dynamic wetting fails when the process speed exceeds a certain critical value. In the coating industry, wetting failure leads to air entrainment which degrades product quality and thus limits the production rate. Therefore, dynamic wetting failure has attracted the attention of many researchers due to its industrial significance.

Surfactant molecules are common additives in coating liquids due to their special nature. They are often used as wetting agents to reduce surface tension and enhance wetting of the coating liquids. Despite the wide usage of surfactants in coating liquids, relatively little is known about the influence of surfactants on dynamic wetting failure in coating processes.

The objective of this thesis is to advance the fundamental understanding of the influence of surfactants on dynamic wetting failure. A hydrodynamic model is developed to describe the displacement of a receding fluid by an advancing fluid in a rectangular channel and a curtain coating geometry. Numerical results show that Marangoni stresses resulting from surfactant concentration gradients along the interface promote the onset of dynamic wetting failure due to the thinning of the receding phase between the fluid interface and the solid substrate. In a study on curtain coating, numerical results show that hydrodynamic assist mainly arises from the hydrodynamic pressure generated by the inertia of the impinging curtain. This pressure leads to a strong capillary-stress gradient that pumps air away from the DCL and thus increases the critical substrate speed for wetting failure.

A complementary experimental study is also conducted where a solid substrate is driven through a tank filled with surfactant solutions. It is found that the critical substrate speeds associated with the onset of wetting failure in surfactant solutions are increased when surfactant concentration increases. The comparisons between numerical and experimental results shed light into the mechanisms through which surfactants influence dynamic wetting failure. For the more viscous solutions used in this work,

the change in the critical speed as surfactant concentration increases can be explained by accounting for the decrease in equilibrium surface tension and static contact angle when surfactants are present. However, for the lowest viscosity liquid, the comparison suggests other surfactant-induced mechanisms (e.g., Marangoni stresses) may play a more important role.

Contents

List of Tables

List of Figures

Chapter 1

Introduction

Dynamic wetting is a common phenomenon in everyday life and industrial operations, where an ambient fluid (often air) is displaced by a liquid on a solid surface. Examples of dynamic wetting range from the daily task of dishwashing to industrial coating processes [1]. In particular, coating flows rely heavily on steady dynamic wetting to uniformly deposit a liquid on a moving substrate. However, dynamic wetting fails at a certain critical substrate speed. This is accompanied by a change in flow from steady two-dimensional (2D) (Figure 1.1(a)) to unsteady three-dimensional (3D) (Figure 1.1(b)). In the case where a liquid displaces air on the substrate, wetting failure leads to air entrainment and a sawtooth-shaped three-phase wetting line (Figure 1.1(b)). This can be detrimental for coating processes since trapped air can degrade product quality [2]. Therefore, understanding the mechanisms of wetting failure and finding ways to delay the onset of wetting failure are of great industrial significance.

Surfactant molecules are common additives in coating liquids. They tend to concentrate at interfaces and locally lower surface tension, the physical property that determines the shape of an interface [1]. Surfactants can freely transport along the interface through diffusion (i.e., molecular motion) and convection (i.e., bulk motion of fluid) and exchange between the interface and the bulk solution. Surfactants in the bulk can also agglomerate into groups (called micelles) when the concentration is above a critical value. In addition, if surfactant concentrations at interfaces are not uniform, surface-tension gradients arise. The resulting tension gradients drive a so-called Marangoni flow whose direction is from regions of low to high surface tension (an example of this

is the "tears" that form at the inner wall of a glass of wine) [3]. Due to these complex dynamics, surfactants have a non-trivial but poorly understood influence on the onset of wetting failure.

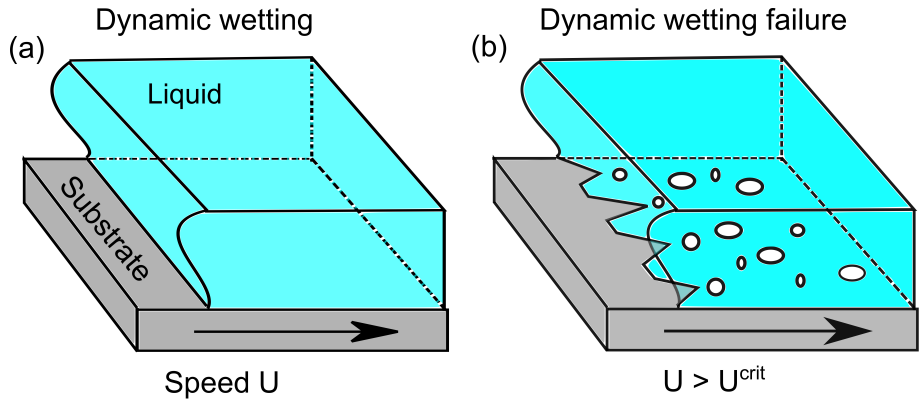

Figure 1.1: Schematics of dynamic wetting and dynamic wetting failure. During dynamic wetting, the flow remains two-dimensional (2D) and steady. It becomes unsteady and three-dimensional (3D) when dynamic wetting failure occurs ($U > U^{crit}$). The incomplete displacement results in air entrainment; air bubbles break off from the serrated three-phase junction.

The objective of this thesis is to develop a fundamental understanding of the influence of surfactants on dynamic wetting failure through experimental and computational approaches. Systematic modeling work examining insoluble and soluble surfactants demonstrates the possible mechanisms through which surfactants influence dynamic wetting failure. Experimental studies are conducted to complement the model predictions. The comparisons between modeling and experimental results shed light into the role of surfactant dynamics in coating flows.

The modeling work focuses on fluid displacements in two geometries that are common in the coating industry (Figure 1.2). First, we consider fluid displacement in a rectangular channel where the top plate is stationary and bottom substrate moves to the right at speed U (Figure 1.2(a)). This geometry is motivated by plunging tape experiments (i.e., a solid substrate plunging into a liquid bath) which have been widely used to experimentally study dynamic wetting failure [4, 5, 6, 7, 8, 9].

The second geometry is curtain coating where liquid is extruded from an elevated die onto a moving substrate, forming a film with uniform thickness downstream (Figure

1.2(b)). Due to its ability to achieve high substrate speeds, curtain coating has became a popular method for mass production [10] and has attracted the attention of many investigators [11, 12, 13, 14]. However, current models mainly study the dynamics of curtain coating flows in the dynamic wetting state [13, 15]. In this thesis, the mechanism of wetting failure and hydrodynamic assist in curtain coating (i.e., a phenomenon that describes the assist of dynamic wetting by the flow of the impinging liquid curtain) are studied (Chapter 4).

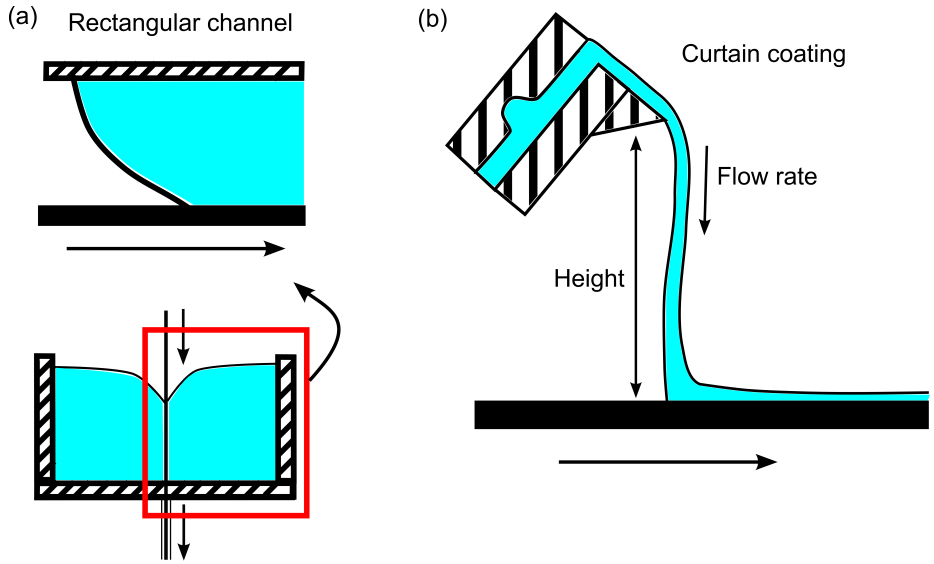

Figure 1.2: Schematics of (a) the rectangular channel and (b) curtain coating geometries used in this thesis.

Although this work is mainly motivated by coating processes, the results from this work provide insight into a wide range of applications where fluid displacement occurs in the presence of surfactants. For example, respiratory stress syndrome, a disease commonly present in premature neonates, relies on surfactants to reopen the pulmonary airways [16, 17]. Surfactants stabilize droplet interface in microfluidics which has a great potential for many applications in biotechnology [18]. In enhanced oil recovery, surfactants are used to reduce the interfacial tension so that less energy is required to recover the oil in porous geological structures [19, 20].

The following sections of this chapter provide a brief literature review related to the results presented in this thesis and a thesis overview. Chapter 1.1 covers wetting

fundamentals, including wetting states, contact angle, and fluid slip. Chapter 1.2 reveals important features of surfactants such as their property, dynamics and influence on air entrainment from prior experimental observations. Chapter 1.3 provides an overview of this thesis.

1.1 Wetting Fundamentals

1.1.1 Dynamic Wetting and The Onset of Dynamic Wetting Failure

Coating is a process where liquid layers are deposited on a substrate. The liquid films undergo solidification processes (e.g., drying or curing) and become solid films that provide desirable surface properties to the substrate. Coating processes can be found in many industries such as food, photovoltaics, and furniture and decoration. The coating industry has a large market size and keeps growing. In fact, the global market for paints and coatings reached $129 billion in 2015 and is expected to grow from nearly $132.2 billion in 2016 to $164.1 billion in 2021 [21].

Fluid displacement is a key phenomenon shared by liquid coating operations, where one fluid is displaced by another immiscible fluid on the solid substrate. The three-phase junction, often called the wetting line or contact line, is the place where fluid displacement occurs. Dynamics near the contact line have a strong influence on the profile of the fluid interface, leading to variations in the apparent contact angle θ_M, a key parameter characterizing the process of fluid displacement [9, 7, 2].

From prior experimental studies, three wetting states are observed when varying the substrate speed U: static wetting, steady dynamic wetting, and dynamic wetting failure. Since fluid displacement is sensitive to the fluid properties (e.g., liquid viscosity μ and surface tension σ), the capillary number $Ca = \mu U/\sigma$ is introduced to indicate the ratio between the viscous and surface-tension forces acting on the contact line, as shown in Figure 1.3.

In the static-wetting state (Figure 1.3(a)), the substrate is immobile ($Ca = 0$) and the system is at equilibrium. The fluid interface touches the substrate at the static contact line (SCL) and forms a well-defined contact angle, static contact angle θ_s, which is determined by the balance between interfacial tensions (i.e., at liquid-air, air-solid, and liquid-solid interfaces). Note that at this state the apparent angle is the same as

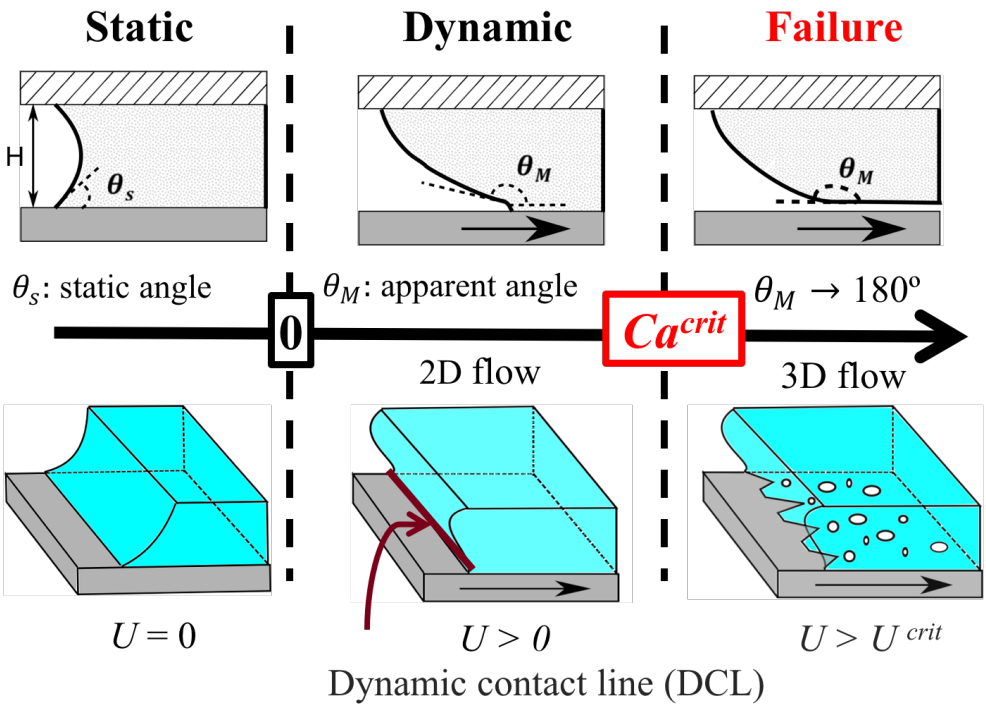

Figure 1.3: Schematics of the wetting states as a function of the capillary number Ca with side (top row) and 3D views (bottom row). The fluid interface can be characterized by a static contact angle θ_s when $Ca = 0$, and by an apparent contact angle θ_M when $Ca \neq 0$. Dynamic wetting failure occurs when the substrate speed is beyond a critical value of Ca (Ca^{crit}). At this wetting state $\theta_M \rightarrow 180^o$ and the dynamic contact line (DCL) becomes serrated with air bubbles breaking off from the tips of air vees.

θ_s. In the dynamic-wetting state (finite value of Ca), the liquid steadily displaces the air as the substrate moves at a speed U. The contact line at the wetting front is called thedynamic contact line (DCL) or dynamic wetting line, as shown in Figure 1.3(b). Due to the substrate motion, the fluid interface is elongated, resulting in the apparent contact angle θ_M (different from θ_s). Note that θ_M is also called a dynamic contact angle or macroscopic contact angle in the literature [22, 23].

As Ca increases, the fluid interface is further elongated and the value of θ_M increases. However, experimental observations show that a critical capillary number $Ca^{crit} = \mu U^{crit}/\sigma$ (associating with the critical substrate speed U^{crit}) sets an upper

limit to the steady dynamic wetting [2, 24, 25] When $Ca > Ca^{crit}$, the flow configuration changes from steady two-dimensional (2D) to unsteady three-dimensional (3D) [26, 7, 8]. Dynamic wetting failure occurs when $\theta_M \approx 180^o$ and the DCL spontaneously breaks into two or more air vees, leading to a sawtooth meniscus (Figure 1.3(c)). Flow instability promotes an intermittent entrainment of air bubbles through the tip of the air vees, leading to non-uniform coverage of coating liquid on the substrate. This causes irregularities in the solidified coating films and thus poses challenges to high-speed coating processes.

Although experimental observations of dynamic wetting failure have been widely reported [7, 8, 9, 27, 28], the mechanism of dynamic wetting failure remained only partially understood [6, 29, 30] until recent studies by Vandre and coworkers [23, 31, 26, 32]. A mechanism of dynamic wetting failure for high-speed fluid displacement was proposed by them [31, 32]. During steady dynamic wetting, capillary stresses developed by the fluid interface pump the air away from the DCL. Dynamic wetting failure occurs when the fluid interface fails to provide the stresses needed to remove the air. Their model predictions of critical speeds U^{crit} agree well with experimental values [26].

Although dynamic wetting has been studied over many years, the precise mechanism of it remains a subject of active debate. There are several dynamic wetting theories in the literature: hydrodynamic theory (i.e., changes in θ_M results from viscous bending of the fluid interface), the diffuse-interface model (i.e., dynamic wetting results from the transport of fluid molecules through an interfacial layer with finite thickness), the interface-formation model (i.e., surface-tension gradients arising from the creation of solid-liquid interface can influence the contact angle at the DCL), and molecular-kinetic theory (i.e., wetting is a consequence of kinetics of molecular adsorption/desorption). This thesis work uses hydrodynamic theory since it has been used to successfully predict the onset of dynamic wetting failure in prior work [23, 31, 26].

1.1.2 Contact Angle

A contact angle is formed at the contact line when the fluid interface intersects the substrate. This angle serves as an important parameter characterizing the wetting states and the substrate properties. To measure the contact angle, a direct visualization of the contact line is carried out through a microscope. Depending on the resolution

of optical measurements, there are two types of contact angles [22]. The observed interface angle, referred to as apparent contact angle θ_{ap} or macroscopic contact angle θ_M in the literature, is measured at some distance from the contact line, as illustrated in Figure 1.4. Instead, the angle in the immediate proximity to the contact line is called the microscopic contact angle θ_{mic}, which can not be observed (i.e., below the optical resolution of a microscope ($\approx \mu m$)) [22, 33] (Figure 1.4). Note that in the static-wetting state (i.e., $U = 0$), there is no interface bending by the substrate, so $\theta_{ap} = \theta_{mic} = \theta_s$.

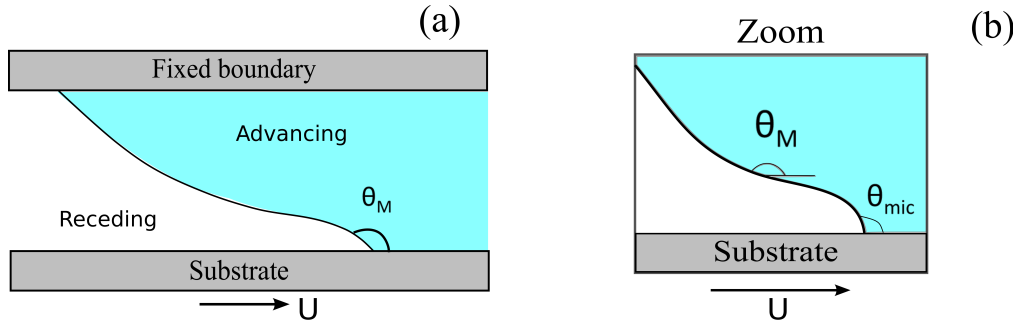

Figure 1.4: Schematics of the macroscopic and microscopic contact angles along a fluid interface. (a) The fluid interface bends in the direction of substrate motion and forms a macroscopic contact angle θ_M. (b) Enlarged view of the fluid interface near the contact line, showing the difference between θ_M and the microscopic contact angle θ_{mic}.

Prior experiemental studies show that θ_M increases with the substrate speed (see Figure 1.3 in Sec. 1.1) [5, 6, 7, 8, 9]. This behavior is qualitatively described by the hydrodynamic theory, which attributes the behavior to the viscous bending of the fluid interface resulting from the drag of the substrate [2]. Based upon the hydrodynamic theory, analytical descriptions for θ_M have been developed by asymptotic analysis [34, 35] and lubrication approximation [36, 37].

$$\theta_M^3 = \theta_{mic}^3 - 9Ca\ ln(\lambda_{cox}), \tag{1.1}$$

where Ca is the capillary number and $\lambda_{cox} = l_{mic}/l_M$ represents the ratio between the microscopic l_{mic} and macroscopic l_M length scales of the wetting system. Very often, λ_{cox} is treated as an adjustable parameter to fit experimental observations of θ_M as Ca increases [31, 22, 38]. Equation (1.1) is limited to low-speed dynamic wetting with slowly varying interface angles ($Ca << 1$), but it clearly shows that θ_M increases

with Ca (note that $ln(\lambda_{cox})$ is negative). Note that equation (1.1) is often reffered to as the Cox-Voinov law [39], and it has laid a foundation for later theoretical work [36, 40, 37, 41, 42].

As can be seen in (1.1), the description of θ_M involves the microscopic contact angle θ_{mic}. In fact, the specification of θ_{mic} as a boundary condition is required since θ_{mic} is governed by intermolecular forces which can not be described by continuum fluid mechanics [22]. Generally, the microscopic angle may depend on the wetting velocity and material properties of the system, such that $\theta_{mic} = \theta_{mic}(\theta_s, U, \mu, \sigma, ...)$. Although debate remains over the choice of the constitutive equation [43, 2, 22, 44], the simplest and most common approach is to set the microscopic contact angle equal to the static contact angle ($\theta_{mic} \approx \theta_s$) since θ_s serves as a leading-order approximation [35, 45, 43]. Prior studies on dynamic wetting failure have shown that modeling results based on this approximation are in good agreement with experimental observations [23, 31, 26].

1.1.3 Fluid Slip

Additional attention is needed when modeling contact-line motion. When the no-slip boundary condition is applied at the contact line, the viscous stresses and the rate of energy dissipation show non-integrable singularities at the contact line [46, 43]. This suggests that fluid elements at the contact line experience an infinite force because fluid elements need to match the velocity at the fluid interface and the contact line. In other words, the fluid velocity is multi-valued at the contact line, which has no physical meaning [47].

To avoid non-integrable singularities, the no-slip boundary condition postulated at fluid/solid boundaries needs to be relaxed. A common model approach is to allow fluid near the contact line to slip, meaning that fluid adopts a velocity different from the substrate's. A Navier-slip boundary condition is commonly used to describe the fluid slip behavior [48, 49, 46, 39].

$$u - U = l_{slip}\frac{\partial u}{\partial y}, \tag{1.2}$$

where u is the fluid velocity, du/dy is the shear stress at the substrate, and y is the Cartesian coordinate normal to the substrate. The coefficient l_{slip} corresponds to the slip length that determines the magnitude of fluid slip. Equation 1.2 shows that the

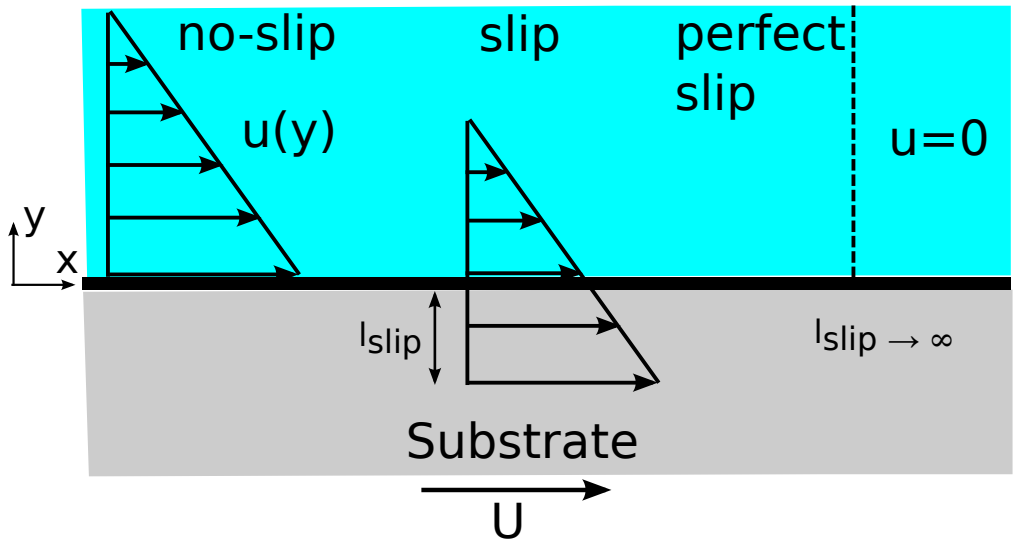

Figure 1.5: Illustration of varying degrees of fluid slip along a moving substrate.

fluid velocity near the contact line is proportional to the shear stress, and the boundary condition recovers the no-slip condition when the slip length vanishes (i.e., $u = U$ if $l_{slip} = 0$). Note that in the modeling work, the slip length is often scaled by a macroscopic length scale L, resulting in the dimensionless slip length $\lambda = l_{slip}/L$.

The slip length l_{slip} can be viewed as the fictitious distance below the surface where the no-slip boundary condition would be satisfied, as illustrated in Figure 1.5. From experimental measurements, typical value of l_{slip} is in the range of 10 nm to 1 μm [50, 51]. Although it is found that the value of l_{slip} depends on surface roughness [52, 53], entrained gaseous films [30, 29, 54], and shear rate [55, 56, 53], how these factors influence fluid slip remains inconclusive. As a result, l_{slip} in hydrodynamic slip models (i.e., models including a slip law near the contact line) is often treated as an adjustable parameter [23].

Although other forms of slip conditions exist [57], it is found that the macroscopic wetting dynamics are insensitive to the exact form of velocity functions used but mainly depend on the magnitude of the dimensionless slip length $\lambda = l_{slip}/L$ [48]. Recent studies demonstrated that predictions from the hydrodynamic model with the slip condition (1.2) are in good agreement with experimental observations of dynamic wetting failure [23, 26], suggesting that (1.2) may serve as a general slip boundary condition in wetting

processes [43].

1.2 Surfactants

1.2.1 Dynamics

Surfactants are amphiphilic molecules (i.e., they have a hydrophilic headgroup and a hydrophobic tail) which preferentially concentrate at interfaces, and therefore, change the local physical properties, like reducing the interfacial tension. When surfactant concentration at the interface is not uniform, interfacial tension gradients arise, leading to so-called *Marangoni streeses* directing from low-surface-tension to high-surface-tension regions [3]. Marangoni stresses can drive additional flows in the bulk fluid, resulting in various surfactant-induced phenomena [3, 58, 59, 60, 18]. Due to their amphiphilic property, surfactants are found in industrial areas related to detergents [61], cosmetics [62], pharmaceuticals [17], and coatings [63, 64].

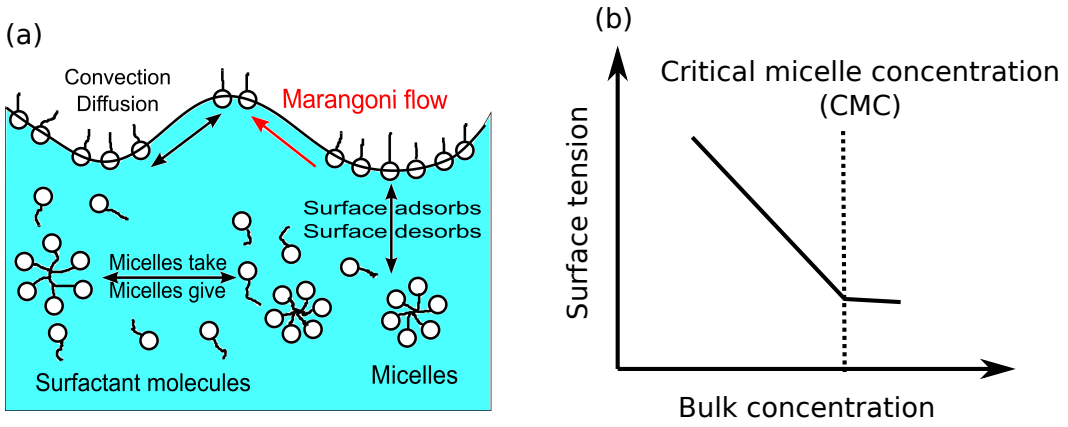

Figure 1.6: (a) Surfactant actions at the fluid interface and in the bulk solution. Surfactant molecules can adsorb and desorb between the bulk and the fluid interface. They can also transport along the interface, and when surfactant concentration gradients appear surface tension gradients will induce Marangoni flow. Surfactant molecules can exchange with micelles in solution. (b) Schematic of the equilibrium surface tension plotted as a function of bulk surfactant concentration. The critical micelle concentration corresponds to the concentration where the slope of the surface-tension curve changes.

In the bulk phase, surfactants can aggregate into micelles when the bulk concentration is above the critical micelle concentration (CMC) (Figure 1.6(a)). The CMC is usually determined by measuring the equilibrium surface tension as a function of bulk surfactant concentrations. The value of the CMC corresponds to the point where the slope of the surface-tension curve changes as the concentration increases, as illustrated in Figure 1.6(b) [65]. Depending on the structure of the surfactant molecules and the solution conditions (e.g., co-solutes and temperature) , the CMC can vary by orders of magnitude [65, 66, 67, 68]. In addition, surfactant aggregates can adopt different configurations (e.g., layers or cylinders) based on the molecular geometry and concentration [68].

As mentioned above, surfactant molecules dissolved in liquid tend to adsorb at the interface, forming a monolayer at the interface and decreasing the surface tension. To model wetting processes in the presence of surfactants, in addition to the surfactant transport equation at the interface, one would need a surface equation of state that relates the surfactant concentration at the interface to the surface tension. Depending on the bulk concentration and solute-solvent interactions, there are a number of surface equations of state corresponding to various adsorption isotherms (e.g., Henry, Langmuir, and Frumkin isotherms) [69, 65]. However, for simplicity many modeling studies adopt a dilute assumption with the surface tension being linearly dependent on surfactant concentration [70, 71, 72].

When a fresh interface is created, surfactant molecules in the bulk will transfer from the bulk to the interface in order to restore the adsorption equilibrium. The transport of surfactants is governed by a two-step process (Figure 1.7): (1) the adsorption/desorption of molecules between the surface layer and the layer immediately below it (i.e., the subsurface layer); (2) the transport of molecules between the subsurface and the bulk. In the literature two types of models have been proposed to describe the process, one is diffusion-controlled and the other is kinetic-controlled. These models involve several adjustable parameters (e.g., diffusion coefficient, adsorption and desorption rate constants) whose values are obtained by fitting the experimental data of surface tension measurements. For more extensive review of the dynamic adsorption models, one can refer to [69, 73, 74, 65].

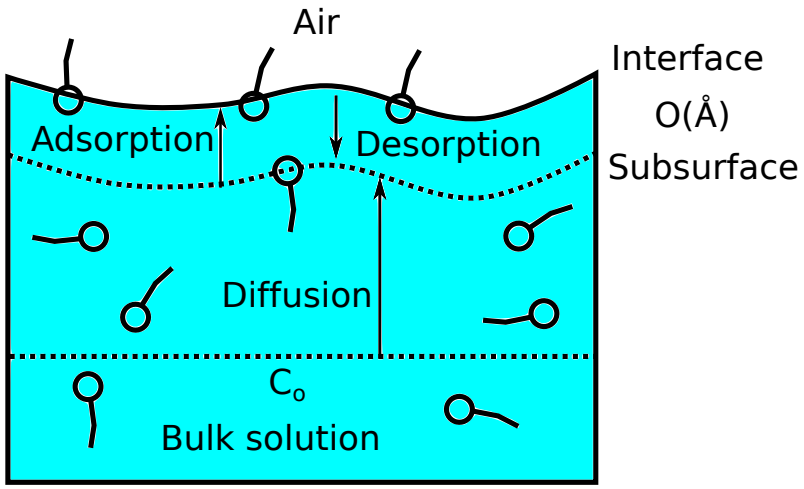

Figure 1.7: A schematic diagram of the dynamic adsorption mechanism. When a new interface is created, surfactant molecules in the bulk will first diffuse to the subsurface and adsorb onto the fluid interface. Note that the subsurface is the layer at a distance of a few molecular diameters below the surface layer.

1.2.2 Surfactant effects on air entrainment

There have been only a few studies about surfactant effects on wetting failure in the literature [75, 76, 77, 7, 8]. Deryagin and Levi [77] studied surfactant effects in slot coating flows to identify surfactants that can improve the quality of photographic film coating. They found that surfactants with certain chemical structures can delay the onset of air entrainment; the maximum coating speed increases as the concentrations of those surfactants increase. They claimed that the increment results from the interactions between the surfactants and the gelatin in the photographic emulsion.

Experimental studies from Burley et al. [7, 8] showed that surfactants can lower the maximum air entrainment speed in plunge-coating experiments. They found that systems with lower liquid surface tension have smaller U^{crit} values than those without surfactants. Marston et al. [78] studied the effect of surfactant on air entrainment hysteresis using a curtain coating method. Similar to Burley et al. [7, 8], they found that the addition of surfactants into glycerol and water mixtures reduce the maximum speed of the onset of air entrainment. The conflicting results from the prior studies point to the need for a fundamental study characterizing the influence of surfactants on

the onset of dynamic wetting failure.

1.3 Thesis Overview

The detailed studies of the influence of surfactants on the onset of wetting failure are presented in the upcoming chapters. The content and structure in each chapter are summarized here.

1.3.1 Dynamic Wetting Failure in Surfactant Solutions

In Chapter 2, the influence of insoluble surfactants on dynamic wetting failure during displacement of Newtonian fluids in a rectangular channel is studied. A hydrodynamic model for steady Stokes flows of dilute surfactant solutions is developed and evaluated using three approaches: (i) a one-dimensional (1D) lubrication-type approach, (ii) a novel hybrid of a 1D description of the receding phase and a 2D description of the advancing phase, and (iii) an asymptotic theory of Cox [J. Fluid Mech. **168**, 195-220 (1986)]. Steady-state solution families in the form of macroscopic contact angles as a function of the capillary number are determined and limit points are identified. When air is the receding fluid, Marangoni stresses are found to increase the receding-phase pressure gradients near the contact line by thinning the air film without significantly changing the capillary-pressure gradients there. As a consequence, the limit points shift to lower capillary numbers and the onset of wetting failure is promoted. The model predictions are then used to interpret decades-old experimental observations concerning the influence of surfactants on air entrainment [Chem. Eng. Sci. **31**, 901-911 (1976)].

1.3.2 Mechanisms of Dynamic Wetting Failure in The Presence of Soluble Surfactants

In Chapter 3, a hydrodynamic model and flow visualization experiments are used to understand the mechanisms through which soluble surfactants can influence the onset of dynamic wetting failure. In the model, a Newtonian liquid displaces air in a rectangular channel in the absence of inertia. A Navier-slip boundary condition and constant contact angle are used to describe the dynamic contact line (DCL), and surfactants are allowed to adsorb to the interface and moving channel wall (substrate). The Galerkin finite

element method is used to calculate steady states and identify the critical capillary number Ca^{crit} at which wetting failure occurs. It is found that surfactant solubility weakens the influence of Marangoni stresses, which tend to promote the onset of wetting failure. Adsorption of surfactants to the substrate can delay the onset of wetting failure due to the emergence of Marangoni stresses that thicken the air film near the DCL. The experiments indicate that Ca^{crit} increases with surfactant concentration. For the more viscous solutions used, this behavior can largely be explained by accounting for changes to the mean surface tension and static contact angle produced by surfactants. For the lowest viscosity solution used, comparison between the model predictions and experimental observations suggests that other surfactant-induced phenomena such as Marangoni stresses may play a more important role.

1.3.3 Dynamic Wetting Failure and Hydrodynamic Assist in Curtain Coating

In Chapter 4, dynamic wetting failure in curtain coating of Newtonian liquids is studied. A hydrodynamic model accounting for air flow near the dynamic contact line (DCL) is developed to describe two-dimensional (2D) steady wetting and to predict the onset of wetting failure. A hybrid approach is used where air is described by a one-dimensional model and liquid by a 2D model, and the resulting hybrid formulation is solved with the Galerkin finite element method. The results reveal that the delay of wetting failure in curtain coating—often termed hydrodynamic assist—mainly arises from the hydrodynamic pressure generated by the inertia of the impinging curtain. This pressure leads to a strong capillary-stress gradient that pumps air away from the DCL and thus increases the critical substrate speed for wetting failure. Although the parameter values used in the model are different from those in experiments due to computational limitations, the model is able to capture the experimentally observed non-monotonic behavior of the critical substrate speed as the feed flow rate increases [T. D. Blake et al., Phys. Fluids 11 (1999) 1995]. The influence of insoluble surfactants is also investigated, and the results show that Marangoni stresses tend to thin the air film and increase air-pressure gradients near the DCL, thereby promoting the onset of wetting failure. In addition, Marangoni stresses reduce the degree of hydrodynamic assist in curtain coating, suggesting a possible mechanism for experimental observations reported by Marston et al.

[Exp. Fluids 46 (2009) 549].

Chapter 2

Dynamic Wetting Failure in Surfactant Solutions

2.1 Introduction

Processes involving the displacement of one fluid by another in the presence of surfactant are very important in many technologies such as coating processes [79], microfluidics [80, 18], and oil recovery [81]. Many coating flows feature the steady wetting of a liquid on a substrate moving at speed U. Such a dynamic wetting process fails when incomplete displacement occurs, usually at a critical speed U^{crit}, and is accompanied by a change in flow from steady two-dimensional (2D) to unsteady three-dimensional (3D) [26]. In the case where a liquid displaces air on the substrate, wetting failure leads to air entrainment and can be detrimental for coating processes since trapped air can degrade product quality [2, 82]. Therefore, understanding the mechanisms of wetting failure and finding ways to delay the onset of wetting failure are of great industrial significance [23, 31]. [1]

Surfactants are widely used to lower surface tension and enhance wettability [79]. This is due to their amphiphilic nature (i.e., they have a hydrophilic head and a hydrophobic tail), which leads to preferential concentration at interfaces. If surfactant concentrations at fluid interfaces are not uniform, surface-tension gradients arise. The

[1] This chapter was originally published in [83].

resulting tangential stresses drive a Marangoni flow whose direction is from regions of low to high surface tension [3]. In addition, surfactants can freely transport along the interface through diffusion and convection and exchange between the interface and the bulk solution. Surfactants in the bulk can also agglomerate into micelles when the concentration is above a critical concentration and change solution rheology [84]. Due to their complex dynamics, surfactants may have a non-trivial influence on the onset of wetting failure.

In our prior wetting-failure studies in the absence of surfactants [23, 31], we studied the displacement of a receding fluid by an advancing fluid in a parallel channel, where the top boundary is stationary and the bottom substrate moves horizontally at speed U. The onset of wetting failure is characterized by a critical capillary number $Ca^{crit} = \mu U^{crit}/\sigma$, where μ is the viscosity of the more viscous phase, U^{crit} is the critical speed, and σ is the surface tension. The objective of the present chapter is to determine how Ca^{crit} changes when insoluble surfactants are present.

The addition of surfactants lowers the surface tension σ, and can also lower the equilibrium contact angle θ_{mic} according to Young's equation [65]. Our previous study [31] shows that if σ is uniformly reduced while θ_{mic} is kept constant (i.e., modeling different liquids at a fixed substrate wettability), Ca^{crit} will remain the same but U^{crit} will be lowered. In addition, if θ_{mic} is decreased while σ remains the same (i.e., increasing substrate wettability), both Ca^{crit} and the critical speed U^{crit} will be raised. However, the influence of surface tension gradients (i.e., Marangoni stresses) on Ca^{crit} (and thus U^{crit}) has not yet been characterized. Several experimental studies have reported changes in the value of U^{crit} when surfactants are present.

Deryagin and Levi [77] used slot coating to identify surfactants that can increase the critical speed U^{crit} of photographic coatings. They reported that polyglycerides of alkenylsuccinic acids, diesters, and some other surfactants can achieve this goal (increases up to $\approx 85\%$). Burley and Kennedy [7] plunged a substrate into a liquid (glycerol/water) pool and recorded the critical speed at which air entrainment commences. They found that the presence of Teepol detergent lowers the critical speed (up to $\approx$ 17.5%). Marston et al. [78] studied air-entrainment hysteresis using curtain coating with a pre-wet substrate. Similar to what Burley and Kennedy [7] observed, they found that the addition of surfactants (sodium dodecyl sulphate) into glycerol/water mixtures

reduces the critical speed (up to $\approx 66\%$).

The changes in the critical speed obtained in the studies above can also be interpreted as changes in the critical capillary number, Ca^{crit}. The values of Ca^{crit} of Deryagin and Levi [77] increase as the surfactant concentration increases. An increase in Ca^{crit} is also found in the work of Burley and Kennedy [7]. However, results from Marston et al. [78] indicate that surfactants decrease Ca^{crit}. Overall, the conflicting results from prior work point to the need for a fundamental study characterizing the influence of surfactants on wetting failure through Marangoni stresses, a reduction of surface tension and equilibrium contact angle, or a combination of these effects.

Building on our prior work [23, 31], we develop a hydrodynamic model involving creeping flows of dilute and insoluble surfactant solutions. The model is evaluated using three approaches: (i) a one-dimensional (1D) lubrication-type approach, (ii) a novel hybrid of a 1D description of the receding phase and a 2D description of the advancing phase, and (iii) an asymptotic theory of Cox [85]. Although similar 1D/2D hybrid approaches have previously been used to study single-phase [86] and two-phase [87, 88] flows, this is the first work, to the best of the authors' knowledge, that presents a hybrid model for fluid displacement with dynamic contact lines.

Section 2.2 describes the model formulation and solution methods. In section 2.3 the hybrid approach is evaluated in the absence of surfactant and compared with results from a full 2D calculation [31]. Results from approaches (i)-(iii) are compared in section 2.4. Section 2.5 discusses the influence of surfactants on wetting failure, proposes a wetting failure mechanism, and presents results from parametric studies. Section 2.6 presents a comparison between model predictions and published experimental data. Finally, section 2.7 summarizes our results.

2.2 Model formulation and solution methods

2.2.1 Governing equations and boundary conditions

A hydrodynamic model is developed for the displacement of a receding fluid by an advancing fluid within a gap H, where the top boundary is immobile and the bottom substrate moves horizontally at a speed U (Figure 2.1(a)). The viscosities of the advancing and the receding fluids are denoted by μ_{adv} and μ_{rec}, respectively. Symbols x and

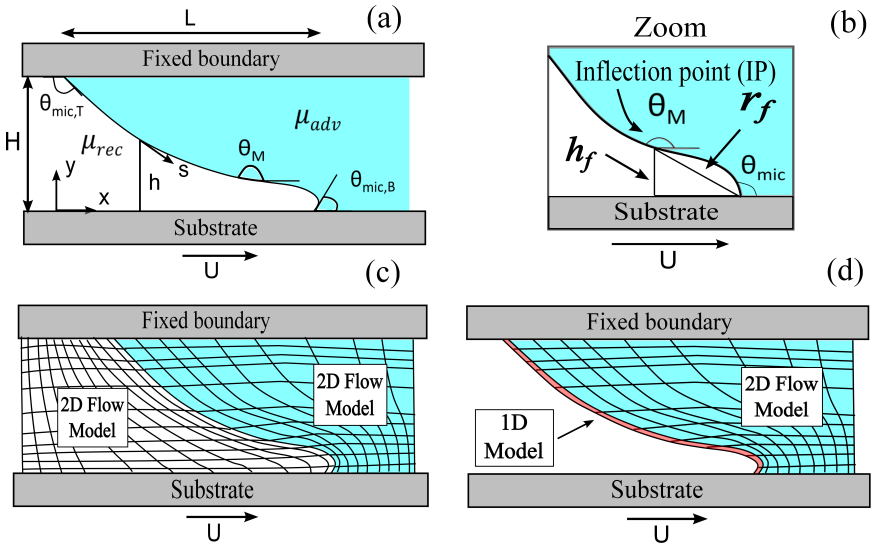

Figure 2.1: (a) Schematic of the problem geometry. (b) Enlarged view of the fluid interface and the inflection point (IP), which corresponds to the location of the maximum interface angle (θ_M). The height of the IP and the distances from the contact line to the IP are denoted by h_f and r_f, respectively. (c) Schematic of a full 2D approach. (d) Schematic of the 1D/2D hybrid approach.

y represent the Cartesian coordinates, and s is the arclength along the fluid interface (located at $y = h$) starting from the static (top) contact line. The horizontal length of the interface is denoted by L.

Figure 2.1(b) shows the difference between the microscopic contact angle θ_{mic} and the dynamic (or macroscopic or apparent) contact angle θ_M. The angle θ_{mic} is the one at which the interface contacts the substrate, whereas θ_M, arising from the viscous bending of the interface, is measured at some distance away from the dynamic contact line. In this work, the maximum angle along the fluid interface is designated as θ_M and this position corresponds to the interface inflection point (IP). The height of the IP and the distance from the dynamic contact line to the IP are denoted by h_f and r_f, respectively. Note that $\theta_{mic,T}$ and $\theta_{mic,B}$ in Figure 2.1(a) represent the microscopic contact angles at the top and the bottom substrates.

To simplify the model, we neglect the influence of inertia so that Stokes equations apply to each phase:

$$\boldsymbol{\nabla} \cdot \boldsymbol{v} = 0, \; \boldsymbol{\nabla} p = \nabla^2 \boldsymbol{v}, \tag{2.1}$$

where $\boldsymbol{v}$ and p represent fluid velocity and pressure in a given phase. Note that lengths, velocities, and stresses are non-dimensionalized with the characteristic scales H, U, and $\mu U/H$, respectively, with μ being the viscosity of a given phase.

The surfactants are assumed to be insoluble, and their transport along the fluid interface is governed by a steady-state convection-diffusion equation:

$$\boldsymbol{\nabla_s} \cdot (\boldsymbol{v_s}\Gamma) = \frac{1}{Pe}{\nabla_s}^2 \Gamma, \tag{2.2}$$

where $\boldsymbol{\nabla_s}$ is the surface-gradient operator, $\boldsymbol{v_s}$ is the interface velocity, and Γ is the dimensionless surfactant concentration scaled with the mean surfactant concentration Γ_m at the interface. The surface Peclet number $Pe = UH/D_s$ contains the surface diffusion coefficient D_s.

Following the convention of the dynamic-wetting literature, the capillary number Ca (ratio of viscous forces to surface-tension forces) and the Marangoni number M (ratio of surface-tension-gradient forces to viscous forces) are calculated based on the more viscous phase. These parameters appear in the following set of dimensionless boundary conditions along the fluid interface:

$$\boldsymbol{v} \mid_{rec} = \boldsymbol{v} \mid_{adv}, \tag{2.3}$$

$$\boldsymbol{n} \cdot \boldsymbol{v} = 0, \tag{2.4}$$

$$M/\delta(\chi)\boldsymbol{\nabla_s}\sigma \cdot \boldsymbol{t} = \boldsymbol{n} \cdot \boldsymbol{T} \cdot \boldsymbol{t} \mid_{adv} - \boldsymbol{n} \cdot \boldsymbol{T} \cdot \boldsymbol{t} \mid_{rec}, \tag{2.5}$$

$$\kappa(1/[Ca\delta(\chi)] + \sigma M/\delta(\chi)) = (\boldsymbol{n} \cdot \boldsymbol{T} \cdot \boldsymbol{n} \mid_{adv} - \boldsymbol{n} \cdot \boldsymbol{T} \cdot \boldsymbol{n} \mid_{rec}), \tag{2.6}$$

$$\left.\begin{array}{r} Ca = \mu_{adv}U/\sigma_m,\ M = (\sigma_o - \sigma_m)/\mu_{adv}U, \text{ and } \delta(\chi) = 1 \text{ for } \chi \leq 1; \\ Ca = \mu_{rec}U/\sigma_m,\ M = (\sigma_o - \sigma_m)/\mu_{rec}U, \text{ and } \delta(\chi) = 1/\chi \text{ for } \chi > 1 \end{array}\right\}. \tag{2.7}$$

Here, (2.3)-(2.4) are the no-slip and no-penetration boundary conditions, and (2.5)-(2.6) represent interfacial stress balances along the tangential and normal directions. Subscripts "*adv*" and "*rec*" indicate properties in the advancing and receding phases, respectively. At the fluid interface, unit normal vector $\boldsymbol{n}$ points toward the receding phase and unit tangent vector $\boldsymbol{t}$ is in the same direction as arclength coordinate s (Figure 2.1(a)). The term $\boldsymbol{\nabla_s}\sigma$ in (2.5) denotes the surface-tension gradient along the interface, κ in (2.6) represents the interface curvature, and $\boldsymbol{T}$ is the Newtonian stress tensor.

In these balances, $Ca\delta(\chi) = \mu_{adv}U/\sigma_m$, $M/\delta(\chi) = (\sigma_o - \sigma_m)/\mu_{adv}U$, and $\chi = \mu_{rec}/\mu_{adv}$ (see definitions for Ca, M, and $\delta(\chi)$ in (2.7); the definitions are the same as those reported by Vandre et al. [31]). In the expressions for Ca and M, σ_o is the surface tension of the surfactant-free solution and σ_m is the mean surface tension corresponding to Γ_m. In the absence of surfactant, $\sigma_m = \sigma_o$ and the Marangoni stresses vanish (i.e., $M/\delta(\chi) = 0$). This limiting case was studied in our prior work [26, 23, 31].

For simplicity, we assume that the surfactant concentration is dilute enough to apply a linear equation of state [89, 70, 90, 91]:

$$\sigma = 1 - \Gamma. \tag{2.8}$$

Here, surface tension and surfactant concentration have been non-dimensionalized using the relations $\sigma' = \sigma_m + (\sigma_o - \sigma_m)\sigma$ and $\Gamma' = \Gamma_m\Gamma$, where variables with a prime represent dimensional values [91]. We also assume that surfactants do not deposit onto the solid surface from the fluid interface, so $\boldsymbol{n} \cdot \nabla\Gamma = 0$ is applied at the two ends of the fluid interface. These boundary conditions require that a constraint of constant surfactant mass be applied:

$$\int_S \Gamma \, ds = S, \tag{2.9}$$

where S represents the total interface arclength.

A Navier-slip boundary condition is applied along the moving substrate to avoid the stress singularity caused by applying the no-slip boundary condition at the contact line [46, 92, 93, 94]:

$$\boldsymbol{t_s} \cdot (\boldsymbol{v} - \boldsymbol{U}) = \lambda \, [\boldsymbol{n_s} \cdot (\delta(\chi)\boldsymbol{T}) \cdot \boldsymbol{t_s}], \tag{2.10}$$

where $\lambda = l_{slip}/H$ is the dimensionless slip length, and l_{slip} is the dimensional slip length. The function $\delta(\chi)$ is defined in (2.7), and $\boldsymbol{n_s}$, $\boldsymbol{t_s}$, and $\boldsymbol{U}$ correspond to the substrate's normal, tangent, and velocity vectors, respectively. This slip boundary condition is applied along the entire bottom substrate and is able to recover the no-slip condition ($\boldsymbol{v} \to \boldsymbol{U}$) for distances greater than l_{slip} away from the dynamic wetting line. The no-slip boundary condition is applied to the top boundary and the no-penetration condition is applied to both the top and bottom boundaries.

In the hydrodynamic model, the microscopic contact angles θ_{mic} serve as boundary conditions at the two ends of the fluid interface [22]. Generally, θ_{mic} may depend on

the substrate speed U and material properties such as μ and σ [2]. Here, we take the simplest view and assume that θ_{mic} is constant and equal to the static contact angle θ_s [40].

In order to isolate the influence of Marangoni stresses on wetting failure, we will assume that the microscopic contact angles are neutral at both contact lines (i.e., $\theta_{mic,T} = \theta_{mic,B} = 90^o$) and remain unchanged by surfactants. In addition, the mean surface tensions σ_m are kept the same for displacements in the absence and presence of Marangoni stresses. In Sec. 2.6, these assumptions are relaxed to compare model predictions with experimental data.

The Stokes equations (2.1), surfactant-transport equation (2.2), and associated conditions [e.g., (2.3)-(2.10)] form the hydrodynamic model, which is evaluated with three approaches: (i) a 1D lubrication-type approach, (ii) a hybrid approach coupling a 1D description of the receding phase and a 2D description of the advancing phase, and (iii) an asymptotic theory of Cox [85].

2.2.2 1D model

The hydrodynamic model is simplified to a 1D equation system by using lubrication theory [95]. To properly describe the curvature κ of the interface during fluid displacement, a "quasi-parallel" (QP) approximation is made in which the curvature gradients along the x-coordinate are assumed to be equal to those along the arclength s ($d\kappa/dx \approx d\kappa/ds$) [96, 97]. Lubrication theory assumes that the flow is nearly parallel and that the interface slope is small. The QP approximation allows one to overcome the latter restriction by using the full curvature $d\theta/ds$, where θ is the local interface angle [96, 37, 31, 32]. This 1D approach is relatively simple to implement and thus it is of interest to see how its predictions compare to those from a more detailed approach such as the hybrid model (Sec. 2.2.3).

Using lubrication theory and the QP approximation, (2.1)-(2.7) can be simplified to:

$$\frac{d\kappa}{ds} = \frac{d^2\theta}{ds^2} = Ca\delta(\chi)\frac{d}{dx}\left(p_{adv} - p_{rec}\right) = F(h, Ca, \lambda, \chi, \frac{d\Gamma}{dx}, M), \tag{2.11}$$

where the curvature gradients along the arclength $d\kappa/ds$ balance the pressure gradients in the x-direction from the two phases, as described by the function $F(h, Ca, \lambda, \chi, d\Gamma/dx, M)$

(see Appendix 2.8.1). Note that p with subscripts is used to distinguish pressures in the advancing and receding phases. While the function F accounts for flows due to surface-tension gradients, it does not account for the influence of surface-tension changes on the normal stress balance. Within the approximations used to derive (2.11), the latter effect is found to be an order-of-magnitude smaller relative to that of the mean surface tension and is thus neglected.

Similarly, the surfactant-transport equation (2.2) can be expressed as follows:

$$\frac{d(u\Gamma)}{ds} = \frac{1}{Pe}\frac{d^2\Gamma}{ds^2}, \tag{2.12}$$

where u is the horizontal velocity component at the interface. This interfacial velocity depends on the same variables as the function F (see Appendix 2.8.1). Note that the surfactant-transport equation (2.12) is coupled with (2.11) through the surface equation of state (2.8).

The following geometric relationships are used to obtain the interface height h and x-coordinate:

$$\frac{dh}{ds} = -\sin\theta;\ \frac{dx}{ds} = -\cos\theta. \tag{2.13}$$

To obtain the profiles of interface angle $\theta(s)$, surfactant concentration $\Gamma(s)$, and interface height $h(s)$, the governing equations (2.11)-(2.13) along with conditions (2.8) and (2.9) are solved with a second-order finite-difference method [23].

2.2.3 Hybrid model

One way to evaluate the hydrodynamic model of Sec. 2.2.1 is to use a full 2D description of both the advancing and receding phases. In our prior work (in which surfactants were absent), this was accomplished by discretizing both phases into finite elements (Figure 2.1(c)) [26, 23, 31]. Here, we use a less computationally intense approach that combines a 1D description of the receding phase while retaining a 2D description of the advancing phase (Figure 2.1(d)). This novel hybrid approach is motivated by the observations that (i) the receding fluid becomes long and slender as the interface deforms near the onset of wetting failure, and (ii) a 2D description of the advancing phase is needed to capture the correct streamline pattern in that phase [23, 31]. Such interface deformation is especially evident in air entrainment where $\chi \ll 1$, which is the case of most interest

in this chapter. Note that the hybrid approach is distinct from the 1D approach of Sec. 2.2.2, where 1D descriptions are used for both phases. In addition, the influence of surface-tension changes in both the normal and tangential stress balances is accounted for in the hybrid approach.

Lubrication theory and the QP approximation (Sec. 2.2.2) are applied to the receding phase to obtain equations involving the pressure and velocity in that phase:

$$Ah + \frac{1}{2}Bh^2 + \frac{1}{6}\frac{dp}{ds}h^3 = 0, \tag{2.14}$$

$$\frac{\partial u}{\partial y}|_s = B + \frac{dp}{ds}h \quad \text{where} \quad A = \frac{\chi h + \chi\lambda u_{\rm s} - \frac{1}{2}\frac{dp}{ds}h^2}{\lambda + h}\ ,\ B = \frac{-\chi + A}{\lambda}, \tag{2.15}$$

where $u_{\rm s}$ represents the horizontal interface velocity, h is the interface height, and $\lambda = l_{slip}/H$ is the dimensionless slip length. The velocity gradient in (2.15) is evaluated at the interface.

In the advancing phase, a full 2D description ((2.1) and associated boundary conditions) is applied. In addition, the full convection-diffusion equation for surfactant transport ((2.2) and associated conditions) is used.

The 1D and 2D descriptions are coupled through the interfacial boundary conditions (2.3)-(2.6). Lubrication theory provides expressions for the normal and tangential stresses in the receding phase:

$$\boldsymbol{n}\cdot\boldsymbol{T}\cdot\boldsymbol{t}|_{rec} \approx \chi\frac{\partial u}{\partial y}\ ; \quad \boldsymbol{n}\cdot\boldsymbol{T}\cdot\boldsymbol{n}|_{rec} \approx p. \tag{2.16}$$

.

The equations governing the 1D and 2D descriptions are solved using the Galerkin finite-element method (FEM) with elliptic mesh generation (see Appendix 2.8.2). Mesh independence is determined by varying the number of elements until there is less than a 2% variation in the values of Ca^{crit} predicted from steady-state solution families. Since the interface tends to bend sharply near the contact line, elements are refined locally to resolve large gradients in the interface curvature. We found that to obtain mesh-independent solutions, element sizes near the contact line need to be less than $10^{-3}\lambda$, where λ is the dimensionless slip length in (2.10).

Advantages of the hybrid approach arise from its computational efficiency. Since the receding phase is described with a 1D model, the hybrid model reduces the number

of variables by nearly 50% in comparison to a full 2D flow model [23, 31] (Figures 2.1(c)-2.1(d)). In addition, mesh quality for the advancing phase is improved because mesh lines do not need to be reconciled with those in the receding phase. These factors make the hybrid model a potentially powerful tool for studying fluid displacement in realistic coating systems that commonly include complicated geometries, complex liquid rheology, and transport of surface-active agents.

2.2.4 Asymptotic theory

Cox developed an asymptotic theory relating the apparent contact angle θ_{ap} to the microscopic contact angle θ_{mic} and the capillary number Ca during fluid displacement [35]. Later, Cox extended the theory to account for insoluble surfactants and found the following relation [85]:

$$\left.\begin{aligned}
&\frac{\sigma_{cox}}{q(\theta_{ap};\chi)}\,[\,g(\theta_{ap};\chi)-g(\theta_{mic};\chi)\,]=Ca\ln(\lambda_{cox}^{-1}),\\
&g(\theta;\chi)=\int_0^{\theta}\frac{q(\phi;\chi)}{f(\phi;\chi)}\,\mathrm{d}\phi,\\
&q(\theta;\chi)=exp\,[\int_0^{\theta}\frac{h(\phi;\chi)}{f(\phi;\chi)}\,\mathrm{d}\phi\,],\\
&h(\phi;\chi)=-2\,\{\frac{\chi[(\pi-\phi)\cos\phi+\sin\phi]}{(\pi-\phi)^2-\sin^2\phi}+\frac{\phi\cos\phi-\sin\phi}{\phi^2-\sin^2\phi}\},\\
&f(\phi;\chi)=2\,\sin\phi\,\{\frac{\chi(\pi-\phi)}{(\pi-\phi)^2-\sin^2\phi}+\frac{\phi}{\phi^2-\sin^2\phi}\},
\end{aligned}\right\}\qquad(2.17)$$

where σ_{cox} represents the dimensionless interfacial tension (scaled by a characteristic interfacial tension) far away from the contact line, $\chi=\mu_{rec}/\mu_{adv}$ is the viscosity ratio, and ϕ is a dummy variable. The theory assumes that inertia and surfactant diffusion are negligible, and is limited to low-speed steady wetting with slowly varying interface angles ($Ca \ll 1$ and $Ca|\partial\theta/\partial x| \ll 1$, respectively). In contrast to the 1D and hybrid approaches, the asymptotic theory does not use a 1D description of either phase.

There are several important differences between the parameters in the asymptotic theory and parameters introduced in Sec. 2.1. The parameter $\lambda_{cox}=l_{mic}/l_M$ (assumed small) is the ratio between an arbitrary macroscopic length scale l_M (10 μm - 1 mm) and a microscopic length scale l_{mic} ($\sim$ 1 nm) [22, 52, 98]. Although λ_{cox} has a similar meaning to the dimensionless slip length λ in the Navier-slip boundary condition (2.10), the values for these two parameters may not be the same in general [2, 99]. In addition,

θ_{ap} need not equal θ_M. Because of the different non-dimensionalization of surface tension in the asymptotic theory, σ_{cox} does not necessarily equal the mean surface tension σ_m defined in (2.7). In spite of these differences, the asymptotic theory can be compared to the 1D and hybrid models by treating λ_{cox} and σ_{cox} as fitting parameters, and by assuming that $\theta_{ap} = \theta_M$.

The relation between θ_{ap} and Ca is obtained numerically because the integral functions $g(\theta;\chi)$ and $q(\theta;\chi)$ in (2.17) lack analytical solutions. Values of θ in an array starting from θ_{mic} to 180^o are substituted for θ_{ap} in the first equation of (2.17), and the corresponding Ca values are then calculated. This method stops when $\theta \approx 180^o$ and the calculated capillary number is assumed to correspond to the critical capillary number Ca^{crit}. We note that this is an assumption since the asymptotic theory is expected to break down as $\theta \to 180^o$ [35]. Nevertheless, this assumption describes well the behavior of Ca^{crit} in the absence of surfactants [31], so we are motivated to examine it here. The values of Ca^{crit} obtained from the asymptotic theory can be compared to those obtained from the 1D model of Sec. 2.2.2 and the hybrid model of Sec. 2.2.3.

Before proceeding, we note a connection between the asymptotic theory and the 1D model of Sec. 2.2. In the absence of surfactants, the 1D model has a form very similar to equations obtained from a long-wavelength theory valid for large slopes [37, 32]. The long-wavelength theory, which expands around Stokes flow in a wedge, is able to recover Cox's asymptotic solution [37, 35]. In the presence of surfactants, we expect that the 1D model behaves similarly. A detailed analysis of this behavior, an analysis for small Marangoni numbers, and extension of the asymptotic theory to better predict the wetting transition [40, 42] are all beyond the scope of the present chapter but would be interesting topics for future work.

2.3 Evaluation of hybrid model in absence of surfactants

In this section, we compare solutions from the hybrid model with those from a full 2D FEM calculation when surfactants are absent [23, 31]. These Ca^{crit} values correspond to limit points in families of steady-state solutions, where a solution family takes the form of macroscopic contact angles θ_M as a function of the capillary number Ca.

In Figure 2.2(a), Ca^{crit} values are plotted for various viscosity ratios χ. The hybrid

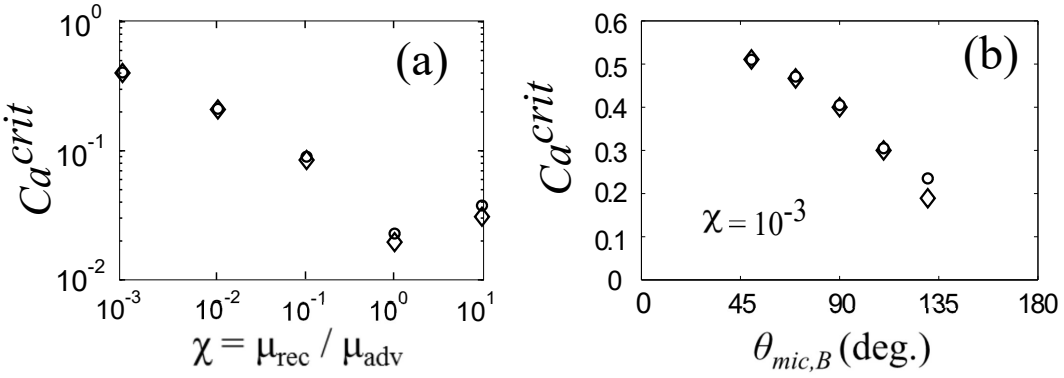

Figure 2.2: Comparison of critical capillary numbers in the absence of surfactant obtained from the full 2D flow model (circles) and the hybrid model (diamonds) while varying (a) fluid viscosity ratio and (b) substrate wettability. The relevant system parameters are (a) $\lambda = 10^{-4}$ and $\theta_{mic,T} = \theta_{mic,B} = 90^o$, (b) $\chi = 10^{-3}$, $\lambda = 10^{-4}$, and $\theta_{mic,T} = 90^o$.

model compares well with the full 2D flow model, especially when $\chi < 1$. Note that $\chi \ll 1$ corresponds to air/liquid displacement where the advancing phase is more viscous than the receding phase. Figure 2.2(b) shows that the agreement extends to various substrate wettabilities. The data remain restricted to partially wetting substrates where $50^o \leq \theta_{mic,B} \leq 130^o$ to avoid extensive distortion of the quadrilateral finite elements near the contact line. Note that $\theta_{mic,T}$ is fixed to 90^o to isolate the influence of wettability of the bottom substrate.

The excellent agreement between the results from the hybrid and full 2D calculations in the case of air/liquid displacement ($\chi \ll 1$) arises because viscous effects from the air are only important near the dynamic contact line, where the air flow is restricted to a slender wedge. Consequently, pressures in the air (receding phase) are well-described by lubrication theory and the QP approximation used in the hybrid model. Given the computational efficiency of the hybrid model and our interest in air entrainment ($\chi \ll 1$), we use it rather than a full 2D FEM calculation to study the influence of insoluble surfactants.

2.4 Comparison between models

In this section, solutions from each approach described in Sec. 2.2 are compared in the presence of surfactants. We make these comparisons for two reasons. First, we wish to test how well the predictions of Ca^{crit} from the asymptotic theory of Cox [85] compare to predictions from the other two approaches. In the absence of surfactants, similar comparisons were made in our prior work [23, 31], but it has not yet been established how well the theory accounting for surfactants works. Second, we wish to test the limits of validity of the 1D approach. In the absence of surfactants, our prior work [23, 31] shows that the 1D approach overpredicts Ca^{crit} when the receding phase is much less viscous than the advancing phase ($\chi \ll 1$) because it does not predict the correct streamline pattern in the advancing phase. However, when $\chi \geq 1$, the 1D and 2D approaches give similar quantitative predictions. When Marangoni stresses due to surfactants are present, it is not yet clear how well the different predictions compare.

Unless stated otherwise, representative parameter values here and in Sec. 2.5 are $10^{-3} \leq \chi \leq 10$, $\theta_{mic,T} = \theta_{mic,B} = 90^o$, and $\lambda = 10^{-4}$ and 10^{-2}. An increase in λ only increases the Ca^{crit} values without changing the qualitative nature of the solutions presented in the remainder of the chapter (results not shown). Note that the microscopic contact angle at the top substrate $\theta_{mic,T}$ is fixed to 90^o in all cases, so we only present values of $\theta_{mic,B}$ in the remainder of the chapter. The Marangoni number M is taken as 0 or 1 to illustrate the cases where Marangoni stresses are absent and present, respectively. The Peclet number Pe is taken as 10^3 to represent the case of convection-dominated surfactant transport.

The macroscopic contact angles θ_M (maximum interface angle; Sec. 2.1) are determined as a function of the capillary number Ca for various viscosity ratios and thus form steady-state solution families (Figure 2.3). The solution families exhibit a limit point corresponding to the largest Ca, which is denoted as the critical capillary number Ca^{crit}. Beyond this Ca^{crit} value ($Ca > Ca^{crit}$), we are unable to find 2D steady-state solutions, suggesting that the system may develop transient or 3D flows leading to wetting failure [31, 100]. For the 1D and hybrid models, Ca^{crit} corresponds to a turning point in the solution paths that connects the stable (lower) and unstable (upper) branches of steady-state solutions.

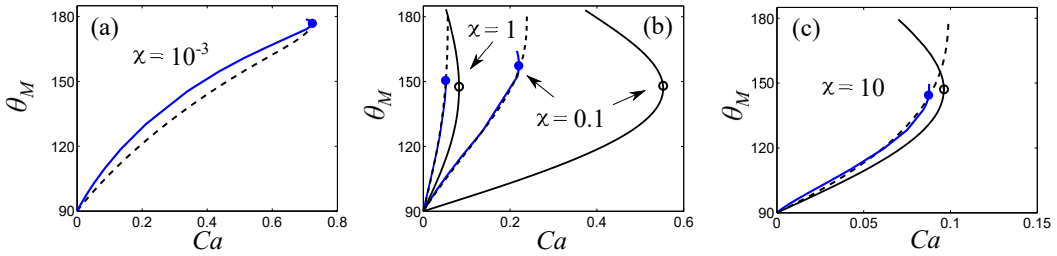

Figure 2.3: Comparison of solution families in the presence of surfactant obtained from the asymptotic theory (dashed lines), 1D model (curves with open symbols), and hybrid model (curves with solid symbols) for various χ values: (a) $\chi = 10^{-3}$; (b) $\chi = 1,\ 0.1$; (c) $\chi = 10$. Dashed lines denote the theoretical result in (2.17) with $\lambda_{cox} = 0.07,\ \theta_M = \theta_{ap}$, and various σ_{cox} values: (a) $\sigma_{cox} = 1.70$; (b) $\sigma_{cox} = 0.78, 1.15$; (c) $\sigma_{cox} = 0.92$. Other parameter values are $M = 1$, $Pe = 10^3$, $\lambda = 10^{-2}$, and $\theta_{mic,B} = 90^o$.

For the asymptotic theory, Ca^{crit} is assumed to coincide with the Ca value where the apparent angle θ_{ap} is 180^o. Note that θ_{ap} in the asymptotic theory (2.17) is approximated as θ_M in Figure 2.3. As discussed in Sec. 2.2.4, the length scale ratio λ_{cox} and the surface tension σ_{cox} in (2.17) are treated as fitting parameters in order to compare solution families. Prior studies in the absence of surfactants suggest that the asymptotic theory has the best agreement with FEM calculations when $\lambda_{cox} \sim 10\lambda$ [31]. Therefore, λ_{cox} is fixed to $\sim 10\lambda$ and σ_{cox} is tuned to match solution families from the asymptotic theory with those from the hybrid model.

Overall, Figure 2.3 demonstrates that the asymptotic theory matches the lower (stable) branch of solution families predicted from the hybrid model over the entire χ range. In contrast, the 1D model only approximates well the hybrid model when $\chi \geq 1$. For this reason, solution families from the 1D model are neglected in Figure 2.3(a) where $\chi = 10^{-3}$. Similar behavior is observed in the absence of surfactants [23, 31].

Figure 2.4 shows the surfactant concentration profiles obtained with the 1D model and the hybrid model for various viscosity ratios. (Because profiles from the asymptotic theory [85] cannot readily be extracted, they are not included in Figure 2.4.) In the case where Marangoni stresses are absent (i.e., $M = 0$), the surfactants are passive and the fluid motion at the interface can be inferred from the concentration profiles. Note that the mean surface tensions σ_m defined in the capillary and Marangoni numbers (2.7) are kept the same in both cases so that the only factor influencing concentration

distributions is the surface-tension gradients.

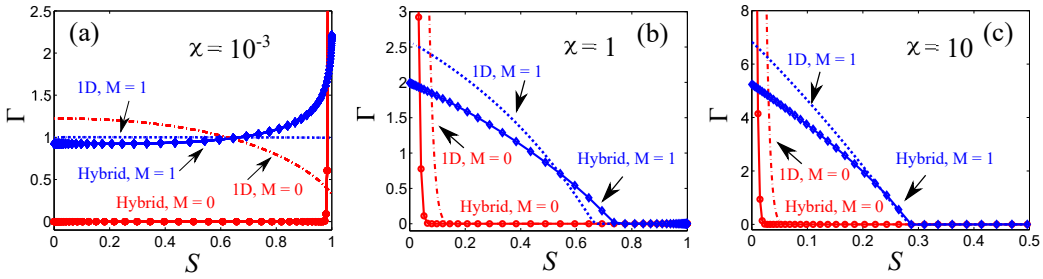

Figure 2.4: Surfactant concentration profiles obtained with the 1D model and the hybrid model at (a) $\chi = 10^{-3}$; (b) $\chi = 1$; (c) $\chi = 10$. The concentration is plotted as a function of arclength coordinate s for $M = 1$ (blue dotted line), $M = 0$ (red dash-dotted line) for the 1D model, and $M = 1$ (blue diamonds), $M = 0$ (red circles) for the hybrid model. In each plot $Ca = Ca^{crit}$: (a) $Ca = 0.72$ (hybrid) and $Ca = 40.4$ (1D); (b) $Ca = 0.05$ (hybrid) and $Ca = 0.08$ (1D); (c) $Ca = 0.088$ (hybrid) and $Ca = 0.096$ (1D). Note that (a)-(c) only show part of the complete concentration profiles. The maximum concentrations in the case of $M = 0$ are around (a) 300 (hybrid); (b) 35 (hybrid) and 25 (1D); (c) 75 (hybrid) and 70 (1D). Other parameter values are $Pe = 10^3$, $\lambda = 10^{-2}$, and $\theta_{mic,B} = 90^o$.

When $M = 0$ and $\chi = 10^{-3}$ (Figure 2.4(a)), the hybrid model predicts that surfactants are carried toward the dynamic contact line ($s = 1$), whereas the 1D model predicts that surfactants are carried toward the static contact line ($s = 0$). (Even in the absence of surfactants, the the 1D model predicts the incorrect streamline pattern for $\chi = 10^{-3}$ [23, 31].) As a consequence, when $M = 1$ the Marangoni stresses predicted from the hybrid model are directed toward the static contact line and those from the 1D model toward the dynamic contact line. In contrast, in the cases where $\chi \geq 1$ (Figures 2.4(b)-2.4(c)), surfactant concentration profiles from the 1D model compare well to those from the hybrid model, indicating that the same direction (toward the dynamic contact line) of Marangoni stresses is predicted from both approaches.

Figure 2.5 shows streamlines and pressure contours obtained from the 1D model and hybrid model when $M = 1$. For each viscosity ratio χ, streamlines from the hybrid model display a rolling-flow pattern in the advancing phase, which results from the viscous drag by the moving substrate. In the case of a low-viscosity receding phase ($\chi = 10^{-3}$), the rolling flow dominates the advancing phase and sets the direction of flow along the fluid interface (Figure 2.5(a)). A recirculation region is found near

the top contact line, and this primarily results from the Marangoni stresses (see Sec. 2.5.1 for an explanation). In contrast, in the cases where $\chi \geq 1$, the receding phase dominates the fluid displacement and the interfacial flow. Therefore, the streamlines in the advancing phase split into two parts with one following the rolling-flow pattern and the other forming a recirculation region near the interface (Figures 2.5(b)-2.5(c)).

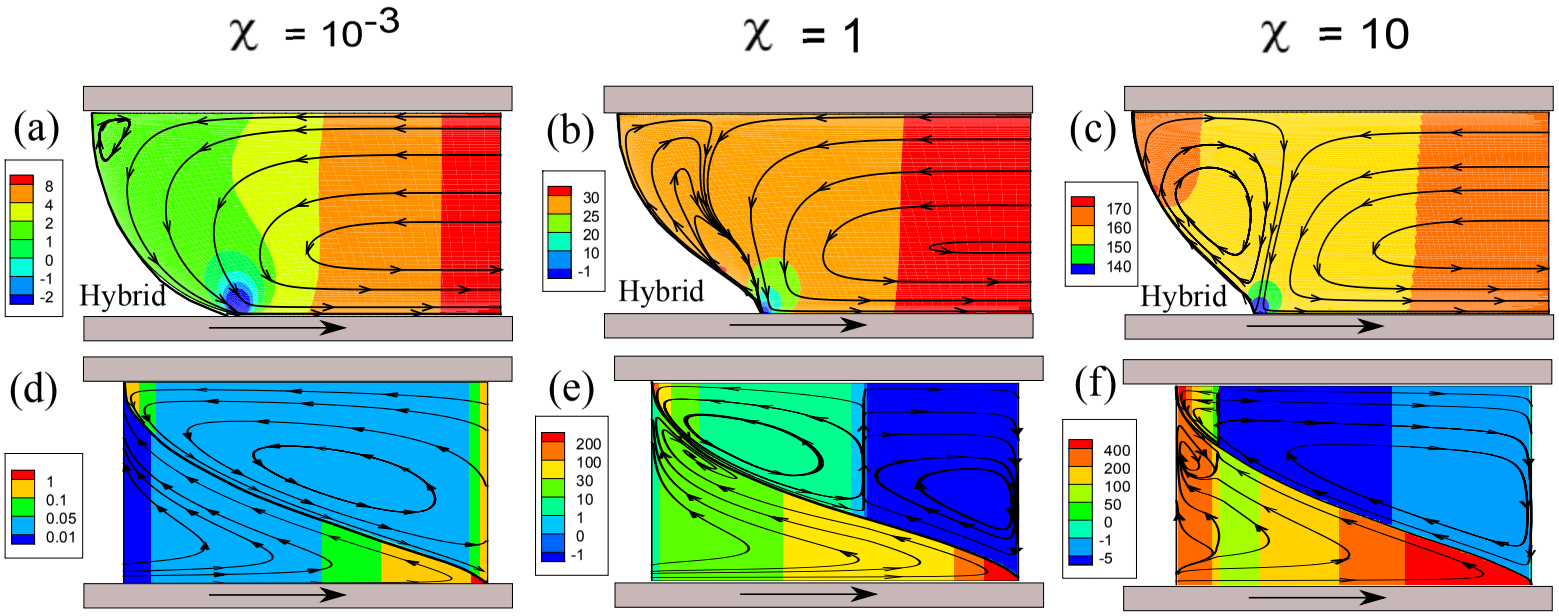

Figure 2.5: Streamlines and pressure contours obtained with the hybrid model (a)-(c) and the 1D model (d)-(f) in the presence of Marangoni stresses ($M = 1$): (a),(d) $\chi = 10^{-3}$; (b),(e) $\chi = 1$; (c),(f) $\chi = 10$. Other parameter values are the same as those listed in Figure 2.4.

Similar to what is found in the absence of Marangoni stresses [23, 31], the 1D model does not consider the flow created when the moving substrate drags the advancing phase. Therefore, streamlines from the 1D model are primarily determined by the receding phase and the Marangoni flow. When the receding-phase stresses are small ($\chi = 10^{-3}$), Marangoni stresses dominate and cause a recirculation zone in the advancing phase (Figure 2.5(d)). The receding-phase stresses cause another recirculation zone as the viscosity of that phase increases (Figures 2.5(e)-2.5(f)).

Although the 1D model does not predict the streamline pattern well, the pressure contours still provide valuable insight into the fluid motion in the receding phase because the 1D description is also applied to the receding flow in the hybrid model. For each χ, adverse pressure gradients are developed in the receding phase to pump the receding fluid away from the contact line.

The influence of the viscosity ratio χ on the onset of wetting failure when $M = 1$ is illustrated in Figure 2.6(a), where Ca^{crit} values obtained from the three approaches of Sec. 2.2 are plotted. Similar to Figure 2.3, the 1D model overestimates Ca^{crit} when $\chi < 1$, whereas the asymptotic theory of Cox matches the hybrid model well. Figure 2.6(b) shows the effect of substrate wettability when $\chi = 10^{-3}$. Here the quantitative agreement between the asymptotic theory and hybrid model is not as good, although the trend predicted is similar. The resemblance between Figure 2.2 and Figure 2.6 suggests that wetting failure with (Figure 2.6) and without (Figure 2.2) Marangoni stresses is governed by similar physical mechanisms. In addition, comparison of Ca^{crit} values from Figure 2.2(b) and Figure 2.6(b) indicate that Marangoni stresses decrease Ca^{crit} over a broad range of microscopic contact angles. The physical mechanism responsible for this will be discussed in Sec. 2.5.2.

Even though the 1D and hybrid models predict very different streamline patterns in the advancing phase, both models yield similar predictions for Ca^{crit} when $\chi \geq 1$. Since the receding phase becomes more dominant as χ increases, and both models use the same description of that phase, the prediction of Ca^{crit} becomes less sensitive to the flow structure in the advancing phase as χ increases.

The results of this section demonstrate that the asymptotic theory [85] accounting for insoluble surfactants describes well the qualitative behavior of Ca^{crit} over a wide range of viscosity ratios. The results also show that the 1D model yields qualitatively

incorrect predictions (i.e., opposite direction of Marangoni stresses) when the viscosity ratio is small ($\chi \ll 1$). However, the 1D model may still be useful for studying liquid withdrawal or liquid-liquid displacement since its predictions are more accurate for $\chi \geq 1$. Since we are primarily interested in the case of air entrainment ($\chi \ll 1$), only the hybrid model is used for the results presented in Sec. 2.5.

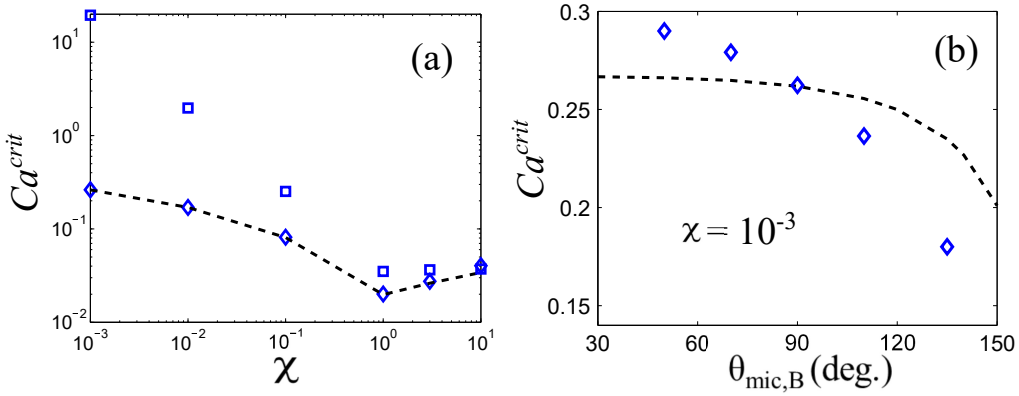

Figure 2.6: (a) Comparison of critical capillary number as a function of viscosity ratio obtained from the 1D model (squares), hybrid model (diamonds), and asymptotic theory (dashed line). (b) Critical capillary number as a function of substrate wettability when $\chi = 10^{-3}$. Other parameter values are $Pe = 10^3$, $\lambda = 10^{-4}$, $\lambda_{cox} = 10\lambda = 10^{-3}$, $M = 1$, and $\theta_{mic,B} = 90^o$ with $\sigma_{cox} = 1.6, 1.3, 1, 0.72, 0.75, 0.9$ for the asymptotic theory (from left to right) in (a), and $\sigma_{cox} = 1.6$ in (b).

2.5 Influence of surfactants on wetting failure

In this section, the influence of Marangoni stresses on wetting failure during air/liquid displacement ($\chi = 10^{-3}$) is studied using the hybrid model. A physical explanation of the influence of Marangoni stresses on Ca^{crit} is then proposed. At the end of this section, parametric studies with respect to the Marangoni number M and Peclet number Pe are presented.

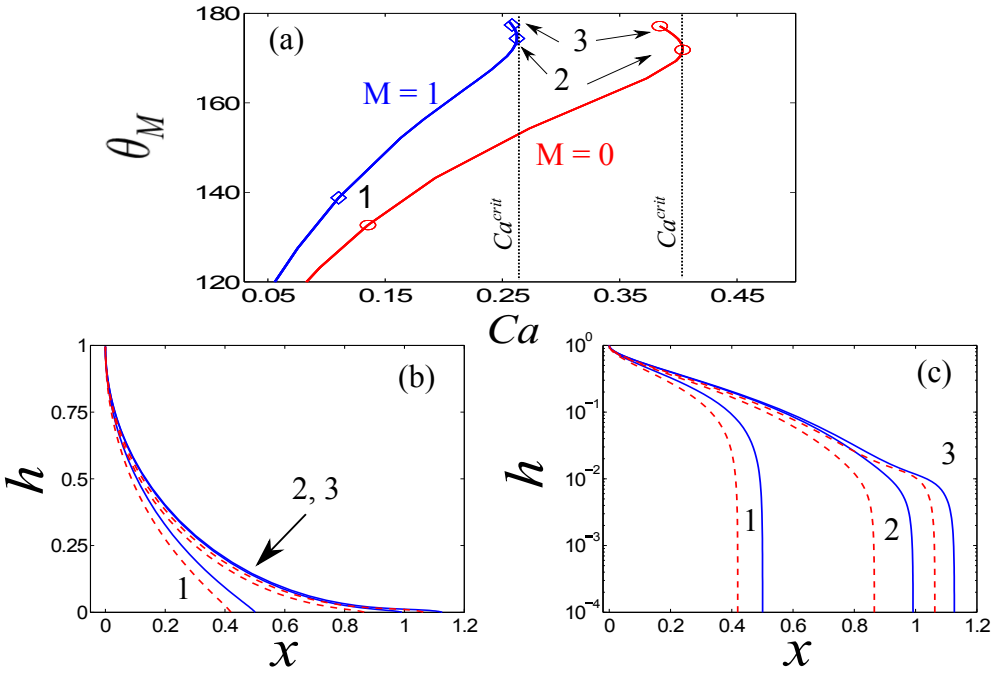

Figure 2.7: (a) Solution families obtained with the hybrid model near Ca^{crit} for $M = 1$ (blue curve with diamonds) and $M = 0$ (red curve with circles). (b) and (c) Interface profiles corresponding to three different points along each solution family shown in (a). Blue solid and red dashed lines denote interfaces for $M = 1$ and $M = 0$, respectively. Note that (c) is a semi-logarithmic plot. Other parameter values are $\chi = 10^{-3}$, $Pe = 10^3$, $\lambda = 10^{-4}$, and $\theta_{mic,B} = 90^o$.

2.5.1 Limit points

Figure 2.7 shows interface profiles for three wetting states along the steady-state solution paths when $\chi = 10^{-3}$. Figure 2.7(a) illustrates that the presence of Marangoni stresses ($M = 1$) decreases Ca^{crit}, meaning that the Marangoni stresses promote the onset of wetting failure. Notably, Marangoni stresses also appear to increase the rate at which θ_M increases with Ca. This is consistent with experimental observations of receding contact angles that decrease more quickly with contact-line speed when surfactant is present [101, 102, 103]. Figures 2.7(b)-(c) show that interface deformation primarily occurs near the dynamic contact line as the interface elongates, which confirms the formation of a thin-film wedge in the receding phase [2, 104]. Figures 2.7(b)-(c) also reveal that Marangoni stresses ($M = 1$) cause greater interface elongation, which implies that Marangoni stresses help the penetration of the receding air into the advancing liquid, thereby promoting wetting failure.

Figure 2.8 compares pressure contours, streamlines, and velocity magnitudes for $M = 0$ and $M = 1$ near Ca^{crit}. In both systems, the advancing phase is dragged by the moving substrate, which results in a rolling-flow pattern in that phase. However, the flow field for $M = 1$ exhibits a recirculation region near the top contact line (Figure 2.8(a)). This is caused by Marangoni stresses, which act against the direction of the rolling flow and in turn drag the advancing fluid. The drag created by the Marangoni stresses can have a significant influence on the flow field near the top contact line because the fluid motion there is relatively slow (Figure 2.8(c)-(d)). In addition, the velocity magnitudes are also decreased by the Marangoni stresses in regions near the interface (Figure 2.8(c)); these stresses point toward the static contact line (Figure 2.4(a)). Overall, the plots in Figure 2.8 demonstrate that Marangoni stresses have a significant influence on the flow field near the fluid interface.

2.5.2 Physical mechanisms

As suggested in Sec. 2.4, the mechanism of wetting failure in the presence and absence of Marangoni stresses may be similar. In the absence of Marangoni stresses, wetting failure occurs when the capillary-stress gradients can no longer provide the pressure gradients required to pump the receding fluid away from the contact line [31]. In this

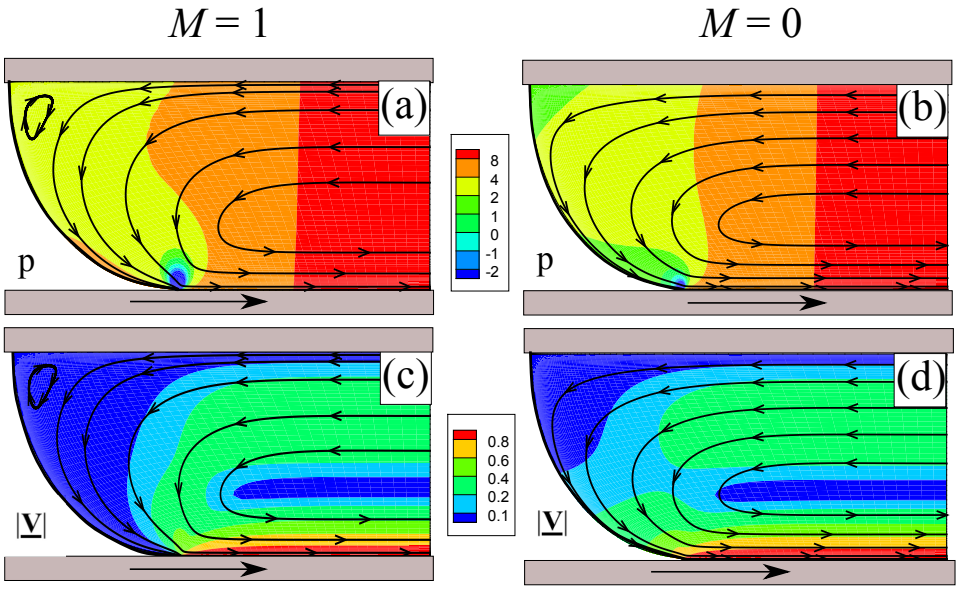

Figure 2.8: (a),(b) Pressure contours and (c),(d) velocity-magnitude contours obtained for $M = 1$ ((a),(c)) and $M = 0$ ((b),(d)). Other parameter values are $Ca = 0.262$ for $M = 1$, $Ca = 0.436$ for $M = 0$, $\chi = 10^{-3}$, $Pe = 10^3$, $\lambda = 10^{-4}$, and $\theta_{mic,B} = 90^o$.

section, we study how this mechanism is modified when Marangoni stresses are present. As we will show, Marangoni stresses increase the receding-phase pressure gradients near the contact line by thinning the air film without significantly changing the capillary-pressure gradients there. As a result, wetting failure occurs at lower substrate speeds (capillary numbers).

According to lubrication theory, which is applied to the receding phase in the hybrid model, the receding-phase pressure gradients at the inflection point (IP) scale as:

$$\left|\frac{dp}{dx}\right| \sim \frac{\chi}{{h_f}^2}, \tag{2.18}$$

where χ is the viscosity ratio and h_f represents the height of the IP (see Figure 2.1(b)). Because of the Navier-slip boundary condition (2.10) applied in the hybrid model, the interface curvature κ near the dynamic contact line diverges as a function of r ($\kappa \sim \ln(r)$) [31, 39]. Therefore, the capillary-stress gradients at the IP scale as

$$\frac{1}{Ca}\left|\frac{d\kappa}{dx}\right| \sim \frac{1}{Ca}\left(\frac{1}{r_f}\right), \tag{2.19}$$

where r is the radial distance of the interfacial position from the contact line and r_f represents the radial distance of the IP (see Figure 2.1(b)). Note that (2.19) is simplified from a more complicated expression for systems where $1/h_f \gg \lambda$ [31].

Figure 2.9(a) shows the capillary-stress gradient and receding-phase pressure gradient as a function of Ca. These gradients are equal at $Ca = Ca^{crit}$ for both $M = 0$ and $M = 1$, confirming that the wetting-failure mechanism is similar in both cases. In addition, the scaling relationships (2.18) and (2.19) match the numerical results well. Notably, the pressure gradients when $M = 1$ grow at a quicker rate than those when $M = 0$, and so match the capillary-stress gradients at a smaller Ca^{crit} value. Interestingly, the values of the capillary-stress gradient do not change significantly. The presence of Marangoni stresses thus accelerates the onset of wetting failure by increasing the pressure gradients in the receding phase.

To investigate why Marangoni stresses increase the receding-phase pressure gradients, the receding-phase shear stresses at the IP are compared. As shown in Figure 2.9(b), the receding-phase shear stresses when $M = 1$ are stronger than those when $M = 0$; this is a consequence of the tangential stress balance (2.5). These stronger shear stresses mean that higher velocity gradients (du/dy) are needed near the interface. This is achieved by a thinning of the air film (air velocity changes over a smaller distance); the lower interfacial velocity (Figure 2.8(c)) also means that thinning is needed to increase the velocity gradient. Since the air film is thinned (h_f decreases) in the presence of Marangoni stresses, the receding-phase pressure gradients are increased according to the scaling (2.18). Direct evidence of the air-film thinning will be presented below (Figure 2.10(a)).

In Figure 2.9(b), scaling relationships for the receding-phase shear stresses are also included. According to lubrication theory, the shear stresses can be approximated as

$$\mu_{rec} \left| \frac{du}{dy} \right| \sim \mu_{rec} \, \frac{U}{h_f}, \tag{2.20}$$

where μ_{rec} is the receding-phase viscosity and U is the substrate speed. As shown in Figure 2.9(b), the above scaling matches the shear stresses in the case where $M = 0$ (red dashed line) but a better scaling is needed for the case where $M = 1$,

$$\mu_{rec} \left| \frac{du}{dy} \right| \sim \frac{\sigma_m}{L}, \tag{2.21}$$

where σ_m is the mean surface tension and L represents the horizontal interface length (see Figure 2.1). This expression reflects the fact that the surface tension determines the magnitude of the shear stresses which balance Marangoni stresses. As can be seen in Figure 2.9(b), the scaling (2.21) agrees better with the numerical results (blue solid line).

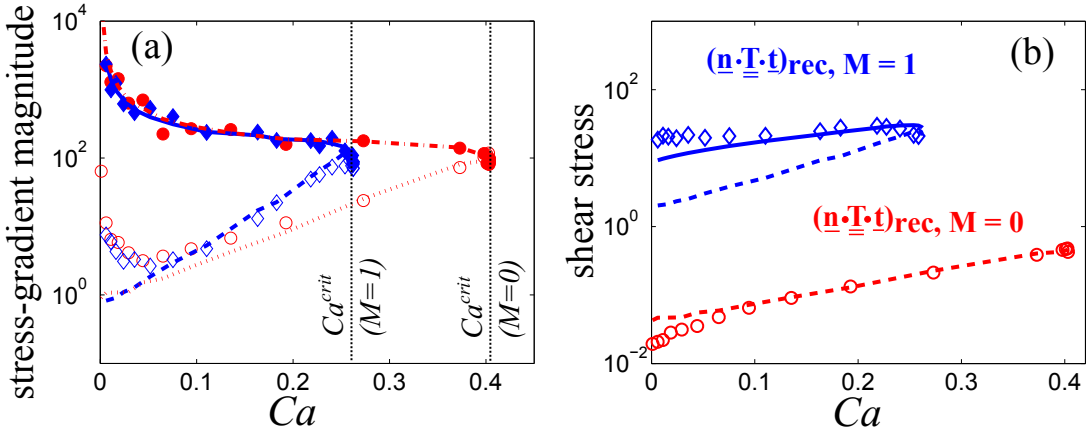

Figure 2.9: (a) Magnitude of stress gradients at the IP for $M = 1$ (blue diamonds) and $M = 0$ (red circles). The capillary-stress gradients (filled symbols) match the receding-phase pressure gradients (open symbols) at Ca^{crit} values denoted by black dotted lines. Blue solid ($M = 1$) and red dash-dotted lines ($M = 0$) are from (2.19). Blue dashed ($M = 1$) and red dotted lines ($M = 0$) are from (2.18). (b) The magnitude of receding-phase shear stresses at the IP for $M = 1$ (blue diamonds) and $M = 0$ (red circles). Blue and red dashed lines are from (2.20) for $M = 1$ and $M = 0$, respectively. Blue solid line is from (2.21) for $M = 1$. Other parameter values are $\chi = 10^{-3}$, $Pe = 10^3$, $\lambda = 10^{-4}$, and $\theta_{mic,B} = 90^o$.

Figure 2.10(a) shows the change of the characteristic lengths (Figure 2.1(b)) at the IP with Ca. For both $M = 0$ and $M = 1$, r_f and h_f decrease with Ca, which means that the IP approaches the dynamic contact line as Ca increases and the air film is thinned and stretched. Both r_f and h_f when $M = 1$ are smaller compared to the case when $M = 0$. This confirms that Marangoni stresses further thin the air film and explains the larger receding-phase pressure gradients when $M = 1$ (Figure 2.9(a)).

Figure 2.10(b) demonstrates that the interfacial length L when $M = 1$ has a larger value compared to the case when $M = 0$, indicating that Marangoni stresses cause greater interface elongation and help the penetration of the receding phase (Figures

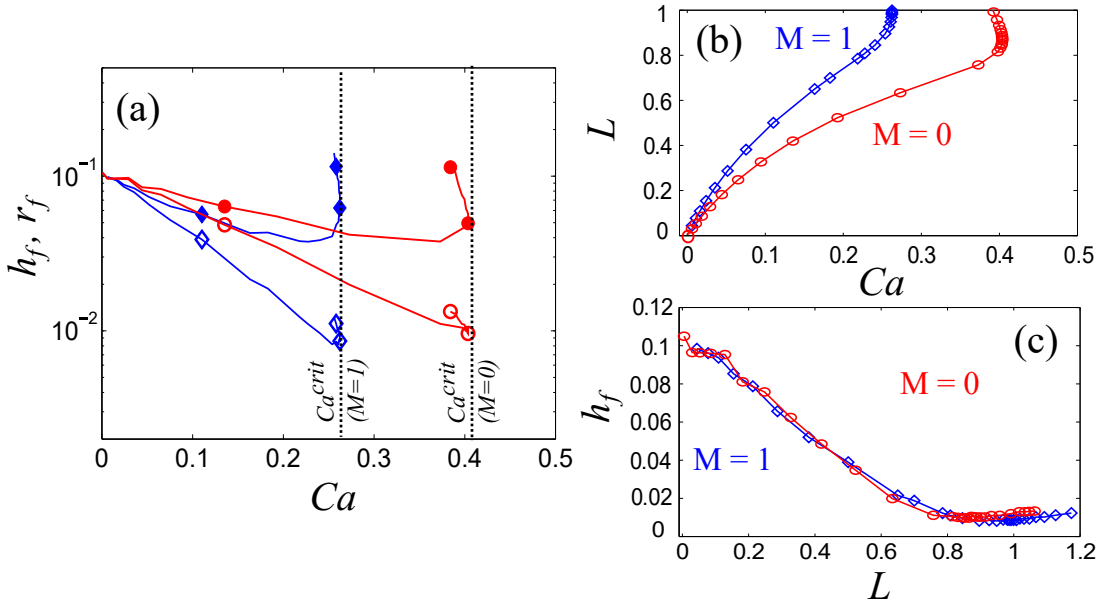

Figure 2.10: (a) Interfacial length scales r_f (closed symbols) and h_f (open symbols) as a function of Ca for $M = 1$ (blue diamonds) and $M = 0$ (red circles). (b) Interfacial length L plotted against Ca for $M = 1$ (blue diamonds) and $M = 0$ (red circles). (c) Inflection-point height h_f as a function of L for $M = 1$ (blue diamonds) and $M = 0$ (red circles). Other parameter values are $\chi = 10^{-3}$, $Pe = 10^3$, $\lambda = 10^{-4}$, and $\theta_{mic,B} = 90^o$.

2.7(b)-(c)). Note that in both cases L shows a sharp increase near Ca^{crit}, consistent with experimental observations in the absence of surfactants [7].

To see how the air-film thickness changes with the interface elongation, h_f is plotted as a function of L for $M = 0$ and $M = 1$ (Figure 2.10(c)). As expected, the film is thinned as the interface elongates. However, the results for both cases collapse onto the same curve, which further supports the observation that the mechanism for wetting failure is very similar in the presence and absence of Marangoni stresses. This plot also highlights the key role played by the IP position. The presence of Marangoni stresses thins the air film and moves the IP closer to the dynamic contact line, bringing the system closer to wetting failure.

2.5.3 Influence of M and Pe

As defined by (2.7), the Marangoni number measures the strength of Marangoni stresses relative to viscous stresses, with larger values of M corresponding to stronger Marangoni stresses. To satisfy the interfacial stress balance (2.5), the receding-phase shear stresses increase as M increases. As discussed in Sec. 2.5.2, this increase of shear stresses is produced by thinning of the air film, which in turn promotes the onset of wetting failure. As a result, the effect of Marangoni stresses on wetting failure is more pronounced as M increases (Figure 2.11(a)). Note that surfactant concentration gradients are very large near the dynamic contact line when $M \to 0$ and $Pe = 10^3$, which causes the hybrid model to diverge. For this reason, Ca^{crit} values in the $0 < M < 1$ regime are only shown in the inset of Figure 2.11(a), where $Pe = 1$.

As M increases, fluid displacement approaches an extreme case (Ca^{crit} value shows a plateau in Figure 2.11(a)), where the velocity magnitude $|V|$ of the fluid interface approaches zero, resulting in a no-slip condition [105]. This is because strong Marangoni stresses counteract the rolling motion in the advancing phase. Consequently, the interfacial velocity is lowered with increasing M as shown in Figure 2.11(b). Note that the x-coordinate in Figure 2.11(b) is the distance from the contact line. The origin of the x-coordinate represents the dynamic contact line, where the velocity is close to zero because of the Navier-slip boundary condition applied at the moving substrate [23].

Figure 2.12 shows the impact of the Peclet number (Pe) on wetting failure; Pe provides a measure of the ratio between convective and diffusive transport of surfactants

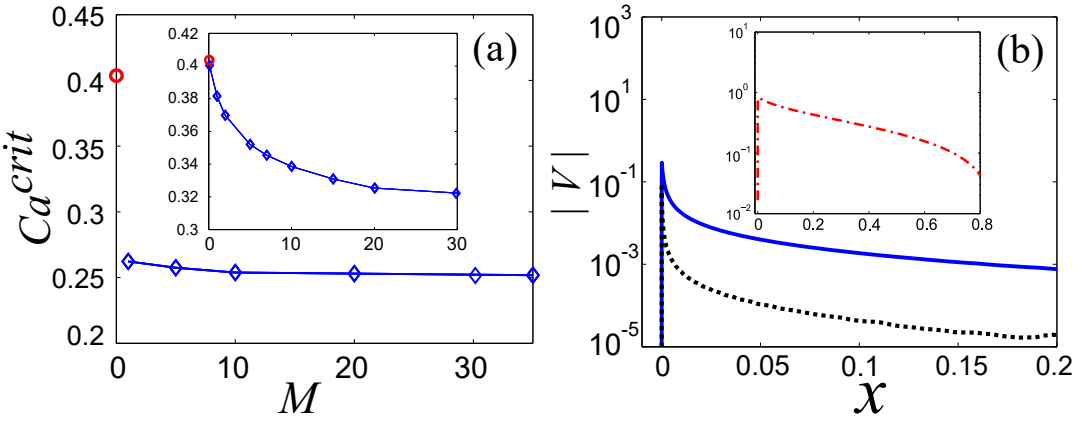

Figure 2.11: (a) Critical capillary number as a function of the Marangoni number (M) for $Pe = 10^3$. The data point for $M = 0$ is denoted as a red circle. *Inset*: Same plot but for $Pe = 1$. (b) Fluid-interface velocity magnitude at Ca^{crit} as a function of the distance from the contact line for $M = 1$ (blue solid line) and $M = 50$ (black dotted line) when $Pe = 10^3$. *Inset*: Velocity magnitude for $M = 0$. Other parameter values are $\chi = 10^{-3}$, $\lambda = 10^{-4}$, and $\theta_{mic,B} = 90^o$.

along the fluid interface. As diffusion becomes important (i.e., D_s increases and Pe decreases), Ca^{crit} increases, which means that surfactants with larger D_s can delay the onset of wetting failure. However, the systems with larger D_s reduce to the case where Marangoni stresses are absent (i.e., $M = 0$). This is because diffusion tends to smooth surfactant concentration gradients along the interface, leading to smaller effects from Marangoni stresses. Therefore, the Ca^{crit} value for $M = 1$ is the same as that for $M = 0$ when $Pe \leq 10^{-2}$.

2.6 Comparison of model predictions with experimental data

As mentioned in Sec. 2.1, surfactants can decrease the equilibrium surface tension and lower the static contact angle θ_s, and surface-tension gradients can induce Marangoni stresses. In this section, our model predictions are compared with experimental data from Burley and Kennedy [7], whose experimental setup is similar to our model geometry.

Burley and Kennedy recorded the critical speed U^{crit} at which wetting failure (i.e.,

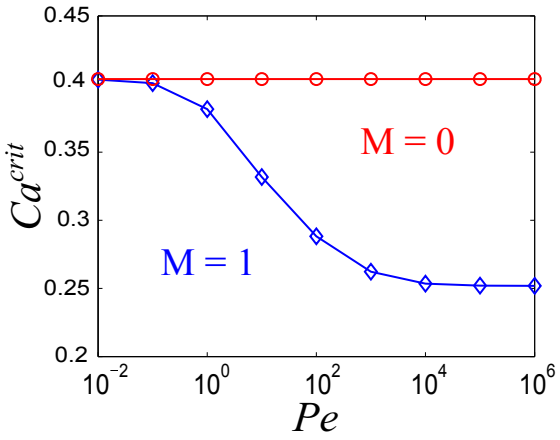

Figure 2.12: Critical capillary number as a function of the Peclet number (Pe) for $M = 1$ (blue diamonds) and $M = 0$ (red circles). Other parameter values are $\chi = 10^{-3}$, $\lambda = 10^{-4}$, and $\theta_{mic,B} = 90^o$.

air entrainment) occurs when a polyethylene terephthalate (PET) tape plunges into a liquid (glycerol/water) tank [7]. They found that the presence of Teepol detergent, which contains mixture of soluble surfactants, lowers the critical speed up to 17.5% (see U^{crit} in Table 2.1). To characterize the influence of surfactants on wetting failure, Ca^{crit} values are calculated based on the definition in (2.7) by substituting in the liquid viscosity μ and surface tension σ reported in the experimental study (see Ca^{crit} in Table 2.1).

Based on the experimental data, $M = 0$ (glycerol/water), $M = 1$ (glycerol/water/Teepol), and $\chi = 4 \times 10^{-4}$. In our previous study without surfactants [23], our full 2D FEM calculation accurately described experimental data in a similar geometry for $\lambda \leq 10^{-5}$. Therefore, $\lambda = 10^{-5}$ is chosen here. Since the static contact angles (θ_{mic}) are not given by Burley and Kenndy [7], we choose 67^o for glycerol/water system [26] and 50^o for glycerol/water/Teepol system. Note that the lowest limit of the hybrid model, 50^o, is picked due to the lack of contact-angle data in the literature for the glycerol/water/Teepol mixture on PET. In addition, because the type of Teepol is not specified in Burley and Kennedy's work, the diffusion coefficient D_s is chosen from values of common lab surfactants [106] ($D_s \sim 10^{-10}$ m^2/s) and, therefore, $Pe = 10^6$ for the model.

A comparison between model predictions and experimental values of U^{crit} shows

Source	Data M	θ_{mic} (deg.)	μ (cP)	σ (mN/m)	U^{crit}	Ca^{crit}
(a)						
Burley & Kennedy	Glycerol/water	-	45.6	62.3	0.581	0.425
This work	0	67	45.6	62.3	0.583	0.427
(b)						
Burley & Kennedy	Glycerol/water/Teepol	-	45.6	49.0	0.478	0.442
This work	0	60	45.6	49.0	0.474	0.441
This work	1	60	45.6	49.0	0.237	0.221
This work	1	50	45.6	49.0	0.242	0.225

Table 2.1: Comparison between model predictions and published experimental data in (a) surfactant-free and (b) surfactant-loaded systems. Other parameter values for the hybrid model are $\chi = 4 \times 10^{-4}$ and $\lambda = 10^{-5}$.

good agreement in the absence of surfactants (Table 2.1(a)). Surprisingly, U^{crit} calculated from the case $M = 0$ and $\theta_{mic} = 60^o$ matches the experimental value of U^{crit} in the presence of surfactants (Table 2.1(b)). However, when Marangoni stresses are present in the model ($M = 1$, $\theta_{mic} = 60^o$), the predicted critical speed U^{crit} is much smaller ($\sim 50\%$) than the experimental value. As θ_{mic} is lowered ($M = 1$, $\theta_{mic} = 50^o$), both U^{crit} and Ca^{crit} are increased, although these values are still much smaller than the experimental values.

Although uncertainty in the experimental values of the contact angle prevents us from drawing more definitive conclusions, the comparison shown in Table 2.1 suggests that changes in U^{crit} observed by Burley and Kennedy upon the addition of surfactants are likely produced by a lowering of the mean surface tension and equilibrium contact angle, rather than by Marangoni stresses. Marangoni stresses may still be present in the experiment, but their effects may be much weaker than predicted by our model due to surfactant solubility, which would tend to lower surface-tension gradients via transport between the fluid interface and bulk. Weaker Marangoni stresses (smaller Marangoni numbers) would raise the value of Ca^{crit} predicted by the model and likely bring it closer to the experimental value.

2.7 Conclusion

A hydrodynamic model is developed in this work to investigate the influence of insoluble surfactants on dynamic wetting failure. It is found that Marangoni stresses increase the

rate at which the dynamic contact angle in our geometry increases with contact-line speed, consistent with experimental observations of the behavior of receding contact angles in surfactant solutions [101, 102, 103]. The hydrodynamic model shows that 2D steady wetting fails at a critical substrate speed corresponding to a critical capillary number Ca^{crit}. When the receding phase has a viscosity much less than the advancing phase, the 1D approach overestimates Ca^{crit} and incorrectly predicts the direction of surfactant concentration gradients. However, since the 1D approach becomes more accurate as the viscosity of the receding phase increases, it may still be useful for studying liquid withdrawal or liquid-liquid displacement. The asymptotic theory of Cox [85] is found to match well predictions from the 1D/2D hybrid approach over a wide range of viscosity ratios.

Analysis of our results reveals that the physical mechanism for wetting failure is similar in the absence and presence of Marangoni stresses. Wetting failure occurs when the fluid interface cannot provide the pressure gradients needed to pump air away from the contact line. The presence of Marangoni stresses promotes the onset of wetting failure by thinning the air film, which increases receding-phase pressure gradients near the contact line but does not significantly change the capillary-pressure gradients there.

The results of the present work have allowed us to establish how insoluble surfactants influence wetting failure through Marangoni stresses, and to gain insight into the decades-old experimental observations of Burley and Kennedy. Our findings provide a strong motivation for accounting for surfactant solubility in future work, and for comparing model predictions to the other experimental observations in more complex geometries described in Sec. 2.1. The hybrid model introduced here provides an especially efficient way to explore this issue, since in processes such as slot coating and curtain coating the dominant effects of the receding phase will be produced by the thin air film near the contact line.

2.8 Appendix

2.8.1 Functions in 1D model

The formulation of the 1D model in Sec. 2.2.2 follows previous derivations [96, 97, 23]. However, we also consider the surface-tension-gradient term in tangential stress balance

equation (2.5). The function $F(h, Ca, \lambda, \chi, d\Gamma/dx, M)$ in (2.11) becomes:

$$\begin{aligned} F(h, Ca, \lambda, \chi, d\Gamma/dx, M) = -\big\{ & 3Ca[-Md\Gamma/dx(h^4(-1+\chi) - 2\lambda(1+4\lambda)\chi \\ & + h(-1+2\lambda+16\lambda^2)\chi + h^2(1+2\lambda)(-4\lambda(-1+\chi)+3\chi) \\ & + h^3(1-3\chi-2\lambda(1+\chi))) + 2(-h^2(-1+\chi)(3\chi+4\lambda\chi) \\ & + h\chi((-2+3\chi)+2\lambda(-3+4\chi)) \\ & + h^3(-1+\chi)\chi - \chi(\chi+4\lambda\chi))]\big\} \\ & /\big\{2h(h-1)(h^3(-1+\chi)+3\lambda(1+4\lambda)\chi + h(-2\lambda(-2+\chi) \\ & - 12\lambda^2(-1+\chi)+\chi) - h^2(-1+\lambda+2\chi+\lambda\chi)]\big\}. \end{aligned} \tag{2.22}$$

The function u in (2.12) becomes:

$$\begin{aligned} u = & (((-1+h)h\chi(Md\Gamma/dx(-h+h^2-4\lambda(1+4\lambda)) - 2((-1+h-4\lambda)\chi))) \\ & /(4(h^3(-1+\chi)+3\lambda(1+4\lambda)\chi + h(-2\lambda(-2+\chi) - 12\lambda^2(-1+\chi)+\chi) \\ & - h^2(-1+\lambda+2\chi+\lambda\chi))))/\chi. \end{aligned} \tag{2.23}$$

2.8.2 Finite-element method for hybrid model

We describe here some of the details associated with the Galerkin finite-element method (FEM) used to solve the governing equations of the hybrid model (Sec. 2.2.3).

Since FEM uses the weak form of the 2D governing equations [107], the normal and tangential stresses in (2.16) cannot be directly applied to the fluid interface, but must be converted into an effective traction vector:

$$\boldsymbol{n} \cdot \boldsymbol{T}|_{rec} = \{\chi n_y \frac{\partial u}{\partial y} - n_x p \ , \ -\chi n_x \frac{\partial u}{\partial y} - n_y p\}, \tag{2.24}$$

where subscripts indicate the x and y components of the normal vector $\boldsymbol{n}$ at the fluid interface. Note that (2.16) is recovered from the normal and tangential projections of (2.24). The velocity gradient can be expressed in terms of the pressure and interface height through (2.15).

The following weak-form residual is applied to the advancing phase and the fluid interface:

$$R^i_{\text{hybrid}} = -\int_S \phi_i \left(\frac{1}{Ca} \frac{\mathrm{d}\boldsymbol{t}}{\mathrm{d}s} + \boldsymbol{n} \cdot \boldsymbol{T}|_{rec} + \frac{\mathrm{d}\sigma}{\mathrm{d}s}\boldsymbol{t} \right) dS + \int_\Omega \phi_i \left(-\nabla^2 \boldsymbol{v} + \boldsymbol{\nabla} p \right) d\Omega, \tag{2.25}$$

where ϕ_i is the basis function, s is the interface arclength, Ω is the area of the advancing phase, and S is the interface length. Along the interface, $\mathrm{d}\boldsymbol{t}/\mathrm{d}s$ represents interface curvature and $(\mathrm{d}\sigma/\mathrm{d}s)\boldsymbol{t}$ is the surface-tension-gradient term. The unit normal vector $\boldsymbol{n}$ points toward the receding phase and the unit tangent vector $\boldsymbol{t}$ is in the same direction as the arclength s. The traction vectors of the receding phase, $\boldsymbol{n}\cdot\boldsymbol{T}|_{rec}$, act as "loading" terms that influence the flow of the advancing phase.

The receding phase also has a weak-form residual associated with it:

$$R^i_{\text{rec}} = \int_S \phi_i \left(Ah + \frac{1}{2}Bh^2 + \frac{1}{6}\frac{dp}{ds}h^3 \right) dS, \tag{2.26}$$

This residual is applied along the fluid interface. Note that the QP approximation ($dx \approx ds$) is applied in (2.14)-(2.15) to express pressure gradients with respect to the arclength s, which allows direct integration of weak-form residuals in FEM [32].

Along the fluid interface, surfactant transport is incorporated through the following weak-form residual:

$$R^i_{\text{surfactant}} = \int_S \phi_i \left(\boldsymbol{\nabla_s}\cdot(\boldsymbol{v_s}\Gamma) - \frac{1}{Pe}{\nabla_s}^2\Gamma \right) dS, \tag{2.27}$$

Because we assume that surfactants do not deposit onto solid boundaries, surfactant concentrations should satisfy the global constraint (2.9) to have a non-trivial solution.

In the advancing phase, biquadratic basis functions are used for velocity and linear discontinuous basis functions are used for pressure. Position variables (e.g., h) are described with biquadratic basis functions. Only the receding-phase pressure at the interface is needed [see (2.26)], so it and the surfactant concentration are also described with biquadratic basis functions. The nodes along the fluid interface can thus be thought of as forming "1D elements" for these variables.

Solution of the residual equations proceeds in a manner analogous to a full 2D FEM calculation [23, 31]. The physical system is mapped to a computational domain using elliptic mesh generation (which introduces additional residual equations) [107]. The field variables are represented by basis functions, and the resulting set of algebraic equations for the basis-function coefficients are then solved by the Newton-Raphson method using a frontal solver [108]. Note that the global constraint (2.9) is incorporated into the frontal solver through the Woodbury formula [109].

Chapter 3

Mechanisms of Dynamic Wetting Failure in the Presence of Soluble Surfactants

3.1 Introduction

3.1.1 Motivation

Dynamic wetting is the displacement of an ambient fluid by a liquid on a solid surface. In coating processes, steady dynamic wetting is a prerequisite for uniform deposition of a liquid layer on a moving substrate [82]. When the displacement process occurs at a critical substrate speed U^{crit}, the liquid fails to uniformly wet the substrate, resulting in unsteady flow and entrainment of the displaced phase between the liquid and the substrate. If air is the displaced phase, dynamic wetting failure leads to air entrainment: air bubbles are pinched off from a sawtooth-shaped dynamic contact line (DCL) [7, 110, 26]. [1]

Although wetting failure has attracted much attention due to its industrial importance [23, 31, 27, 10, 25, 111], relatively little is known about the influence of surfactants on this wetting transition. In addition to being of fundamental interest, this issue is of practical importance since surfactants are used in coating processes to lower surface

[1] This chapter has been accepted by Journal of Fluid Mechanics.

tension and enhance substrate wettability [64, 112]. If the distribution of surfactants along the fluid interface is nonuniform, surface-tension gradients (known as Marangoni stresses) arise and pull fluid from regions of low to high surface tension. Furthermore, the surfactants may be soluble in the bulk liquid, leading to surfactant exchange between the bulk and the fluid interface and substrate.

The objective of the present chapter is to investigate the influence of surfactant solubility on dynamic wetting failure using a hydrodynamic model and complementary experiments. As will be discussed below, prior experimental work has reported that surfactants influence the onset of wetting failure (i.e., the critical substrate speed U^{crit}) [7, 78, 9, 77], but the underlying mechanisms have not been clearly resolved.

3.1.2 Summary of related prior work

Burley and Kennedy [7] conducted plunge-coating experiments, where a substrate is pulled through a liquid pool, and reported critical substrate speeds U^{crit} for air entrainment. They found that the addition of surfactants (Teepol detergent) to a glycerol/water mixture lowers the critical substrate speed U^{crit} by 17.5% but increases the critical capillary number Ca^{crit} by 4%. The critical capillary number provides a measure of viscous forces relative to surface-tension forces at the onset of wetting failure, and has the definition $Ca^{crit} = \mu U^{crit}/\sigma$, where μ is the liquid viscosity and σ is the surface tension.

Prior modeling work suggests that U^{crit} and Ca^{crit} can be influenced by surfactants in the following three ways [83]. First, if the surfactants only reduce the equilibrium surface tension, then by dimensional analysis U^{crit} decreases but Ca^{crit} does not change. Second, if the surfactants decrease the static contact angle, both U^{crit} and Ca^{crit} would increase due to an increase in substrate wettability (assuming all other physical properties fixed). Third, if the surfactants produce Marangoni stresses, both U^{crit} and Ca^{crit} would decrease due to the thinning of air film near the DCL [83]. Note that, in general, all of these phenomena may occur simultaneously.

Although a reduction in equilibrium surface tension ($\sim$21.3%) is observed in the experiments of Burley and Kennedy [7], the influence of the latter two phenomena on the experimental value of U^{crit} is unclear since Burley and Kennedy did not report the change in the static contact angle produced by the addition of surfactants. This

motivates us to conduct an experimental study in which this change is measured.

In our prior work [83], we developed a hydrodynamic model to study the influence of Marangoni stresses produced by insoluble surfactants in a parallel-plate geometry where the top boundary is immobile and the bottom substrate moves horizontally at a speed U. Steady interface shapes were tracked as a function of substrate speed, and a critical substrate speed U^{crit} was identified beyond which no two-dimensional (2D) steady-state solutions could be found. This critical substrate speed corresponds to a critical capillary number Ca^{crit}.

The critical capillary number Ca^{crit} arises because capillary-stress gradients due to interface curvature near the DCL are no longer strong enough to provide the pressure gradients needed to pump the receding fluid (air) away from the DCL. The model shows that Marangoni stresses (directed away from the DCL) promote the onset of wetting failure by thinning the air film between the fluid interface and the substrate [83]. The thinner air film leads to larger pressure gradients in the air phase, making it more difficult for pressure gradients due to capillarity to remove the air from the DCL.

The model predictions were then used to interpret the experimental observations of Burley and Kennedy [7]. Since Burley and Kennedy did not report values of the static contact angles, these quantities had to be estimated. Although both the model and experiments show that surfactants decrease U^{crit}, the model underpredicts the value of U^{crit} by 50%, suggesting that Marangoni stresses in the system are overestimated. The difference in the value of U^{crit} may result from the assumption of insoluble surfactants in the model, whereas Teepol detergent contains soluble surfactants. In addition, the uncertainty in the experimental values of the static contact angle (as noted above) may also contribute to the difference in the value of U^{crit}. These factors prevent us from drawing more definitive conclusions about the important physical processes at play in the experiments of Burley and Kennedy [7].

Since surfactant solubility can weaken Marangoni stresses through exchange between the fluid interface and the bulk, one would expect that the predicted U^{crit} from a model accounting for surfactant solubility will be increased and thus closer to the experimental value. In addition, the uncertainty in the experimental values of the static contact angle (as noted above) may also contribute to the difference in the value of U^{crit}. Thus, our prior work provides a strong motivation to develop a model accounting for surfactant

solubility and to conduct complementary experiments in which both U^{crit} and the static contact angle are measured.

In addition to transport between the fluid interface and the bulk, surfactants can adsorb to the solid substrate as illustrated in prior experimental studies on dynamic wetting [79, 113, 114, 115]. The adsorption can occur as surfactants along the interface get carried to the DCL, and it can also occur as surfactants in the bulk liquid get transported to the substrate. Adsorption can influence the surfactant concentration distribution, and thus the surface tension along the fluid interface. To advance fundamental understanding of how this phenomenon influences dynamic wetting failure, it would be useful to incorporate substrate adsorption of surfactants (through the DCL and from the bulk liquid) into our model.

3.1.3 Overview of present chapter

Building on our prior work on insoluble surfactants [83], we develop a hydrodynamic model accounting for surfactant solubility and substrate adsorption in a parallel-plate geometry. An experimental study including plunge-coating experiments and characterization of liquid properties is conducted. Comparison of the model predictions and experimental observations provides insight into the physical mechanisms through which surfactants influence the onset of dynamic wetting failure. We note that the parallel-plate geometry was used to study dynamic wetting failure in the absence of surfactants, and the predictions of Ca^{crit} show good agreement with experimental observations for a feasible slip-length value [23, 31, 26].

The mathematical formulation and solution method for the hydrodynamic model are described in Section 3.2. In Section 3.3, we discuss the influence of surfactant solubility and substrate adsorption on Ca^{crit}. The experimental study is presented in Section 3.4. Comparisons of Ca^{crit} from experiments and the hydrodynamic model are made in Section 3.5. Conclusions are provided in Section 3.6.

3.2 Hydrodynamic model

The model problem we consider is illustrated in Figure 3.1(a). A receding fluid is displaced by an advancing liquid within a gap H, where the top boundary is held fixed

while the bottom boundary moves horizontally at a speed U. Viscosity is denoted by μ with subscripts being used to distinguish between properties of the advancing and receding fluids (i.e., μ_{adv} and μ_{rec}). Symbols x and y represent the Cartesian coordinates, and s is the arclength along the fluid interface (located at $y = h$) starting from the static (top) contact line. The horizontal length of the interface is denoted by L.

A schematic displaying the microscopic contact angle θ_{mic} and the macroscopic contact angle θ_M is shown in Figure 3.1(b). The microscopic angle (θ_{mic}) is formed between the fluid interface and the substrate and serves as a boundary condition in our model. In contrast, the macroscopic angle (θ_M) is measured at some distance away from the contact line due to the bending of the interface by viscous forces. In this work, the maximum angle along the fluid interface is designated as θ_M and corresponds to the inflection point (IP) of the fluid interface, whose height and radial distance from the DCL are denoted by h_f and r_f, respectively. Since the fluid interface contacts both horizontal boundaries, $\theta_{mic,T}$ and $\theta_{mic,B}$ in Figure 3.1(a) represent the microscopic contact angles at the top and bottom boundaries, respectively.

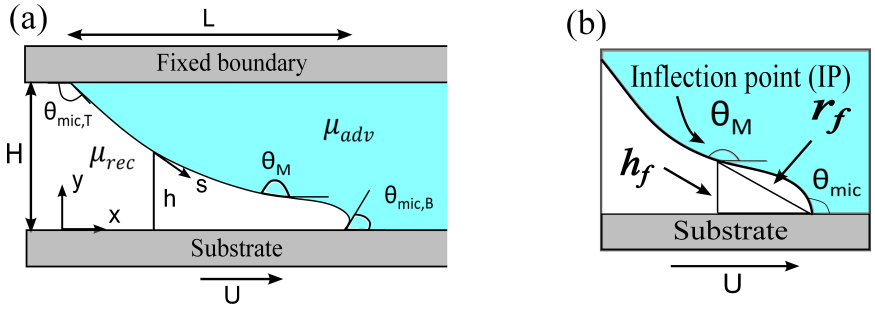

Figure 3.1: (a) Schematic of problem geometry. (b) Enlargement of contact-line region. The inflection point (IP) corresponds to the maximum interface angle (θ_M), and its height and radial distance are denoted by h_f and r_f, respectively.

3.2.1 Hydrodynamics

The steady Stokes equations describe the velocity $\boldsymbol{v}$ and pressure p in the advancing phase:

$$\boldsymbol{\nabla} \cdot \boldsymbol{v} = 0, \; \boldsymbol{\nabla} p = \nabla^2 \boldsymbol{v}. \tag{3.1}$$

The characteristic scales H, U, and $\mu_{adv}U/H$ are used to non-dimensionalize the lengths, velocities, and stresses, respectively.

Since the air phase is long and slender near the onset of wetting failure, lubrication theory can be applied to this phase to greatly reduce computational costs. The resulting 1D description of the air flow is given by the following equations [83, 32]

$$Ah + \frac{1}{2}Bh^2 + \frac{1}{6}\frac{dp}{ds}h^3 = 0, \tag{3.2}$$

$$\frac{\partial u}{\partial y}|_s = B + \frac{dp}{ds}h \quad \text{where} \quad A = \frac{\chi h + \chi\lambda u_{\mathrm{s}} - \frac{1}{2}\frac{dp}{ds}h^2\lambda}{\lambda + h}\ ,\ B = \frac{-\chi + A}{\lambda}, \tag{3.3}$$

where h is the interface height, p is the air pressure, $(\partial u/\partial y)|_s$ is the velocity gradient evaluated at the interface, u is the horizontal velocity component, and u_{s} represents u evaluated at the fluid interface. The symbol $\lambda = l_{slip}/H$ is a dimensionless slip length with l_{slip} being the dimensional slip length, and $\chi = \mu_{rec}/\mu_{adv}$ is the viscosity ratio.

In equations (3.2)-(3.3), the pressure gradients (dp/ds) use the quasi-parallel approximation $(dx \approx ds)$, where s represents the arclength coordinate along the interface [96, 97]. We note that this hybrid approach of a 1D description of the receding air and a 2D description of the advancing liquid has been used in our previous work [32, 83, 116]. The predictions of the onset of wetting failure from this hybrid approach are in excellent agreement with those obtained from a model using a 2D description of both the air and liquid flows in the absence of surfactants [32, 83]. The reliability of the hybrid approach in the absence of surfactants motivates us to use this approach to study wetting failure in the presence of surfactants.

The following dimensionless boundary conditions are applied along the fluid interface:

$$\boldsymbol{t}\cdot\boldsymbol{v}\,|_{adv} = u_s, \tag{3.4}$$

$$\boldsymbol{n}\cdot\boldsymbol{v} = 0, \tag{3.5}$$

$$M\boldsymbol{\nabla_s}\sigma\cdot\boldsymbol{t} = \boldsymbol{n}\cdot\boldsymbol{T}\cdot\boldsymbol{t}\,|_{adv} - \boldsymbol{n}\cdot\boldsymbol{T}\cdot\boldsymbol{t}\,|_{rec}, \tag{3.6}$$

$$\kappa(1/Ca + \sigma M) = \boldsymbol{n}\cdot\boldsymbol{T}\cdot\boldsymbol{n}\,|_{adv} - \boldsymbol{n}\cdot\boldsymbol{T}\cdot\boldsymbol{n}\,|_{rec}\ . \tag{3.7}$$

Equations (3.4)-(3.5) represent the no-slip and no-penetration conditions, and equations (3.6)-(3.7) correspond to interfacial stress balances in the tangential and normal

directions. At the fluid interface, unit normal vector $\boldsymbol{n}$ points toward the air phase and unit tangent vector $\boldsymbol{t}$ is in the same direction of the arclength coordinate s along the interface (Figure 3.1(a)).

In equations (3.6)-(3.7), $\boldsymbol{\nabla_s}\sigma$ indicates the surface-tension gradient along the interface, κ corresponds to the interface curvature, and $\boldsymbol{T}$ is the Newtonian stress tensor. The parameters $M = (\sigma_o - \sigma_m)/\mu_{adv}U$ and $Ca = \mu_{adv}U/\sigma_m$ are the Marangoni and capillary numbers, where σ_o denotes the surface tension of the solvent (i.e., surfactant-free solution) and σ_m is the surface tension corresponding to the mean surfactant concentration Γ_m at the interface. The Marangoni number M gives the relative strength of surface-tension-gradient forces (i.e., Marangoni forces) to viscous forces. When surfactants are absent, $\sigma_o = \sigma_m$ and the Marangoni stresses are zero. The capillary number Ca provides a measure of the strength of viscous forces relative to surface-tension forces.

A Navier-slip boundary condition is applied along the moving substrate to remove the stress singularity at the DCL [46, 92, 93, 94]:

$$\boldsymbol{t_s} \cdot (\boldsymbol{v} - \boldsymbol{U}) = \lambda \, [\boldsymbol{n_s} \cdot \boldsymbol{T} \cdot \boldsymbol{t_s}]. \tag{3.8}$$

Here, λ represents the dimensionless slip length defined earlier and $\boldsymbol{U}$ is the substrate velocity vector. Symbols $\boldsymbol{n_s}$ and $\boldsymbol{t_s}$ are unit vectors that are normal (pointing toward the fluids) and tangent to the substrate, respectively. This slip boundary condition is able to recover the no-slip condition ($\boldsymbol{v} \to \boldsymbol{U}$) at distances greater than l_{slip} away from the DCL. For simplicity, we assume that l_{slip} is the same in both the air and liquid phases. The no-slip boundary condition is applied to the top (fixed) boundary and the no-penetration condition is applied to both solid boundaries.

The ends of the fluid interface in the model are set by the microscopic contact angles θ_{mic} at the static contact line (top) and DCL (bottom) [22, 39]. Although θ_{mic} may depend on the substrate speed, material properties, and flow field [44, 117, 2, 98], here θ_{mic} is assumed to be constant and the same as the static contact angle θ_s [31, 98, 40, 45]. This assumption has been used in our prior work on the parallel-plate system in the absence of surfactants [31], and the predictions of the onset of wetting failure agree well with experimental observations for a feasible slip-length value.

3.2.2 Surfactant transport

In this chapter we study the influence of surfactant solubility and substrate adsorption on dynamic wetting failure. As will be discussed below, we use a model involving four parameters that account for adsorption (K) and desorption (α) of surfactants between the fluid interface and the bulk, and substrate adsorption through the DCL (K_{DCL}) and from the bulk (K_b). These processes are illustrated in Figure 3.2. More complex models accounting for phenomena such as micelle formation could be developed (e.g., [79]), but are beyond the scope of the present paper.

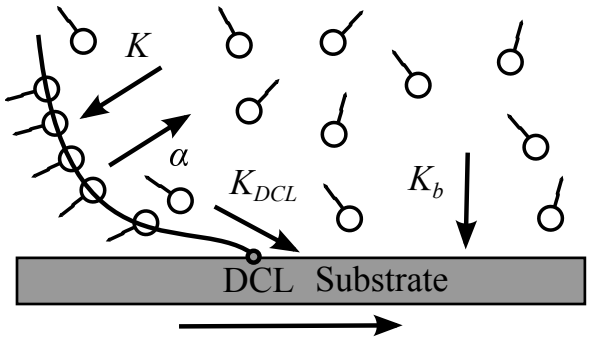

Figure 3.2: Schematic of surfactant adsorption/desorption near the dynamic contact line (DCL).

In the bulk, surfactant transport is described by a steady convection-diffusion equation:

$$\boldsymbol{v} \cdot \boldsymbol{\nabla} C = \frac{1}{Pe_b} \nabla^2 C, \tag{3.9}$$

where C represents the dimensionless surfactant concentration in the bulk scaled by a mean bulk concentration C_o. The bulk Peclet number $Pe_b = UH/D_b$ is defined using the bulk diffusion coefficient D_b, and shows the strength of surfactant convection relative to diffusion in the bulk.

Since we are interested in the possible influence of substrate adsorption of surfactants on dynamic wetting failure, the no-flux condition for surfactants is applied to the top boundary (Figure 3.1(a)). At the right boundary, a fixed dimensionless bulk concentration $C = 1$ is applied, acting as a surfactant reservoir. The conditions at the left and bottom boundaries will be discussed below.

A mass flux describes surfactant transport between the bulk and the fluid interface

(left boundary of the bulk; Figure 3.1(a)). At this location, the flux is given by

$$-\frac{1}{Pe_b}\boldsymbol{n}\cdot\boldsymbol{\nabla}C = K(C_s-\Gamma), \tag{3.10}$$

where C_s is the dimensionless bulk concentration there and Γ is the dimensionless surfactant concentration at the interface scaled by the mean surfactant concentration Γ_m. The solubility number $K = k_a\Gamma_\infty/U$ shows the ratio of the rates of adsorption (to the fluid interface) and convection, where k_a is the adsorption rate constant of surfactants and Γ_∞ is the concentration at which the interface is saturated [118, 71]. Following the convention of prior modeling work accounting for surfactant solubility [118, 71], the flux is non-dimensionalized by $U\Gamma_m/H$, so the bulk Peclet number Pe_b and the solubility number K show up in (3.10). The product of Pe_b and K gives the relative strength of adsorption to bulk diffusion. Note that larger K values correspond to less-soluble surfactants (i.e., surfactants tend to adsorb to the fluid interface).

A steady convection-diffusion equation is applied to the fluid interface to describe interfacial surfactant transport:

$$\boldsymbol{\nabla_s}\cdot(\boldsymbol{v_s}\Gamma) = \frac{1}{Pe_s}{\nabla_s}^2\Gamma + j_n, \text{ where } j_n = \alpha(C_s-\Gamma). \tag{3.11}$$

The symbol $\boldsymbol{\nabla_s}$ denotes the surface gradient operator, $\boldsymbol{v_s}$ is the interface velocity, and j_n is the flux between the bulk and the interface. The desorption number $\alpha = k_dH/U$ shows the strength of desorption (from the fluid interface) relative to convection, where k_d is the desorption rate constant at the fluid interface [118, 71]. Larger values of α result in more desorption of surfactants from the fluid interface. The surface Peclet number $Pe_s = UH/D_s$ is defined using the surface diffusion coefficient D_s, and shows the strength of surfactant convection relative to diffusion at the fluid interface. The product of Pe_s and α gives the relative strength of desorption to surface diffusion. Note that the desorption number α and the solubility number K are related by $\alpha\Gamma_m/HC_o = K$, where the mean bulk concentration C_o and the mean interfacial concentration Γ_m are related by the isotherm $C_o = \Gamma_m k_d/k_a\Gamma_\infty$.

As noted in Section 1, surfactants can adsorb to the substrate through the DCL or from the bulk liquid. To account for adsorption through the DCL, a mass flux of surfactants at the DCL is used:

$$-\frac{1}{Pe_s}\boldsymbol{t}\cdot\boldsymbol{\nabla}\Gamma = K_{DCL}\ \Gamma_s, \tag{3.12}$$

where Γ_s represents the dimensionless surfactant concentration at the DCL and $K_{DCL} = k_{DCL}H/U$ is the DCL adsorption parameter that shows the relative strength of adsorption (at the DCL) to convection, where k_{DCL} is the adsorption rate constant [119, 120, 90]. This boundary condition recovers the no-flux condition if $K_{DCL} = 0$, and the product of Pe_s and K_{DCL} gives the strength of adsorption (at the DCL) relative to surface diffusion. Note that since we are interested in the influence of substrate adsorption on wetting failure occurring at the DCL, we assume that surfactants do not deposit onto the top solid boundary. Therefore, the no-flux condition $\boldsymbol{t} \cdot \boldsymbol{\nabla}\Gamma = 0$ is applied at the top end of the fluid interface.

To describe surfactant adsorption from the bulk to the substrate, a mass flux is applied at the bottom boundary of the bulk (i.e., the interface between the bulk and moving substrate):

$$-\frac{1}{Pe_b}\boldsymbol{n} \cdot \boldsymbol{\nabla}C = K_b\, C_s, \tag{3.13}$$

where C_s represents the bulk surfactant concentration at the substrate, $\boldsymbol{n}$ is the unit normal vector pointing downward, and $K_b = k_bH/U$ is the bulk adsorption parameter that shows the relative strength of adsorption (at the bottom boundary) to convection, where k_b is the adsorption rate constant at the substrate [120, 121]. If $K_b = 0$, there is no adsorption of surfactants on the substrate. The product of Pe_b and K_b gives the strength of adsorption (at the bottom boundary) relative to bulk diffusion.

The surfactant transport equation (3.11) influences the tangential stress balance (3.6) through an the equation of state, a relationship between surface tension and interfacial surfactant concentration. Generally, surface tension depends logarithmically on surfactant concentration [65]. Here, we assume that the surfactant concentration is dilute enough to apply a linearized equation of state [90, 122, 123]:

$$\sigma = 1 - \Gamma. \tag{3.14}$$

In this equation, surface tension σ has been non-dimensionalized using the relation $\sigma' = \sigma_m + (\sigma_o - \sigma_m)\sigma$, where σ' represents the dimensional surface tension [91].

3.2.3 Solution method

The Galerkin finite element method is used to solve Equations (3.1)-(3.14); for details we refer readers to our previous work [23, 83]. The key dimensionless model parameters are

summarized in Table 3.1. For a given set of parameters, we seek steady-state solutions of the model that include interface shape, surfactant concentration along the interface and in the bulk, pressure in the air phase, and velocity and pressure in the liquid phase. We then track the macroscopic contact angle θ_M (i.e., the maximum contact angle along the interface; Figure 3.1) as a function of the capillary number Ca until a critical capillary number Ca^{crit} is located beyond which we are unable to find a steady-state solution. The value of Ca^{crit} from the solution path is assumed to correspond to the onset of wetting failure.

To isolate the influence of surfactant adsorption/desorption (i.e., K, α, K_{DCL}, and K_b) on wetting failure, we assume neutral and constant microscopic contact angles θ_{mic} at the top and bottom boundaries of the fluid interface (i.e., $\theta_{mic,T} = \theta_{mic,B} = 90^o$) in the parametric study of Section 3.3. In addition, the mean surface tensions σ_m are kept the same for systems in the absence and presence of surfactants. As a consequence, we can directly compare critical capillary numbers Ca^{crit} for different cases and determine whether a given phenomenon delays or promotes the onset of wetting failure (These assumptions are relaxed in Section 4 when we compare model predictions to experimental data.) We note that even when $\theta_{mic} = 90^o$, predictions of Ca^{crit} in absence of surfactants from the combined approach of a 1D description of the air and a 2D description of the liquid agree well ($< 5\%$ difference) with those from a model that uses a full 2D description of both the air and liquid phases [83]. This indicates that even for these large values of θ_{mic}, a 1D description of the air accurately describes the onset of wetting failure.

Parameter	**Representation**	**Physical meaning**
χ	μ_{rec}/μ_{adv}	viscosity ratio
λ	l_{slip}/H	dimensionless slip length
Pe_b	UH/D_b	convection rate/bulk diffusion rate
Pe_s	UH/D_s	convection rate/surface diffusion rate
M	$(\sigma_o - \sigma_m)/\mu_{adv}U$	surface-tension-gradient forces/viscous forces
Ca	$\mu_{adv}U/\sigma_m$	viscous forces/surface-tension forces
K	$k_a\Gamma_\infty/U$	adsorption rate/convection rate
α	k_dH/U	desorption rate/convection rate
K_{DCL}	$k_{DCL}H/U$	substrate adsorption rate at DCL/convection rate
K_b	k_bH/U	substrate adsorption rate in the bulk/convection rate

Table 3.1: Model parameters and corresponding physical meanings

3.3 Parametric study

In this section, we perform a parametric study to examine the influence of surfactant solubility and substrate adsorption on dynamic wetting failure. A viscosity ratio of $\chi = 5 \times 10^{-4}$ is chosen, which corresponds to the case where air is displaced by a liquid having a viscosity of ~ 40 cP. Following our prior work [83], a dimensionless slip length of $\lambda = 10^{-4}$ is used. If we take the characteristic length H to be the capillary length $l_{cap} = \sqrt{\sigma_0/\rho g}$ (where ρ is the liquid density) [23], then for $l_{cap} \sim 2$ mm, this value of λ corresponds to a dimensional slip length l_{slip} of ~ 0.2 μm. Smaller values of λ would decrease the Ca^{crit} values reported here, but do not affect the qualitative behavior we observe.

Using a value of $U \sim 0.1$ m/s, the value of H noted above, and data from prior studies of surfactant adsorption/desorption in aqueous solutions [124, 69], we find that $Pe_b \approx O(10^5)$, $Pe_s \approx O(10^4)$, $M \in [0-1]$, $K \in [10^{-2}-10]$, and $\alpha \in [10-10^5]$. To reduce the computational costs associated with resolving high concentration gradients while still remaining in a convection-dominated regime, we use the values of $Pe_s = 10^3$ and $Pe_b = 10^4$ in our calculations (Reducing these values weakens the influence of Marangoni stresses (see, for example, [83]).) We were not able to find values of K_{DCL} and K_b in the literature, so we simply vary the values of these parameters to study their qualitative influence on wetting failure.

3.3.1 Solubility number K

The macroscopic contact angle θ_M (Figure 3.1(b)) is extracted from the steady interface shape at a given value of the capillary number Ca and is used to construct a steady-state solution path (Figure 3.3(a)). By tracking steady-state solutions, we can locate a critical capillary number Ca^{crit} corresponding to a critical substrate speed U^{crit}. Beyond this value of Ca, we are unable to find 2D steady-state solutions, and assume that three-dimensional (3D) and/or transient flows develop. Thus, the value of Ca^{crit} from our calculations is taken to correspond to the onset of wetting failure and can be compared to experimental measurements.

We consider in this section the influence of the solubility number K. For our parametric study, we fix the desorption number α to a value of 350. We also neglect the

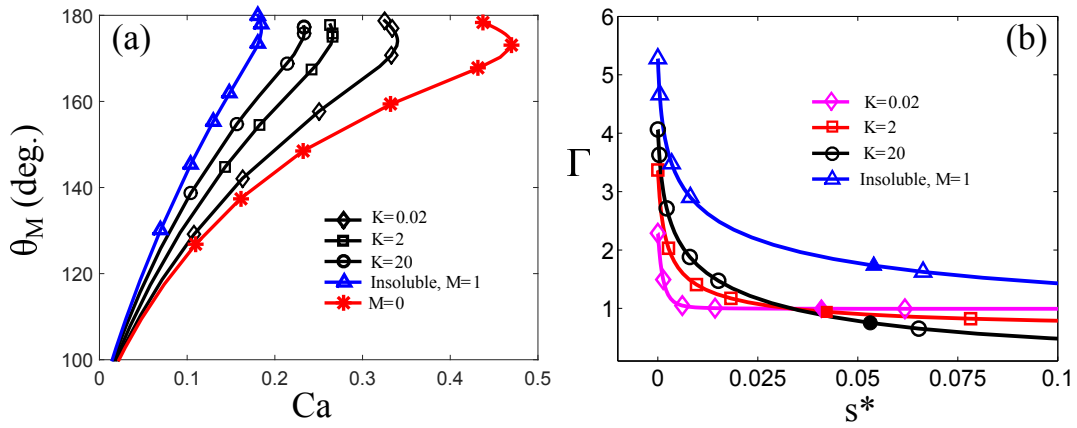

Figure 3.3: (a) Solution paths for $M = 0$ (red asterisks), insoluble surfactants when $M = 1$ (blue triangles), and soluble surfactants when $M = 1$ with various K values: $K = 20$ (black circles), $K = 2$ (black squares), and $K = 0.02$ (black diamonds). (b) Concentration profiles for insoluble surfactants (blue triangles) and soluble surfactants when $K = 20$ (black circles), $K = 2$ (red squares), and $K = 0.02$ (magenta diamonds). Solid symbols (at $s^* \approx 0.05$) represent the interface inflection point (IP). Concentration gradients at the IPs are $d\Gamma/ds = -12.6$ (insoluble surfactant), -9.26 ($K = 20$), -5.30 ($K = 0$), and -0.08 ($K = 0.02$). Values of other parameters are $\chi = 5 \times 10^{-4}$, $\lambda = 10^{-4}$, $Pe_s = 10^3$, $Pe_b = 10^4$, $\theta_{mic,B} = \theta_{mic,T} = 90^o$, $\alpha = 350$, and $K_{DCL} = K_b = 0$.

influence of substrate adsorption and thus set $K_{DCL} = K_b = 0$.

Figure 3.3(a) shows solution paths for several different cases: $M = 0$, insoluble surfactants when $M = 1$, and soluble surfactants when $M = 1$ and several different values of K. The results for insoluble surfactants are obtained using the model developed in our previous work [83], where an additional mass-conservation constraint is applied along the fluid interface. Figure 3.3(a) demonstrates that the presence of Marangoni stresses (i.e., the cases where $M = 1$) decreases Ca^{crit} and thus promotes the onset of wetting failure, which is consistent with the finding in our previous work [83]. As noted in Section 1, Marangoni stresses promote the onset of wetting failure by thinning the air film between the fluid interface and the substrate [83]. This leads to larger air-pressure gradients and makes it more difficult for capillary-stress gradients to pump air away from the DCL. Direct evidence of the thinning of the air film is given in Table 3.2, where the dimensionless film thicknesses h_f (Figure 3.1) are shown for the different cases in Figure 3.3(a) when $Ca = 0.15$.

Source	$\boldsymbol{h_f}$
$M = 0$	0.044
Soluble surfactant when $M = 1$ and $K = 0.02$	0.034
Soluble surfactant when $M = 1$ and $K = 2$	0.027
Soluble surfactant when $M = 1$ and $K = 20$	0.015
Insoluble surfactant when $M = 1$	0.005

Table 3.2: Dimensionless film thicknesses h_f for the different cases in Figure 3.3(a) when $Ca = 0.15$. Other parameter values are the same as in Figure 3.3(a).

As expected, surfactant solubility decreases Marangoni effects via transport between the fluid interface and the bulk. The Ca^{crit} values for soluble surfactants are larger than the value for insoluble surfactants. In addition, Ca^{crit} decreases as the solubility number K increases, meaning that more adsorption of surfactants to the fluid interface (i.e., less soluble surfactant) results in stronger Marangoni effects. Fitting the model predictions in Figure 3.3(a) yields a power-law relationship between Ca^{crit} and K, $Ca^{crit} \approx 0.28K^{-0.054}$. We note that the above results are for $\theta_{mic,B} = 90^o$. Our prior work on insoluble surfactants shows that changes in $\theta_{mic,B}$ (i.e., substrate wettability) from 45^o to 135^o lead to an $\sim$30% decrease in Ca^{crit} [83]; we would expect similar behavior for soluble surfactants.

Figure 3.3(b) shows the corresponding surfactant concentration profiles along the fluid interface. The concentration is shown as a function of s^*, the arclength coordinate *starting* from the DCL. In all cases, the surfactant concentration Γ reaches a maximum at $s^* = 0$, meaning that surfactants accumulate at the DCL. This is because the advancing liquid flow carries surfactants toward the DCL. In the advancing phase, the bottom substrate drags the liquid as it moves to the right. As a consequence, liquid near the fluid interface flows toward the substrate to conserve mass, resulting in a rolling-flow pattern (Figure 3.4) similar to those observed in prior experimental and computational work [24, 25, 23, 83]. Note that as the solubility number K decreases, the surfactant concentration at the DCL ($s^* = 0$) also decreases.

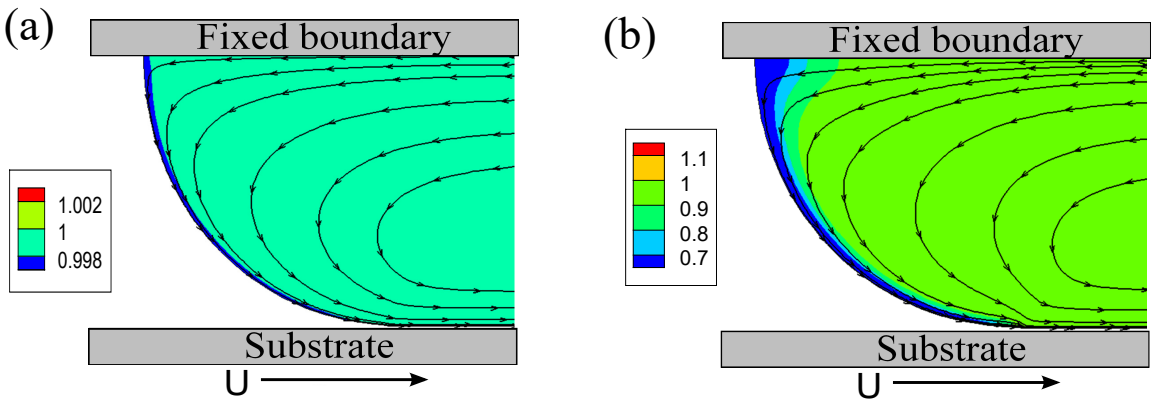

Figure 3.4: Concentration contours and streamlines for soluble surfactants when (a) $M = 1$, $K = 0.02$, and $Ca = 0.237$; (b) $M = 1$, $K = 20$, and $Ca = 0.340$. Note that $Ca = Ca^{crit}$ in both cases. Other parameter values are the same as in Figure 3.3.

The solid symbols in Figure 3.3(b) represent the interface inflection point (IP). From our previous work on insoluble surfactants [83], we found that Marangoni stresses directed away from the DCL (i.e., negative concentration gradient at the IP) will promote the onset of wetting failure by thinning the air film between the interface and the substrate. In Figure 3.3(b), the case of insoluble surfactants shows the most negative concentration gradient, meaning that Marangoni effects are the strongest and the Ca^{crit} value is the smallest among all the cases shown. In addition, the absolute value of the

concentration gradient decreases as K decreases (see values in figure caption). This is because the adsorption of surfactants from the bulk to the fluid interface becomes weaker as K decreases, resulting in less surfactant accumulation at the DCL.

Figure 3.4 shows contour plots of the concentration field along with streamlines for soluble surfactants when $K = 0.02$ and $K = 20$ at Ca^{crit}. Due to adsorption at the fluid interface, the bulk concentration near the interface is lower than that far away from the interface. In addition, as K increases, adsorption of surfactants becomes stronger, making the low-concentration region larger (Figure 3.4(b)).

3.3.2 Desorption number α

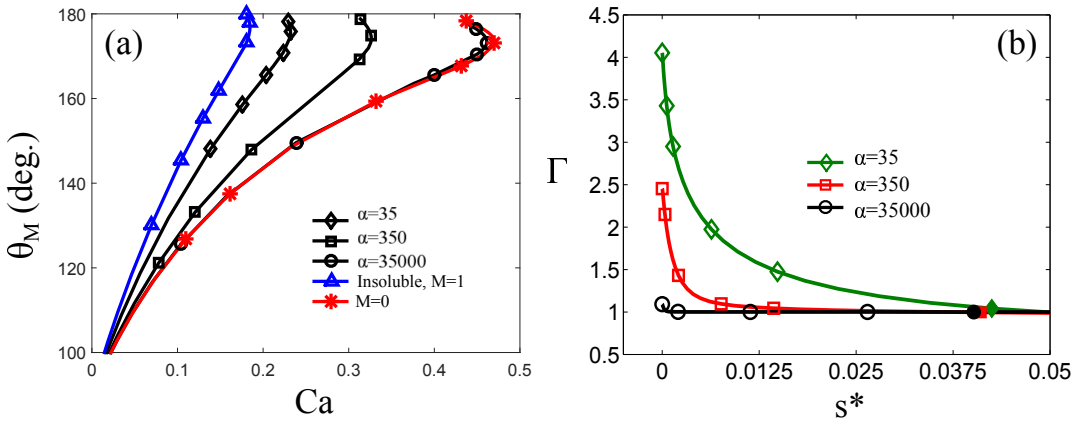

Figure 3.5: (a) Solution paths for $M = 0$ (red asterisks), insoluble surfactants when $M = 1$ (blue triangles), and soluble surfactants when $M = 1$ with various α values: $\alpha = 3.5 \times 10^4$ (black circles), $\alpha = 350$ (black squares), and $\alpha = 35$ (black diamonds). (b) Concentration profiles for soluble surfactants $M = 1$ when $\alpha = 35$ (green diamonds), $\alpha = 350$ (red squares), $\alpha = 3.5 \times 10^4$ (black circles). Solid symbols (at $s^* \approx 0.0375$) represent the interface inflection point (IP). Concentration gradients at the IPs are $d\Gamma/ds = -7.14$ ($\alpha = 35$), -0.89 ($\alpha = 350$), and -0.0089 ($\alpha = 3.5\times10^4$). Values of other parameters are $\chi = 5 \times 10^{-4}$, $\lambda = 10^{-4}$, $Pe_s = 10^3$, $Pe_b = 10^4$, $\theta_{mic,B} = \theta_{mic,T} = 90^o$, $K = 0.2$, and $K_{DCL} = K_b = 0$.

In Figure 3.5(a), we show solution paths for $M = 0$, insoluble surfactants when $M = 1$, and soluble surfactants when $M = 1$ and different values of α. Here, we fix the value of the solubility number K to a value of 0.2, and again neglect substrate adsorption ($K_{DCL} = K_b = 0$). As can be seen, Ca^{crit} increases as the desorption number

α increases, meaning that more desorption of surfactants leads to weaker Marangoni effects. In particular, when $\alpha = 3.5 \times 10^4$, the solution path as well as the Ca^{crit} value approach those for $M = 0$, indicating that Marangoni stresses are negligible. Fitting the model predictions in Figure 3.5(a) yields a power-law relationship between Ca^{crit} and α, $Ca^{crit} \approx 0.18\alpha^{0.091}$.

Figure 3.5(b) shows the corresponding concentration profiles along the fluid interface for soluble surfactants. The surfactant concentration is largest near the DCL, and its magnitude decreases as α increases (i.e., as desorption increases and Marangoni stresses become weaker). In addition, the concentration gradient at the IP decreases as α increases. For $\alpha = 3.5 \times 10^4$, the concentration profile is nearly uniform, consistent with the observation above that the solution path for this case is similar to that for $M = 0$. The contour plots for different values of α are similar to those for different values of K (Figure 3.4) so are not shown.

3.3.3 DCL adsorption parameter K_{DCL}

We now turn to the effects of surfactant adsorption to the substrate, first considering the case of adsorption through the DCL while neglecting adsorption from the bulk ($K_b = 0$). Figure 3.6(a) shows solution paths for several different cases: $M = 0$, insoluble surfactants when $M = 1$, and soluble surfactants when $M = 1$ and several different values of K_{DCL}. Clearly, Ca^{crit} increases as K_{DCL} increases, suggesting that adsorption of surfactants through the DCL has a significant effect on Marangoni stresses. Surprisingly, when $K_{DCL} = 1.2$ the Ca^{crit} value becomes larger than that for $M = 0$, meaning that the onset of wetting failure is delayed. Fitting the model predictions in Figure 3.6(a) yields a power-law relationship between Ca^{crit} and K_{DCL}, $Ca^{crit} \approx 0.50K_{DCL}^{0.17}$.

Figure 3.6(b) shows the corresponding concentration profiles along the fluid interface. Similar to Figure 3.3(b), the case of insoluble surfactants shows the most negative concentration gradient at the IP, whereas the absolute values of the concentration gradients are greatly reduced in the case of soluble surfactants (see values in figure caption). In addition, as K_{DCL} increases, more surfactant transfers from the fluid interface to the substrate through the DCL ($s^* = 0$), decreasing the surfactant concentration at the

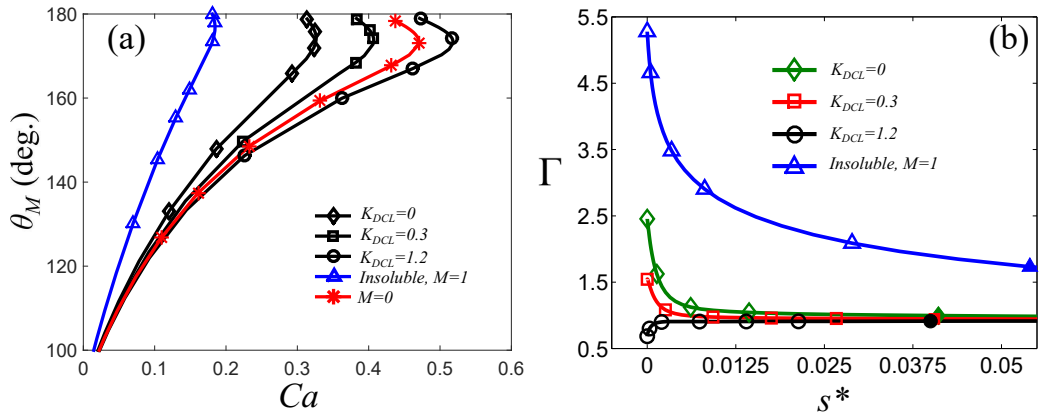

Figure 3.6: (a) Solution paths for $M = 0$ (red asterisks), insoluble surfactants when $M = 1$ (blue triangles), and soluble surfactants when $M = 1$ with various K_{DCL} values: $K_{DCL} = 0$ (black diamonds), $K_{DCL} = 0.3$ (black squares), and $K_{DCL} = 1.2$ (black circles). (b) Concentration profiles for insoluble surfactants (blue triangles) and soluble surfactants when $K_{DCL} = 0$ (green diamonds), $K_{DCL} = 0.3$ (red squares), and $K_{DCL} = 1.2$ (black circles). Solid symbols (at $s^* \approx 0.0375$) represent the interface inflection point (IP). Concentration gradients at the IPs are $d\Gamma/ds = -12.6$ (insoluble surfactant), -0.89 ($K_{DCL} = 0$), -0.28 ($K_{DCL} = 0.3$), and 0.16 ($K_{DCL} = 1.2$). Values of other parameters are $\chi = 5 \times 10^{-4}$, $\lambda = 10^{-4}$, $Pe_s = 10^3$, $Pe_b = 10^4$, $\theta_{mic,B} = 90^o$, $K = 0.2$, $\alpha = 350$, and $K_b = 0$.

DCL. Notably, if K_{DCL} is large enough (e.g., $K_{DCL} = 1.2$), the concentration gradient $d\Gamma/ds$ at the IP even changes its sign from negative to positive. For these large values of K_{DCL}, the substrate serves as a surfactant "sink" and prevents accumulation of surfactant there. As a consequence, the direction of the concentration gradient and Marangoni stresses at the DCL reverses.

Our previous work [83] showed that Marangoni stresses directed away from the DCL (i.e., negative concentration gradient at the IP) promote the onset of wetting failure by thinning the air film. The reversal of the direction of Marangoni stresses suggests that the air film is thickened, resulting in a delay in the onset of wetting failure. From our results, we found that at the same Ca value (e.g., $Ca = 0.47$) the characteristic air film thickness (h_f in Figure 3.1(b)) for $K_{DCL} = 1.2$ ($h_f = 0.0086$) is larger than that for $M = 0$ ($h_f = 0.0067$), corroborating the argument that thickening of the air film (by Marangoni stresses directed toward the DCL) delays the onset of wetting failure.

Since K_{DCL} changes the surfactant concentration primarily near the DCL, it has a negligible effect on the concentration distribution in the bulk. Thus, contour plots for different values of K_{DCL} are not shown.

3.3.4 Bulk adsorption parameter K_b

We now consider surfactant adsorption from the bulk to the substrate while neglecting adsorption through the DCL ($K_{DCL} = 0$). In Figure 3.7(a), we show solution paths for $M = 0$, insoluble surfactants when $M = 1$, and soluble surfactants when $M = 1$ and several different values of K_b. As can be seen, Ca^{crit} increases as K_b increases, implying that surfactant adsorption from the bulk can strongly influence Marangoni stresses. Notably, the value of Ca^{crit} for soluble surfactants with $K_b = 0.1$ is larger than that for $M = 0$, suggesting that adsorption of surfactants from the bulk can delay the onset of wetting failure. Fitting the model predictions in Figure 3.7(a) yields a power-law relationship between Ca^{crit} and K_b, $Ca^{crit} \approx 0.63K_b^{0.10}$.

Figure 3.7(b) shows the corresponding concentration profiles along the fluid interface. Interestingly, when $K_b \neq 0$, a local minimum in the concentration profiles appears, suggesting that Marangoni stresses change direction along the fluid interface (i.e., from directed away to directed toward the DCL as s^* increases). Because surfactants carried by the flow in the advancing phase cannot be transported through the DCL ($s^* = 0$)

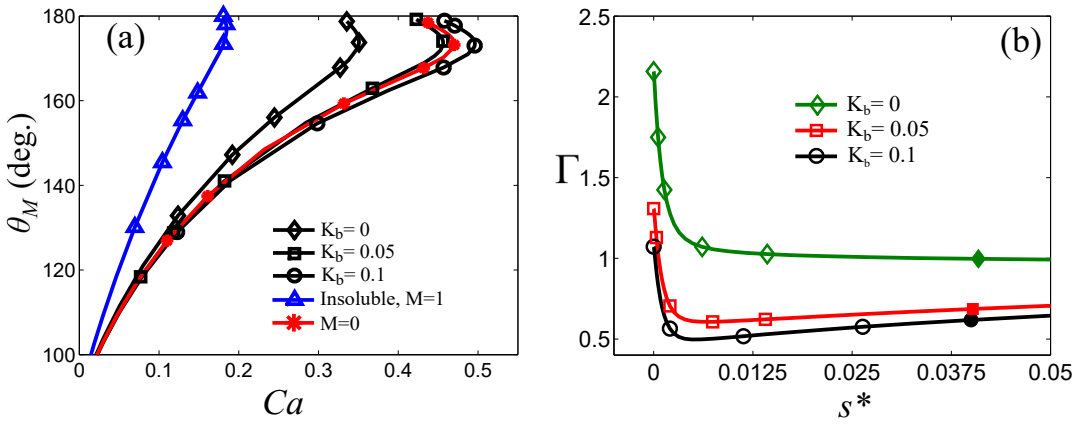

Figure 3.7: (a) Solution paths for $M = 0$ (red asterisks), insoluble surfactants when $M = 1$ (blue triangles), soluble surfactants when $M = 1$ with various K_b values: $K_b = 0$ (black diamonds), $K_b = 0.05$ (black squares), and $K_b = 0.1$ (black circles). (b) Concentration profiles for insoluble (blue triangles) and soluble surfactants when $K_b = 0$ (green diamonds), $K_b = 0.05$ (red squares), and $K_b = 0.1$ (black circles). Solid symbols (at $s^* \approx 0.0375$) represent the interface inflection point (IP). Concentration gradients at the IPs are $d\Gamma/ds = -0.57$ ($K_b = 0$), 2.11 ($K_b = 0.05$), and 2.80 ($K_b = 0.1$). Values of other parameters are $\chi = 5 \times 10^{-4}$, $\lambda = 10^{-4}$, $Pe_s = 10^3$, $Pe_b = 10^4$, $\theta_{mic,B} = 90^o$, $K = 0.2$, $\alpha = 550$ and $K_{DCL} = 0$.

since $K_{DCL} = 0$, they accumulate there, leading to the largest concentration values at $s^* = 0$. These values decrease as K_b increases.

Adsorption to the substrate acts as a surfactant sink and decreases the bulk concentration near the substrate. As a result, surfactants on the fluid interface near the bottom substrate desorb to equilibrate with the surfactant concentration in the bulk, resulting in a local minimum in the interfacial concentration profile. The minimum becomes more pronounced as K_b (adsorption to the substrate) increases. Note that in Section 3.3.3, no concentration minimum is created by substrate adsorption through the DCL, so the Marangoni stresses do not change sign.

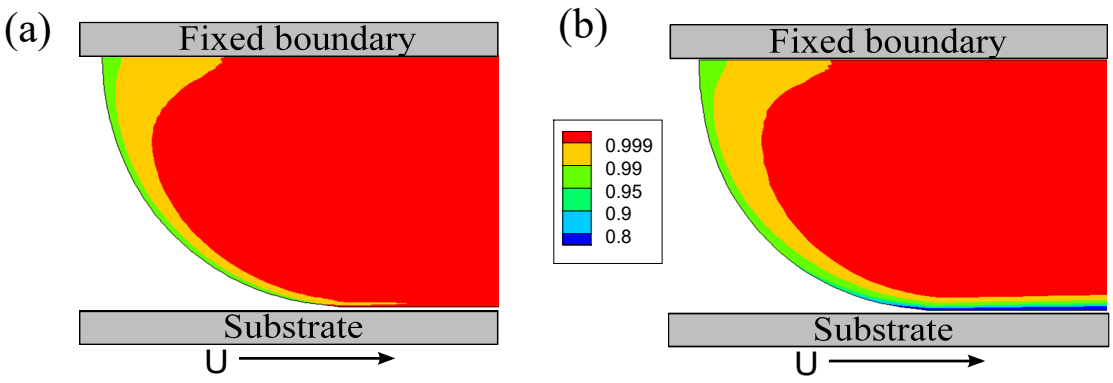

Figure 3.8: Concentration contours for soluble surfactants when (a) $M = 1$, $K_b = 0$, and $Ca = 0.35$; (b) $M = 1$, $K_b = 0.1$, and $Ca = 0.50$. Note that $Ca = Ca^{crit}$ in both cases. Other parameter values are the same as in Figure 3.7.

To understand how the concentration minimum influences Ca^{crit}, it is instructive to compare the concentration gradient values ($d\Gamma/ds$) at the IP: -0.57 ($K_b = 0$), 2.11 ($K_b = 0.05$), and 2.80 ($K_b = 0.1$). When $K_b = 0$, the Marangoni stresses point away from the DCL (due to the negative value of $d\Gamma/ds$), indicating that Marangoni stresses promote the onset of wetting failure.

When $d\Gamma/ds$ is positive, one might expect that Marangoni stresses will delay the onset of wetting failure (i.e., lead to a larger value of Ca^{crit} compared to $M = 0$). However, when $K_b = 0.05$, Ca^{crit} is still smaller than that for $M = 0$. This is because the negative concentration gradients near the DCL (i.e., Marangoni stresses pointing away from the DCL) compete with the positive ones near the IP (i.e., Marangoni stresses pointing toward the DCL). In this case ($K_b = 0.05$), the negative concentration gradients

near the DCL dominate and lead to a decrease in Ca^{crit} (compared to $M = 0$). As the value of K_b further increases, the concentration gradients near the IP become more positive. When $K_b = 0.1$, the positive concentration gradients near the IP dominate. As a result, the onset of wetting failure is delayed and Ca^{crit} becomes larger than that for $M = 0$.

The competition between the Marangoni stresses is reflected in the behavior of the characteristic air film thickness (h_f in Figure 3.1(b)). Recall that as the air film is thinned, the onset of wetting failure is promoted since capillary-stress gradients become less effective at removing air from the DCL [83]. When $Ca = 0.46$, the air film for soluble surfactants with $K_b = 0.1$ ($h_f = 0.0072$) is thicker than that for $M = 0$ ($h_f = 0.0070$) and $K_b = 0.05$ ($h_f = 0.0066$), suggesting that Ca^{crit} for $K_b = 0.1$ has the largest value among these three cases, consistent with Figure 3.7(a). For $K_b = 0.05$, the film thickness is thinner than that for $M = 0$, meaning that Ca^{crit} will be smaller than that for $M = 0$, again consistent with Figure 3.7(a).

Figure 3.8 shows contour plots of the concentration field for soluble surfactants when $K_b = 0$ and $K_b = 0.1$ at Ca^{crit}. Similar to Figure 3.4, the bulk concentration near the interface is lower than that far away from the interface. However, when surfactants in the bulk adsorb to the substrate, a region of low concentration appears near the substrate (Figure 3.8(b)).

3.4 Experimental study

To complement our model predictions, we have also conducted an experimental study. Below we describe the experimental apparatus and liquid characterization. A comparison between the experimental data and model predictions is performed in Section 3.5

3.4.1 Experimental apparatus

A schematic of our experimental apparatus is shown in Figure 3.9(a) [26]. A transparent PET (polyethylene terephthalate) tape moves through a vessel with one side of the tape in contact with liquid and the other in contact with a glass support. A 125 μm thick and 2 inch wide tape is used for all of the experiments reported in this chapter. Before

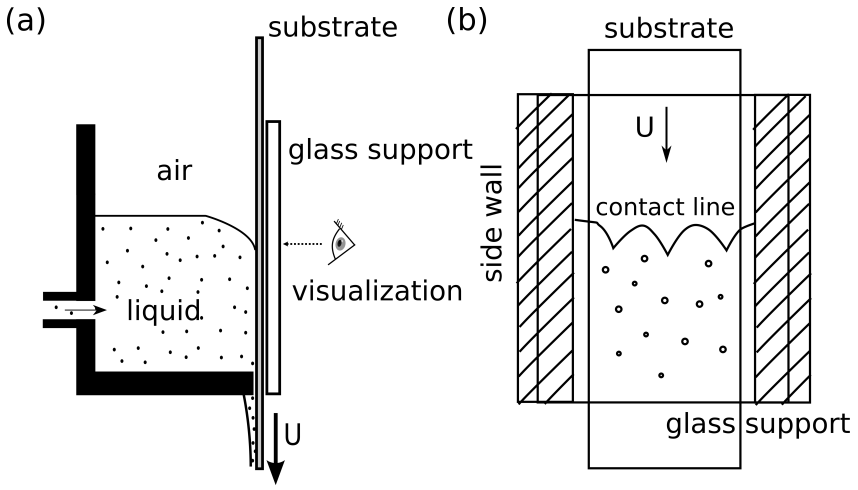

Figure 3.9: (a) Schematic of experimental apparatus, which is similar to the design used in [26]. (b) Front view of apparatus. Contact-line behavior is visualized through a glass support plate located to the right of the substrate in panel (a).

an experiment (i.e., tape is immobile), ∼250 ml of liquid is fed through an inlet located at the back of the vessel. Once the vessel is filled with the desired amount of liquid, the inlet is shut off to avoid creating flows in the vessel during an experiment. A high-speed camera is used to visualize contact-line behavior through the glass support as the tape speed increases (Figure 3.9(b)). A plate can be inserted into the tank to confine the meniscus [26], but since we wish to focus on the influence of surfactants in the absence of meniscus confinement, the plate is not used here.

The vessel acts like a plunge-coating tank, similar to the apparatus used by Burley and Kennedy [7]. However, the advantage of our design is that one can directly visualize DCL behavior. In this work, wetting failure is signaled by the appearance of triangular air films at the DCL as the tape speed increases. The corresponding tape speed is designated as the critical substrate speed U^{crit}. For each liquid, three experiments are carried out to assess the reproducibility of the critical speed. The triangular films are sensitive to disturbances and can quickly rupture, leaving behind air bubbles that are entrained in the bulk liquid. More details about the shape and thickness of these films in the absence of surfactants can be found in [26]. The key features of the air films (e.g., width, thickness, and space) are largely insensitive to the presence of surfactants (see Appendix 3.7.2).

3.4.2 Liquid characterization

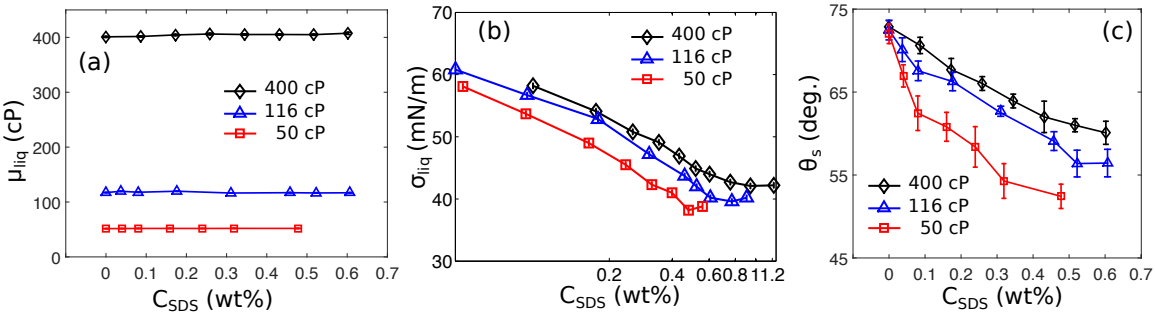

Figure 3.10: Characterization of solutions with various sodium dodecyl sulphate (SDS) concentrations: (a) viscosity, (b) surface tension, and (c) static contact angle on PET substrates for μ_{liq} = 400 cP (black diamonds), μ_{liq} = 116 cP (blue triangles), and μ_{liq} = 50 cP (red squares).

The liquids used in this study are glycerol/water solutions. The surfactant used is sodium dodecyl sulphate (SDS) (Sigma-Aldrich ReagentPlus®). During solution preparation, we found that the solubility of SDS in glycerol/water mixtures is low, especially for highly viscous solutions. Small SDS clumps remain in the mixture even after stirring and waiting overnight. As a result, SDS is dissolved in deionized water first, and pure glycerol is added afterward. The resulting glycerol/water/SDS mixture is stirred and left to rest overnight to dissipate large air bubbles and equilibrate with the laboratory temperature.

Three liquid viscosities, μ_{liq} = 400 cP, 116 cP, and 50 cP, are used in this study. The viscosities are obtained from an AR-G2 rheometer (TA Instruments), which shows that the viscosity is independent of shear rate in the range between 1 s^{-1} and 900 s^{-1}. The mean liquid viscosities are plotted as a function of surfactant concentration C_{SDS} in Figure 3.10(a), and do not change with the addition of surfactants throughout the range of C_{SDS} investigated. Note that in the plunge-coating experiments, the shear rate (based on the web speed and capillary length) is between 10 s^{-1} and 100 s^{-1}. The value of U^{crit} increases as μ_{liq} decreases, meaning that more tape needs to be used in a given experiment. Because of the limited supply of tape, we do not use liquids with a viscosity below 50 cP.

The surface tensions of the solutions are obtained from a Krüss K10ST digital tensiometer (Figure 3.10(b)). As expected, the surface tension decreases as the surfactant concentration increases. We can determine the critical micelle concentration (CMC) from the point where the slope of the surface-tension curve changes as C_{SDS} increases. The CMC for each liquid viscosity is $C_{SDS} \approx 0.94$ wt% ($\mu_{liq} = 400$ cP), $C_{SDS} \approx 0.77$ wt% ($\mu_{liq} = 116$ cP), and $C_{SDS} \approx 0.47$ wt % ($\mu_{liq} = 50$ cP). This increase in CMC with glycerol content (i.e., liquid viscosity) is consistent with prior experimental observations for SDS and other ionic/nonionic surfactants [66, 125, 126]. Note that solutions with $C_{SDS} <$ CMC are used in the plunge-coating experiments to be more consistent the dilute-surfactant assumption of the model.

Figure 3.10(b) also shows that the surface tension depends on the liquid viscosity. At a fixed surfactant concentration, a lower liquid viscosity corresponds to a smaller value of surface tension. This is because there is more aqueous surfactant solution in the less viscous liquids. This finding is similar to what is observed for SDS and sodium tetradecyl sulphate (STS) in prior experiments [127, 128].

Static contact angles on the PET tape are measured by the sessile drop method using a Krüss DSA goniometer. The influence of surfactants on the contact angles is shown in Figure 3.10(c). Due to the reduction in surface tension, the contact angle decreases as C_{SDS} increases, consistent with the Young's equation [65]. Similarly, since a less viscous liquid corresponds to a smaller value of surface tension, the contact-angle values decrease as the liquid viscosity decreases. Note that the static contact angles reported here will be used as the boundary condition at the DCL in our model ($\theta_{mic,B}$ in Figure 3.1(a)).

3.5 Comparison of Ca^{crit} from experiments and model predictions

Air entrainment occurs above a critical substrate speed U^{crit}, at which the contact line forms triangular air films. Air bubbles are generated when the films rupture. The speed U^{crit} from our experiments (Section 3.4) is plotted as a function of SDS concentration C_{SDS} for the three liquid viscosities (Figure 3.11(a)). As can be seen, the critical speed decreases as the surfactant concentration increases at a given liquid viscosity. In

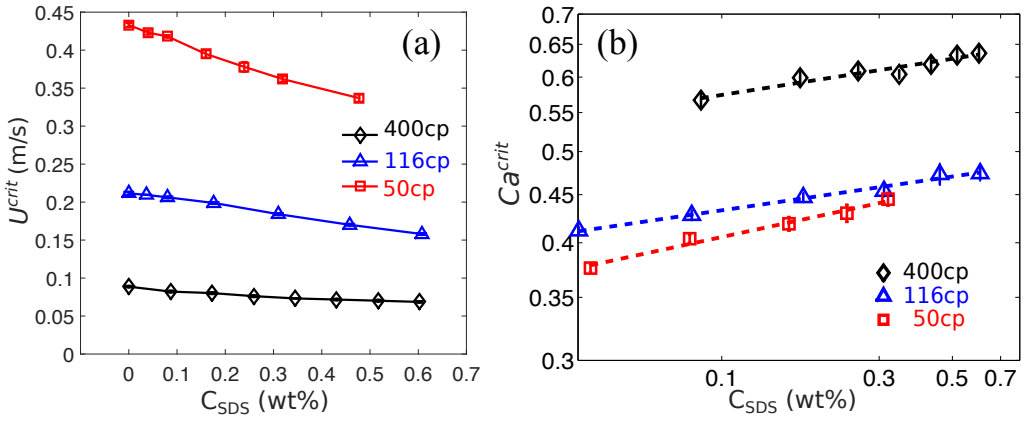

Figure 3.11: (a) Critical speed U^{crit} and (b) critical capillary number Ca^{crit} for μ_{liq} = 400 cP (black diamonds), μ_{liq} = 116 cP (blue triangles), and μ_{liq} = 50 cP (red squares). The solid lines in (a) are drawn to aid visualization. The dashed lines in (b) correspond to power law fittings of Ca^{crit} for three liquids: $Ca^{crit} \sim C_{SDS}^{0.055}$ (black, μ_{liq} = 400 cP), $Ca^{crit} \sim C_{SDS}^{0.051}$ (blue, μ_{liq} = 116 cP), $Ca^{crit} \sim C_{SDS}^{0.076}$ (red, μ_{liq} = 50 cP). For reference, the values of Ca^{crit} when $C_{SDS} = 0$ are 0.545 (μ_{liq} = 400 cP), 0.379 (μ_{liq} = 116 cP), and 0.336 (μ_{liq} = 50 cP).

addition, surfactants have a larger effect on U^{crit} at lower liquid viscosities.

We also note that lower critical speeds occur at higher liquid viscosities, consistent with prior experiments [26]. This can be understood by considering the case where surfactants are absent. At fixed interfacial tension and microscopic contact angle, higher liquid viscosities promote greater interface bending, leading to larger capillary-stress gradients and air-pressure gradients (due to a thinner air film). However, the air-pressure gradients increase more rapidly than the capillary-stress gradients as the liquid viscosity increases, so wetting failure occurs at a lower critical speed [129].

Figure 3.11(b) shows the corresponding values of the critical capillary number Ca^{crit}. As can be seen, Ca^{crit} increases with the liquid viscosity, consistent with prior experimental observations [26, 7, 8, 2, 24]. In addition, at a fixed liquid viscosity Ca^{crit} increases with C_{SDS}, showing the same trend as that reported by Burley and Kennedy [7].

To generate predictions of Ca^{crit} from the model, the viscosity ratio $\chi = \mu_{air}/\mu_{liq}$ is calculated based on the air and liquid viscosities. The Marangoni number $M = (\sigma_o - \sigma_m)/\mu_{liq}U^{crit}$ is obtained using the surface tension σ_m , and the surface tension

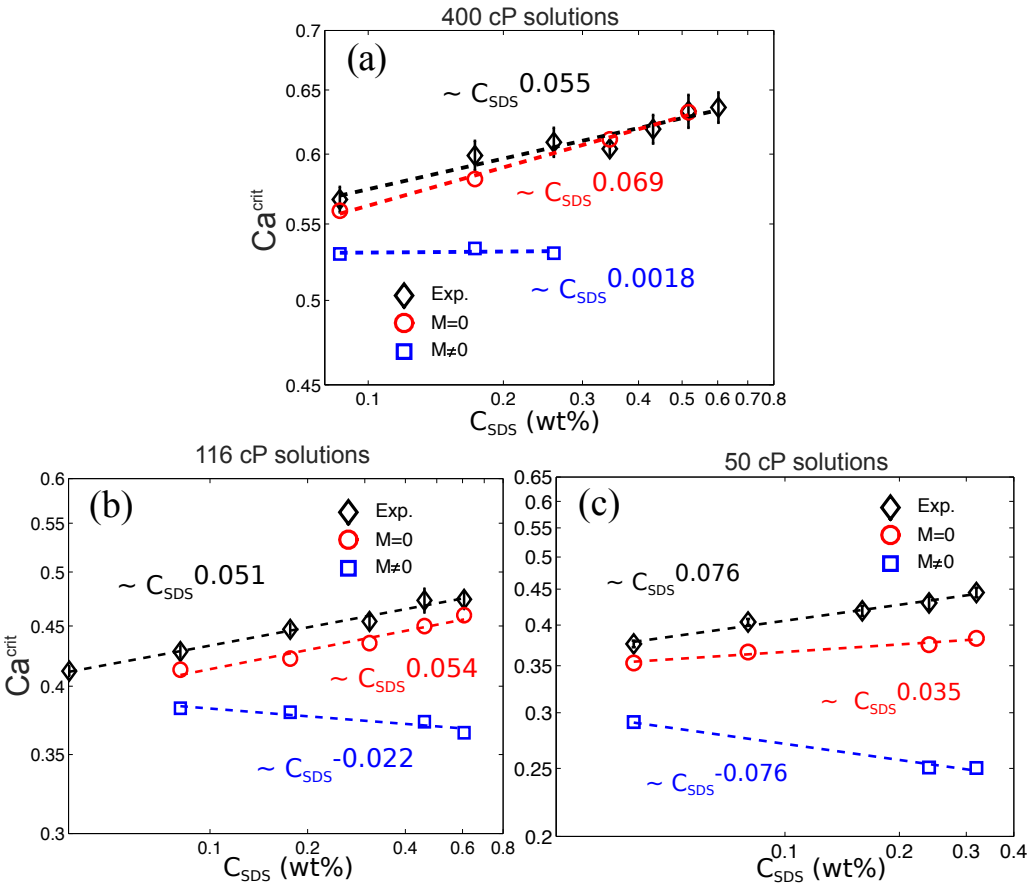

Figure 3.12: Comparison of model predictions with experimental data for (a) $\mu_{liq} = 400$ cP, (b) $\mu_{liq} = 116$ cP, and (c) $\mu_{liq} = 50$ cP. In each panel, symbols correspond to Ca^{crit} from our experiments (black diamonds), our model when $M = 0$ (red circles), and our model when $M \neq 0$ (blue squares). Dashed lines correspond to power-law fits of each data set. See appendix 3.7.3 for model parameters for each data point.

σ_o of the corresponding glycerol/water mixture when $C_{SDS} = 0$. Note that the value of M increases (from ∼0.1 to 1) as C_{SDS} increases due to the changes in σ_m and U^{crit}. The microscopic contact angles $\theta_{mic,B}$ at the DCL are set equal to the corresponding static contact angles (Section 3.4.2) at each value of C_{SDS}.

The capillary length $l_{cap} = \sqrt{\sigma_m/\rho g}$ is used as the characteristic length scale H when calculating various parameters (Table 3.1), where ρ and g are the liquid density and the gravitational acceleration, respectively. For the liquids used here, $l_{cap} \sim 2$ mm - 2.3 mm. Since l_{cap} is much less than the tank width (~ 10 cm), the effects of meniscus confinement are negligible and it is appropriate to take l_{cap} as the characteristic length scale [23, 26]. The Reynolds numbers in the advancing and receding phases (based on the susbstrate velocity and capillary length) in the experiments are at most ∼20 and ∼65, respectively, which are much below the values where inertia significantly affect the value of Ca^{crit} [31].

Since exact experimental values of the diffusion coefficients (D_b and D_s) and rate constants for adsorption k_a and desorption k_d are difficult to measure, we estimate these values from prior experimental studies of aqueous solutions [124, 69]. These values are used to calculate the Peclet numbers (Pe_b and Pe_s), the solubility number K, and the desorption number α in our experiments. Inevitably, this creates a high level of uncertainty since our liquids are more viscous than those used in prior studies. Note that although we use the same dimensional values of k_a and k_d for all calculations, K and α change as C_{SDS} does due to the changes in U^{crit} and l_{cap}. The values of Pe_b and Pe_s also change as C_{SDS} does, but because these are always very large, for simplicity we set $Pe_b = 10^5$ and $Pe_s = 10^4$. This corresponds to a convection-dominated limit where the results are insensitive to further increases in the Peclet numbers [83]. Since we do not have any experimental data for the parameters controlling surfactant adsorption to the substrate, K_{DCL} and K_b, we set these parameters to zero.

The dimensionless slip length λ ($\lambda \leq 10^{-5}$) is treated as an adjustable parameter. For a given liquid, its value is varied until the prediction for Ca^{crit} at $C_{SDS} = 0$ agrees with the experimental value. This value of λ is then used for all calculations at non-zero C_{SDS}. In this work, $\lambda \sim 10^{-6} - 10^{-5}$, which corresponds to dimensional slip lengths $\sim 2 - 20$ nm, values comparable to those used in our prior work on wetting failure in the absence of surfactants [23, 31, 26].

In Figure 3.12, we plot the experimental values of Ca^{crit} for each liquid as a function of C_{SDS}, along with the corresponding model predictions. In addition to the predictions for $M \neq 0$, we also show predictions from calculations where we set $M = 0$. The $M = 0$ predictions allow us to assess how well the experimental behavior can be described by simply accounting for changes to the mean surface tension and static contact angle. To facilitate comparison between the experimental values and model predictions, we also fit power-law relationships to the data in the plots. These are shown with dashed lines and the power-law exponents are given in the plots.

For the 400 cP case, Figure 3.12(a) shows that the predictions when $M = 0$ agree much better with the experimental data compared to the predictions when $M \neq 0$. The predictions for $M \neq 0$ indicate that Ca^{crit} is nearly independent of C_{SDS}, whereas the predictions for $M = 0$ show that Ca^{crit} increases as C_{SDS} does, consistent with the experimental data.

We have also performed calculations (not shown for brevity) where we have varied the parameters controlling surfactant adsorption to the fluid interface, K and α, over a physically reasonable range of values. However, we are unable to match the experimental values of Ca^{crit}. Similarly, reducing the value of $\theta_{mic,B}$ to account for the possibility that the local surfactant concentration at the DCL may be higher than the given value of C_{SDS} also does not lead to agreement with the experimental data.

If the parameters controlling surfactant adsorption to the substrate, K_{DCL} and K_b are made non-zero, it is possible to obtain agreement, but experimental values of these parameters are unknown. This suggests that for the 400 cP solutions, the simplest explanation consistent with the experimental data is that the increase in Ca^{crit} with C_{SDS} can largely be understood just by accounting for changes to the mean surface tension and static contact angle when surfactants are present.

For the 116 cP case, Figure 3.12(b) shows that the predictions for $M = 0$ are again in much better agreement with the experimental data than those for $M \neq 0$. Indeed, in this case, the $M \neq 0$ calculations predict that Ca^{crit} decreases as C_{SDS} increases, which is opposite to what is observed experimentally. The predictions for $M = 0$ are slightly below the experimental data, but can be brought into better agreement if a lower value of $\theta_{mic,B}$ is used (to account for a higher local surfactant concentration at the DCL, as noted above). Varying the values of K, α, and $\theta_{mic,B}$ over a physically reasonable range

does not lead to a match between the $M \neq 0$ predictions and the experimental data. As with the 400 cP solutions, this suggests that the experimental data can largely be explained just by accounting for changes to the mean surface tension and static contact angle when surfactants are present.

For the 50 cP solutions, Figure 3.12(c) shows that the $M = 0$ predictions are once more in better agreement with the experimental data, and that the $M \neq 0$ calculations again predict that that Ca^{crit} decreases as C_{SDS} increases. However, the discrepancy between the $M = 0$ calculations and the experimental data is larger compared to the other two liquid viscosities. Using a lower values of $\theta_{mic,B}$ in the $M = 0$ calculations raises the Ca^{crit} values, but does not bring them into agreement with the experimental data. Thus, for these solutions, surfactant-related phenomena (e.g., substrate adsorption) other than changes to the mean surface tension and static contact angle may be playing a more important role. Indeed, as the solutions become less viscous, Marangoni stresses would be expected to become more influential (e.g., the values of M are generally larger for the 50 cP solutions compared to the 400 cP solutions [appendix B]). However, as noted in Section 3.4.2, experimental limitations have prevented us from studying solutions with viscosities lower than 50 cP.

For all of the cases shown in Figure 3.12, the model predictions for $M \neq 0$ are lower than the experimental values. Since Marangoni stresses tend to lower the value of Ca^{crit} (Section 3.3), this suggests that the model may overestimate the importance of Marangoni stresses, possibly due to the use of a linear equation of state and linear rate laws for surfactant adsorption [130, 69]. It is also possible that the slip length may vary with surfactant concentration, or the assumption of a Navier-slip law with constant microscopic contact angle may break down in the presence of surfactants [56, 55, 131, 132, 133]. Finally, we note that if the parameters controlling surfactant adsorption to the substrate, K_{DCL} and K_b, are made non-zero ($K_{DCL} \approx O(1)$, $K_b \approx O(0.1)$), it is possible to obtain agreement between the model predictions and experimental data. However, experimental values of these parameters are unknown, preventing us from drawing definitive conclusions about the role of surfactant adsorption. Resolution of these issues will require methods of imaging surfactant concentration distributions along the fluid interface and substrate and in the bulk, and improved characterization of surfactant adsorption kinetics [134, 135].

Overall, the results from this section indicate that for the more viscous solutions, the increase in Ca^{crit} with surfactant concentration can largely be explained by accounting for changes to the mean surface tension and static contact angle (This is also consistent with our observation in Appendix 3.7.2 that the air-film characteristics are not significantly affected by surfactant concentration.) For the solution with the lowest viscosity, other surfactant-induced phenomena (as described above) may become important, but more comprehensive experiments are needed to elucidate the underlying physical mechanisms.

3.6 Conclusions

In this work we have used a hydrodynamic model and complementary experiments to gain insight into the physical mechanisms through which surfactants influence the onset of dynamic wetting failure. Our parametric study in Section 3.3 demonstrates how surfactant solubility weakens the influence of Marangoni stresses, and elucidates the influence of various parameters controlling surfactant adsorption to the fluid interface and substrate. Comparison of the model predictions to our experimental observations (Section 3.5) reveals that for the more viscous solutions we used, changes to the mean surface tension and static contact angle appear to be largely responsible for the increase in Ca^{crit} with surfactant concentration. For the solution with the lowest viscosity, other surfactant-induced phenomena may become important, but more comprehensive experiments are needed to definitively establish this.

Our results point to the need for imaging of surfactant concentration distributions and better characterization of surfactant adsorption kinetics. There is especially a need for measuring adsorption to substrates, since our results in Section 3.3 raise the possibility that substrate adsorption could be used to delay the onset of wetting failure. Such studies are not only of fundamental interest, but also important for understanding the influence of surfactants in industrially important flows such as curtain coating [116, 78].

3.7 Appendix

3.7.1 Stress gradient

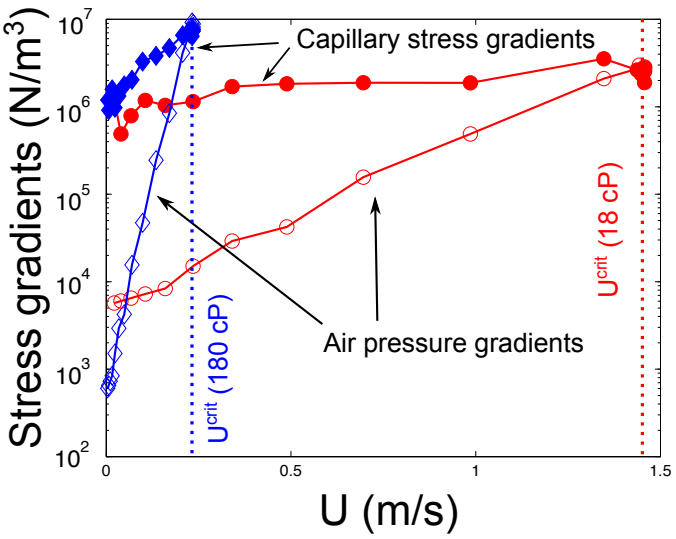

Figure 3.13: Stress gradients at the inflection point of the fluid interface for $\mu_{liq} = 180$ cP (blue diamonds) and $\mu_{liq} = 18$ cP (red circles). The capillary-stress gradients (filled symbols) match the receding-phase pressure gradients (open symbols) at U^{crit} values denoted by vertical dotted lines. Other parameter values are $\lambda = 10^{-4}$, $M = 0$, and $\theta_{mic,T} = \theta_{mic,B} = 90^o$.

Several experimental studies have shown the critical capillary number Ca^{crit} to increase weakly with higher liquid viscosities, showing a power-law relationship, $Ca^{crit} = \mu^a$, where $0 < a < 1$ [2, 26]. This implies that $U^{crit} = \mu^b$, where $b < 0$ and U^{crit} decreases for higher liquid viscosities. Figure 3.13 shows the magnitudes of the capillary-stress gradient and air-pressure gradient as a function of the substrate speed U for two liquid viscosities. These gradients match at the critical speed U^{crit} in both liquids. Both the capillary-stress gradients and the air-pressure gradients are larger in the more viscous liquid than those in the less viscous one due to the more pronounced interface bending. However, the air-pressure gradients increase more rapidly than the capillary-stress gradients as the liquid viscosity increases, so wetting failure occurs at a lower critical speed.

3.7.2 Air-film characteristics

In this work, the critical speed U^{crit} corresponding to dynamic wetting failure is determined by gradually increasing the tape speed until triangular air films form at the dynamic contact line (DCL). The films are sensitive to disturbances and can quickly rupture, leaving behind air bubbles that are entrained in the bulk liquid. In this section, we characterize the films in the presence of surfactants.

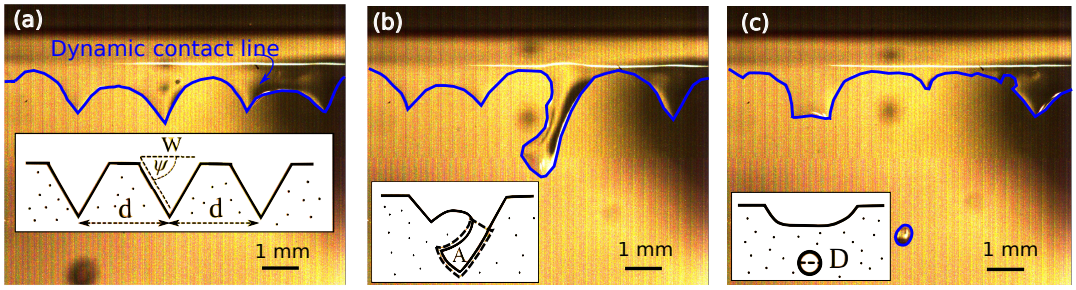

Figure 3.14: Evolution of the air film at the onset of air entrainment: (a) triangular air films with width W, angle ψ, and spacing d, (b) local rupture of air film with area A, and (c) formation of a spherical air bubble with diameter D. The schematic in each panel represents an idealization of each state. The blue solid line denotes the dynamic contact line. The liquid viscosity $\mu_{liq} = 400$ cP, and the critical speed $U^{crit} = 0.082$ m/s. The time lapse between panels is ≈ 30 ms.

Figure 3.14 shows three characteristic stages near the dynamic contact line (DCL) at the onset of air entrainment. First, sawtooth-shaped triangular air films appear at the DCL. Each air "vee" can be represented by an isosceles triangle of angle ψ with a width W. The distance between the apexes of adjacent triangles is denoted by d. Second, disturbances cause the elongated air film to locally rewet the substrate. The rewetted region grows, resulting in an irregular film of area A connecting with the meniscus (Figure 3.14(b)). Finally, a portion of the air film breaks off and forms a spherical bubble with diameter D due to surface-tension forces (Figure 3.14(c)). The following sections discuss the influence of surfactants on the shape (Section 3.7.2), thickness, and spacing (Section 3.7.2) of the air film.

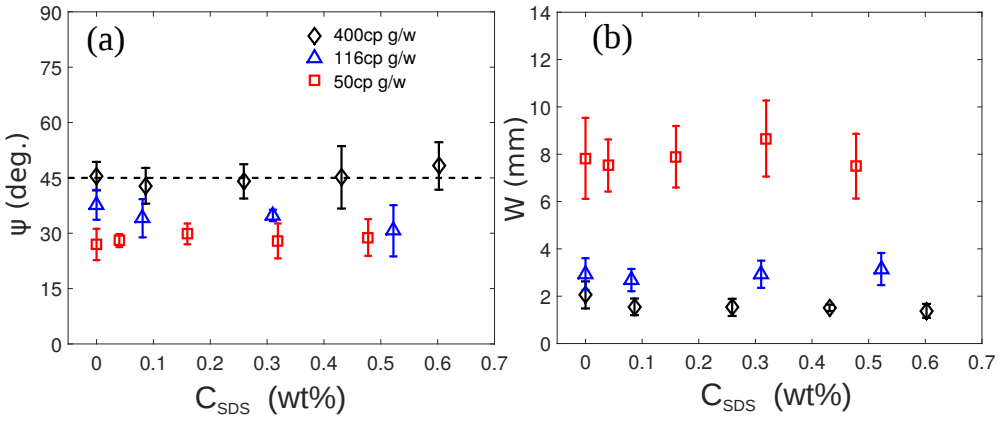

Figure 3.15: The effect of SDS concentration C_{SDS} on triangular air-film formed at Ca^{crit} as characterized by (a) angle ψ and (b) width W (refer to Figure 3.14 for the definition of ψ and W). In each panel, symbols correspond to solutions with different viscosities: $\mu_{liq} = 400$ cP (black diamonds), $\mu_{liq} = 116$ cP (blue triangles), and $\mu_{liq} = 50$ cP (red squares). Dashed line in (a) represents 45^o.

Shape

Figure 3.15 demonstrates the influence of surfactants on the characteristic angle ψ and width W of the triangular air films. Interestingly, the addition of surfactants does not significantly change the values of ψ and W. However, ψ and W depend on the liquid viscosity. The angle ψ has a larger value at a higher liquid viscosity, whereas the width W has a larger value at a lower liquid viscosity. These findings are consistent with prior work in the absence of surfactants [26]. At lower viscosity, the decrease in the angle ψ can be attributed to an edge effect caused by the tape since the air film is wider.

Thickness and spacing

Air-film thickness can be estimated from visualizations of the evolution of the air films, as illustrated in Figure 3.14. At the early stage of the rupture process (Figure 3.14(b)), the meniscus is connected with an irregular air film with volume $A \times h_{exp}$, where h_{exp} represents the height of the air film defined by area A. Since the diameter D of a spherical air bubble can be easily measured (Figure 3.14(c)), the film thickness h_{exp} can be approximated as $h_{exp} = \pi D^3/6A$.

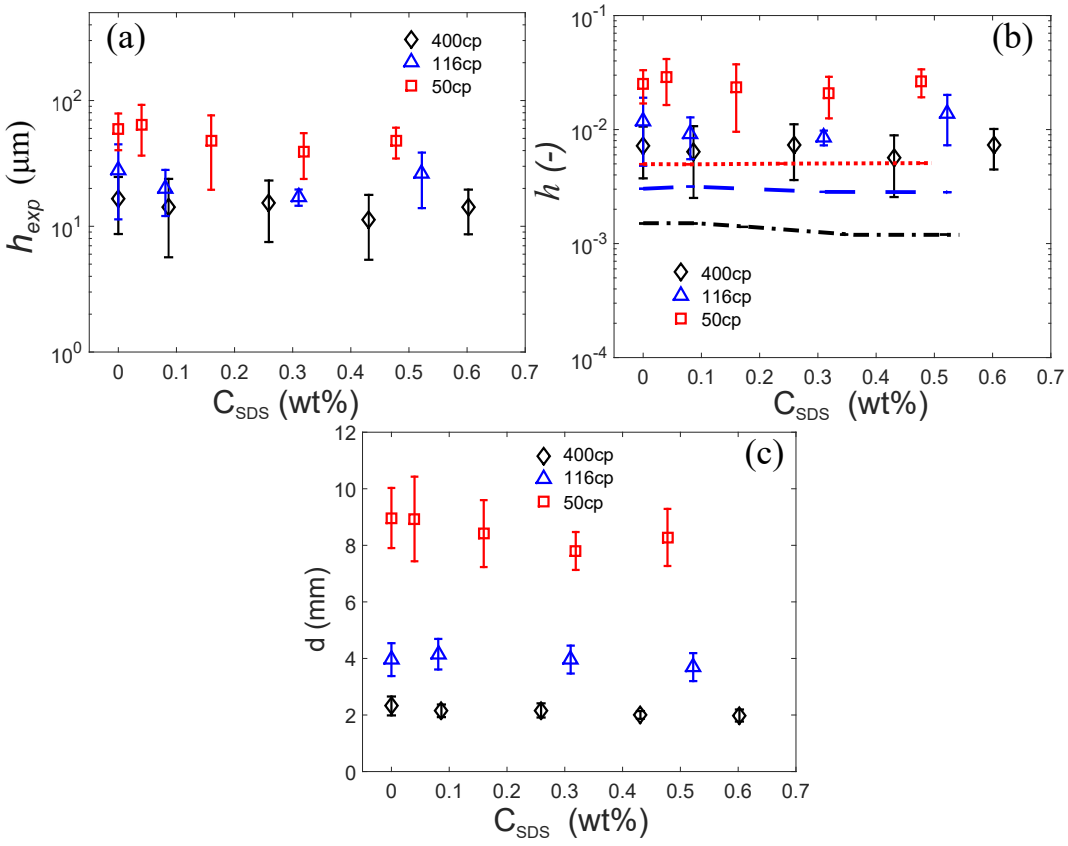

Figure 3.16: (a) Estimated air-film thickness h_{exp}, (b) comparison of the dimensionless film thickness from the experiments h and the height of the inflection point h_f from our model, and (c) spacing d of triangular air films at different liquid viscosities: $\mu_{liq} = 400$ cP (black diamonds), $\mu_{liq} = 116$ cP (blue triangles), and $\mu_{liq} = 50$ cP (red squares). In (b), the dotted line (50 cP), dashed line (116 cP), and dashed dotted line (400 cP) represent model predictions of h_f when $M = 0$. Note that y axis in (b) is dimensionless.

Figure 3.16(a) shows the estimated film thickness h_{exp} at different surfactant concentrations. We found that the variation of h_{exp} values is small through the range of C_{SDS} investigated. However, the liquid viscosity has a larger effect on h_{exp} values with a higher viscosity corresponding to a smaller h_{exp} value, consistent with the experimental observations in prior work [26]. The change in the h_{exp} values is a consequence of the interaction between capillary and viscous stresses. As the liquid viscosity increases, the interface can bend more near the DCL, generating larger capillary stress gradients that lead to a thinner air film [26].

Figure 3.16(b) shows the comparison between the dimensionless film thickness $h = h_{exp}/l_{cap}$ from the experiments and the height of the inflection point h_f from our model when $M = 0$. Note that h_{exp} is non-dimensionalized by the capillary length l_{cap}. As can be seen, the variation of h_f values is small through the range of C_{SDS}, showing a similar trend to that of the dimensionless film thickness h. We note that since h_f does not necessary equal the value of h estimated from the experiments, the values of h_f may be different from those of h.

As expected, the addition of surfactants does not significantly change the values of the spacing d (Figure 3.16(c)). The value of d is mainly influenced by the liquid viscosity, consistent with prior work in the absence of surfactants [26].

3.7.3 Model parameters in Figure 3.12

Model parameters in each panel:

(a) $\chi = 4.48 \times 10^{-5}$, $\lambda = 9.07 \times 10^{-6}$, $Pe_s = 10^4$, $Pe_b = 10^5$, $K_{DCL} = K_b = 0$ for each model result. For $M = 0$ (red circles), concentration = [0.086, 0.173, 0.345, 0.517] wt%, $\alpha = [7.64, 7.83, 8.58, 8.95] \times 10^4$, $K = [3.65, 3.74, 4.10, 4.28] \times 10^1$, and $\theta_{mic,B} = [71^o, 68^o, 64^o, 61^o]$; For $M = [0.22, 0.35, 0.47]$ (blue squares), concentration = [0.086, 0.173, 0.259] wt%, $\alpha = [7.64, 7.83, 8.24] \times 10^4$, $K = [3.65, 3.74, 3.94] \times 10^1$, and $\theta_{mic,B} = [71^o, 68^o, 66^o]$.

(b) $\chi = 1.55 \times 10^{-4}$, $\lambda = 3.25 \times 10^{-6}$, $Pe_s = 10^4$, $Pe_b = 10^5$, $K_{DCL} = K_b = 0$ for each model result. For $M = 0$ (red circles), concentration = [0.081, 0.176, 0.310, 0.458, 0.607] wt%, $\alpha = [3.05, 3.16, 3.41, 3.69, 3.97] \times 10^4$, $K = [1.46, 1.51, 1.63, 1.76, 1.9] \times 10^1$, and $\theta_{mic,B} = [68^o, 66^o, 63^o, 59^o, 56^o]$; For $M = [0.36, 0.51, 1, 1.3]$ (blue squares), concentration = [0.081, 0.176, 0.458, 0.607] wt%, $\alpha = [3.05, 3.16, 3.69, 3.97] \times 10^4$, $K =$

$[1.46, 1.51, 1.76, 1.90] \times 10^1$, and $\theta_{mic,B} = [68^o, 66^o, 59^o, 56^o]$.

(c) $\chi = 3.58 \times 10^{-4}$, $\lambda = 2 \times 10^{-6}$, $Pe_s = 10^4$, $Pe_b = 10^5$, $K_{DCL} = K_b = 0$ for each model result. For $M = 0$ (red circles), concentration = [0.040, 0.080, 0.239, 0.319] wt%, $\alpha = [1.48, 1.50, 1.66, 1.73] \times 10^4$, K =[7.09, 7.18, 7.94, 8.29], and $\theta_{mic,B} = [67^o, 62^o, 58^o, 54^o]$; For $M = [0.38, 1, 1.2]$ (blue squares), concentration =[0.040, 0.239, 0.319] wt%, $\alpha = [1.48, 1.66, 1.73] \times 10^4$, $K = [7.09, 7.94, 8.29]$, and $\theta_{mic,B} = [67^o, 58^o, 54^o]$.

For all of the model predictions, $k_a = 3 \times 10^4$ m^3/mol s, $k_d = 2.73 \times 10^6$ s^{-1}, $D_b = 10^{-9}$ m^2/s, and $D_s = 10^{-8}$ m^2/s [124, 69].

Chapter 4

Dynamic Wetting Failure and Hydrodynamic Assist in Curtain Coating

4.1 Introduction

Dynamic wetting is a common phenomenon in everyday life and industrial coating operations where an ambient fluid (often air) is displaced by a liquid on a solid surface. In particular, coating flows rely heavily on steady dynamic wetting to uniformly deposit a liquid on a moving substrate [82]. Dynamic wetting fails at some critical substrate speed and is accompanied by a change in flow from steady two-dimensional (2D) to unsteady three-dimensional (3D) [6, 7, 26]. In coating processes, wetting failure leads to air entrainment and can degrade product quality [82, 2]. Therefore, understanding the mechanisms of wetting failure is very important so that strategies to delay the onset of wetting failure and increase coating speed can be developed. [1]

Curtain coating is a high-speed coating method where substrate speeds of $U \approx 10$ m/s can be achieved [11, 12, 136, 137]. In this method, liquid is extruded (at a feed flow velocity V) from a die (of width w) at a height h_{curt} onto a moving substrate (Figure 4.1(a)). Gravity accelerates the liquid as it flows down the curtain [14, 13]. A uniform

[1] This chapter was originally published in [116].

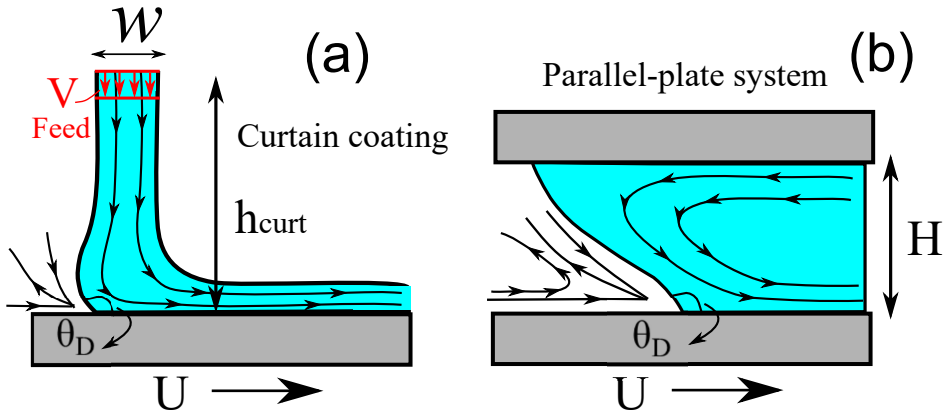

Figure 4.1: Schematics of (a) curtain coating and (b) parallel-plate geometry.

film of thickness h_{inf} is formed on the substrate when the liquid flow is steady and two-dimensional. The ability to achieve high substrate speeds has made curtain coating a popular mass-production method [10]. However, the mechanism of wetting failure in curtain coating remains poorly understood.

4.1.1 Hydrodynamic assist

The term "hydrodynamic assist" is used to describe the fact that curtain coating can be manipulated to assist dynamic wetting and delay the onset of wetting failure (i.e., air entrainment) [14, 10]. It was found that manipulating the feed flow velocity V in curtain coating can postpone the onset of wetting failure to a higher critical substrate speed U^{crit} in comparison with "plunge coating", where a solid substrate plunges into a liquid pool [138, 139]. Experimental observations show that the degree of hydrodynamic assist reaches its maximum (i.e., the largest critical speed) when the dynamic contact line (DCL) is right beneath the liquid curtain, which leads to a strong hydrodynamic pressure near the DCL as the liquid impacts the substrate [14, 138, 137, 140, 10, 139].

Flow visualizations near the DCL show that manipulating V (at a given substrate speed U) can also lead to a reduction in the dynamic contact angle θ_D, the observed angle between the fluid interface and the substrate at the DCL (Figure 4.1(a)) [138, 141, 137, 142]. To study the origin of the reduction in θ_D, Wilson et al. [15, 143] developed a hydrodynamic model for curtain coating with a fixed microscopic contact angle θ_{mic}

prescribed at the DCL. Note that θ_{mic} serves as a boundary condition at the DCL and influences the free-surface shape [22, 39].

Their model prediction [15, 143] shows that the reduction in the apparent contact angle (i.e., interface angle calculated 20 μm away from the DCL in their model and assumed to be equal to θ_D) is much smaller than than the reduction in θ_D observed experimentally by Blake et al. [138]. Therefore, Wilson et al. [15, 143] claimed that θ_{mic} is not a constant and must depend on parameters controlling the overall flow (e.g., curtain height h_{curt} and feed flow rate $Q = wV$). However, their hydrodynamic model does not consider the contribution of air stresses, and as a consequence, cannot predict a critical speed for wetting failure. As we will discuss below, air stresses are essential for determining the shape of the fluid interface and predicting wetting failure [31, 26, 93].

Before proceeding, we note that there are several different ways to describe dynamic wetting phenomena [22, 39, 98, 117]. The first (and simplest) is to assume that θ_{mic} is constant, and that all variations in θ_D are due bending of the fluid interface by viscous forces. The second is to assume that θ_{mic} depends on substrate speed through a relationship like that obtained from the molecular-kinetic theory of wetting. The third is to assume that θ_{mic} depends on parameters controlling the overall flow, which is the approach of the interface-formation model. Wilson et al. [15, 143] used the first approach and concluded that it cannot adequately describe the experimental observations. The conclusion of the present chapter is that the first approach may be sufficient provided that air stresses are accounted for.

4.1.2 The role of air stresses

A common approach in previous computational studies of coating flows is to neglect the contribution of air stresses due to the low air viscosity [15, 143, 144, 145, 146]. However, in our previous work on fluid displacement between two parallel plates (Figure 4.1(b)), we have shown the need to incorporate the air phase to accurately describe the displacement process and predict wetting failure [23, 31, 26, 32].

If air stresses are neglected in the model, 2D steady-state solutions can be obtained at any substrate speed, meaning that the onset of wetting failure (i.e., the critical substrate speed U^{crit}) is completely missed [31]. By including the air-phase contribution to stress balances along the fluid interface, a limit point arises in the steady-state solution path

(θ_D vs. U), indicating that 2D steady solutions do not exist beyond a critical substrate speed. This critical speed marks the onset of wetting failure [31]. A stress-gradient analysis revealed that wetting failure occurs when capillary-stress gradients generated by interfacial curvature can no longer provide the pressure gradients needed to pump air away from the DCL, a mechanism supported by experimental studies [31, 26].

Notably, the geometry of curtain coating is significantly different from that of the parallel-plate system (Figure 4.1). In the former geometry, liquid is fed from a coating die and creates two free surfaces (i.e., upstream and downstream fluid interfaces) as the liquid impacts the substrate. In the latter geometry, there is no feed flow and only one free surface between two plates. However, even though these two geometries are very different, they both feature a thin air layer (wedge) near the DCL during fluid displacement, especially near the onset of wetting failure. Therefore, our previous work on the parallel-plate system [31, 26] suggests that it will be important to consider the contribution of air stresses when modeling curtain coating.

4.1.3 Influence of surfactants

Surfactants are known to lower the surface tension σ, and can also lower the static contact angle θ_s according to Young's equation [65]. In addition, gradients in surfactant concentration can induce surface-tension gradients (i.e., Marangoni stresses), driving liquid from regions of low to high surface tension [3]. Experimental results reported by Marston et al. [78] show that the addition of surfactant (sodium dodecyl sulphate) to glycerol/water mixtures significantly decreases the critical substrate speed U^{crit} (up to 66.7%) in curtain coating. In addition, the shape of the coating window (i.e., the parameter space within which the coating flow is steady and free of defects) is considerably modified, with the degree of hydrodynamic assist being greatly reduced by surfactants.

Marston et al. reported that after the addition of surfactant, a twofold reduction in surface tension is observed but the liquid viscosity remains approximately the same [78]. Since no non-Newtonian rheological behavior is observed in the surfactant solutions, the change in the critical speed and the shape of the coating window suggests that surface-tension gradients (i.e., Marangoni stresses) may also play an important role. Our previous work with the parallel-plate system (Figure 4.1(b)) demonstrates

that the presence of Marangoni stresses promotes the onset of wetting failure (i.e., decreases U^{crit}) by thinning the air film between the fluid interface and the substrate [83]. However, since the geometries of the parallel-plate system and curtain coating are significantly different, it is not obvious that the physical mechanisms relevant to the parallel-plate system still hold in curtain coating.

4.1.4 Overview of present chapter

In this chapter, a hydrodynamic model for curtain coating accounting for the receding air flow is developed. Since a full 2D description of both the liquid and air phases is computationally prohibitive, here we use a less computationally intense approach that combines a 2D description of the liquid and a one-dimensional (1D) description of the air near the DCL. The 1D description is motivated by the observation of a long and slender air film as the interface deforms near the onset of wetting failure [2, 26, 104]. This hybrid approach was used in our previous work [83] on the parallel-plate system (Figure 4.1(b)) and its predictions were shown to be in excellent agreement with those from calculations using full 2D descriptions of both the air and liquid phases. Here, the hybrid approach is applied to a considerably more complicated geometry (Figure 4.1(a)).

We solve this hybrid formulation of the hydrodynamic model with the Galerkin finite element method. By tracing steady-state solutions of the model as substrate speed increases, we can locate a critical substrate speed U^{crit} beyond which 2D steady solutions do not exist. This critical condition corresponds to the onset of wetting failure and is characterized by a critical capillary number $Ca^{crit} = \mu_{adv} U^{crit}/\sigma$, where μ_{adv} is the viscosity of the advancing liquid and σ is the surface tension. Prior literature shows that the value of Ca^{crit} depends on various factors such as fluid properties [147, 104, 111], substrate properties [24, 31], and flow geometry [26, 23, 138, 141].

The objective of the present chapter is to determine how Ca^{crit} in curtain coating changes with the viscosity of the receding air μ_{rec} (i.e., the strength of air stresses), feed flow rate Q (i.e., V), and Marangoni stresses induced by surface-tension gradients. To examine how well the hydrodynamic model performs, we also compare our predictions of contact-angle behavior with prior computational work by Wilson et al. [15, 143] and experimental work by Blake et al. [138]. In addition, physical explanations of

hydrodynamic assist and Marangoni effects on wetting failure are proposed using a stress-gradient analysis [31, 83].

The mathematical formulation and solution method we use are described in Section 4.2. In Section 4.3, we discuss the influence of the receding phase and compare Ca^{crit} in curtain coating and the parallel-plate system. Hydrodynamic assist in curtain coating and its physical mechanism are examined in Section 4.4. The variation of contact angle with feed flow rate is the topic of Section 4.5. Section 4.6 presents results on the influence of surfactants on wetting failure and the underlying physical mechanisms. Finally, a summary of our results is provided in Section 4.7.

4.2 Hydrodynamic model

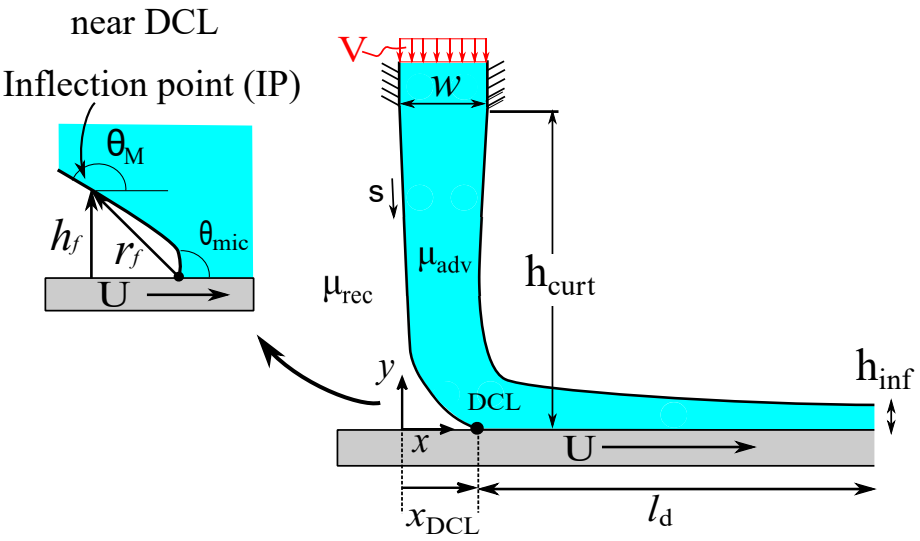

Figure 4.2: Schematic of physical coating domain and illustration of interface characteristics near the dynamic contact line (DCL). The inflection point corresponds to the maximum interface angle, and its height and radial distance are characterized by h_f and r_f, respectively.

In curtain coating, liquid is fed from an elevated slot die (width w and height h_{curt}) with an average downward feed flow velocity V onto a substrate moving at speed U (Figure 4.2). The liquid impacts the substrate at the dynamic contact line (DCL), whose position x_{DCL} depends on the problem parameters. The viscosities of the advancing

(liquid) and the receding (air) fluids are denoted by μ_{adv} and μ_{rec}, respectively. The liquid density and surface tension are denoted by ρ and σ. Symbols x and y represent the Cartesian coordinates, whose origin is right beneath the upstream tip of the slot die as indicated in Figure 4.2. During steady wetting, a coating film with a uniform thickness $h_{inf} = Q/U$ is formed over the moving substrate, where $Q = wV$ is the liquid flow rate per unit width from the slot die. Note that the domain length l_d extends to approximately $5h_{curt}$ downstream to obtain a well-developed flow in the coating film.

The schematic of the region near the DCL (Figure 4.2) shows the difference between the microscopic contact angle θ_{mic} and the macroscopic contact angle θ_M. The former angle (θ_{mic}) is located at the place where the interface contacts the substrate and serves as a boundary condition in our model. In contrast, the latter one (θ_M) is defined to be the maximum angle along the fluid interface and corresponds to the inflection point (IP) of the fluid interface. Note that θ_M does not necessarily equal the dynamic contact angle θ_D, the experimentally observed angle between the fluid interface and the substrate. The height of the IP and the radial distance from the DCL are denoted by h_f and r_f, respectively.

Since we are interested in the influence of Marangoni stresses on wetting failure, we will also consider the case where insoluble surfactants are present on the upstream fluid interface. We neglect the effect of surfactants on the downstream fluid interface because wetting failure occurs at the DCL.

4.2.1 Governing equations

The steady Navier-Stokes equations describe the velocity $\boldsymbol{v}$ and pressure p in the liquid phase:

$$\boldsymbol{\nabla} \cdot \boldsymbol{v} = 0,\ Re(\boldsymbol{v} \cdot \boldsymbol{\nabla}\boldsymbol{v}) = \nabla^2 \boldsymbol{v} - \boldsymbol{\nabla} p + (Bo/Ca)\boldsymbol{g}. \tag{4.1}$$

The lengths, velocities, and stresses are non-dimensionalized with the characteristic scales Q/U, U, and $\mu_{adv}U^2/Q$, respectively. The Reynolds, capillary, and Bond numbers are given by $Re = \rho V w/\mu_{adv}$, $Ca = \mu_{adv}U/\sigma$, and $Bo = (\rho g/\sigma)(wV/U)^2$, respectively. The gravitational acceleration is given by $\boldsymbol{g} = -g\mathbf{e}_y$, where $\mathbf{e}_y$ is the unit vector in the y-direction.

Near the DCL, the air phase is long and slender. Lubrication theory is thus applied to the air phase, resulting in a 1D description of the air flow (as described in our previous

work [32, 83]):

$$Ah + \frac{1}{2}Bh^2 + \frac{1}{6}\frac{dp}{ds}h^3 = 0, \tag{4.2}$$

$$\frac{\partial u}{\partial y}|_s = B + \frac{dp}{ds}h \quad \text{where} \quad A = \frac{\chi h + \chi\lambda u_s - \frac{1}{2}\frac{dp}{ds}h^2\lambda}{\lambda + h}\ ,\ B = \frac{-\chi + A}{\lambda}, \tag{4.3}$$

where h is the interface height, p is the air pressure, u_s represents the horizontal interface velocity, $\lambda = l_{slip}U/Q = l_{slip}/h_{inf}$ is a dimensionless slip length with l_{slip} being the dimensional slip length, and $\chi = \mu_{rec}/\mu_{adv}$ is the viscosity ratio. The velocity gradient in (4.3) is evaluated at the interface. Note that the quasi-parallel (QP) approximation ($dx \approx ds$) is used in (4.2)-(4.3) to express pressure gradients with respect to the arclength coordinate s along the interface (Figure 4.2) [96, 97].

The following set of dimensionless boundary conditions is applied along the upstream fluid interface:

$$\boldsymbol{v}\ |_{rec} = \boldsymbol{v}\ |_{adv}, \tag{4.4}$$

$$\boldsymbol{n} \cdot \boldsymbol{v} = 0, \tag{4.5}$$

$$M\boldsymbol{\nabla_s}\sigma \cdot \boldsymbol{t} = \boldsymbol{n} \cdot \boldsymbol{T} \cdot \boldsymbol{t}\ |_{adv} - \boldsymbol{n} \cdot \boldsymbol{T} \cdot \boldsymbol{t}\ |_{rec}, \tag{4.6}$$

$$\kappa(1/Ca + \sigma M) = \boldsymbol{n} \cdot \boldsymbol{T} \cdot \boldsymbol{n}\ |_{adv} - \boldsymbol{n} \cdot \boldsymbol{T} \cdot \boldsymbol{n}\ |_{rec}\ . \tag{4.7}$$

Equations (4.4)-(4.5) represent the no-slip and no-penetration boundary conditions, and (4.6)-(4.7) are interfacial stress balances. At the fluid interface, $\boldsymbol{n}$ is the unit outward vector normal to the interface and unit tangent vector $\boldsymbol{t}$ points in the direction of increasing distance s along the interface (Figure 4.2). Subscripts "adv" and "rec" indicate properties in the advancing and receding phases, respectively.

In the stress balances, $\boldsymbol{\nabla_s}\sigma$ denotes the surface-tension gradient along the interface, κ represents the interface curvature, and $\boldsymbol{T}$ is the Newtonian stress tensor. The Marangoni and capillary numbers are defined as $M = (\sigma_o - \sigma_m)/\mu_{adv}U$ and $Ca = \mu_{adv}U/\sigma_m$. Here, σ_o is the surface tension of the surfactant-free solution and σ_m is the surface tension corresponding to the mean surfactant concentration Γ_m at the interface. In the absence of surfactant, $\sigma_o = \sigma_m$ and the Marangoni stresses vanish (i.e., $M = 0$).

At the downstream fluid interface, the no-slip and kinematic boundary conditions (4.4)-(4.5) are still valid. However, since the air flow near the downstream interface

is not expected to have significant effects on wetting failure, the stress contribution from the air phase there is neglected. The stress balances at the downstream interface become:

$$\boldsymbol{n} \cdot \boldsymbol{T} \cdot \boldsymbol{t} \mid_{adv} = 0, \tag{4.8}$$

$$\kappa = Ca \left(\boldsymbol{n} \cdot \boldsymbol{T} \cdot \boldsymbol{n} \mid_{adv} + P_{amb} \right), \tag{4.9}$$

where P_{amb} is the ambient pressure. As noted earlier, we neglect the effect of surfactants on the downstream fluid interface. Therefore, surface tension there remains constant, resulting in (4.8)-(4.9).

To remove the stress singularity that would arise by applying the no-slip boundary condition at the DCL, a Navier-slip boundary condition is applied along the moving substrate [46, 92, 93, 94]:

$$\boldsymbol{t_s} \cdot (\boldsymbol{v} - \boldsymbol{U}) = \lambda \, [\boldsymbol{n_s} \cdot \boldsymbol{T} \cdot \boldsymbol{t_s}], \tag{4.10}$$

where λ is the dimensionless slip length defined earlier. Symbols $\boldsymbol{n_s}$, $\boldsymbol{t_s}$, and $\boldsymbol{U}$ correspond to the substrate's normal, tangent, and velocity vectors, respectively. This slip boundary condition is applied along the entire bottom substrate and is able to recover the no-slip condition ($\boldsymbol{v} \rightarrow \boldsymbol{U}$) for distances greater than l_{slip} away from the DCL. Although the slip length will in general have different values in the advancing and receding phases, for simplicity we assume here that it has the same value in both phases. This assumption has worked well in our previous work on the parallel-plate system [23, 31, 26]. Note that in the vertical direction, the no-penetration condition is applied to the bottom boundary.

In the hydrodynamic model, the microscopic contact angle θ_{mic} serves as a boundary condition at the DCL to determine the free-surface shape [22, 39]. In general, θ_{mic} may depend on problem parameters such as the substrate speed, curtain height, and feed flow rate [44, 117, 2, 98] (see §1.1). Since we wish to isolate the influence of air stresses, we take the simplest view and assume θ_{mic} to be equal to the static contact angle θ_s (a fixed value) [31, 98, 40, 45].

4.2.2 Surfactant transport

A steady convection-diffusion equation describes insoluble surfactant transport along the upstream fluid interface:

$$\boldsymbol{\nabla_s} \cdot (\boldsymbol{v_s}\Gamma) = \frac{1}{Pe}\nabla_s{}^2\,\Gamma, \tag{4.11}$$

where $\boldsymbol{\nabla_s}$ is the surface gradient operator and $\boldsymbol{v_s}$ is the interface velocity. The surface Peclet number $Pe = Vw/D_s$ is defined using the surface diffusion coefficient D_s. The dimensionless surfactant concentration Γ is scaled with $K\Gamma_m$, where K represents a scaling factor ($K \gg 1$) and Γ_m is the mean surfactant concentration at the fluid interface. Because the flow along the interface carries surfactant toward the DCL, large concentration gradients arise there that are computationally prohibitive to resolve if we scale Γ with Γ_m only (i.e., $K = 1$). As a result, we introduce a scaling factor K and choose $K = 500$.

The surfactant transport equation (4.11) is coupled with the tangential stress balance (4.6) through an equation of state [79]. For simplicity, we assume that the surfactant concentration is dilute enough to apply a linear equation of state [90, 122, 123, 89]:

$$\sigma = 1 - \Gamma. \tag{4.12}$$

Here, surface tension σ has been non-dimensionalized using the relation $\sigma' = \sigma_m + (\sigma_o - \sigma_m)\sigma$, where σ' represents the dimensional surface tension [91].

We assume that surfactants do not deposit onto the solid surfaces. As a result, no-flux boundary conditions $\boldsymbol{n} \cdot \nabla\Gamma = 0$ are applied at the DCL and also the upstream tip of the slot die (Figure 4.2). These boundary conditions require that a constraint of constant surfactant mass be applied:

$$\int_S \Gamma \; ds = (1/K)S, \tag{4.13}$$

where S represents the total arclength of upstream fluid interface. Note that $1/K$ in (4.13) results from scaling concentration by $K\Gamma_m$.

Surfactants can potentially influence the microscopic contact angle θ_{mic} and induce surface-tension gradients at the same time. To isolate the influence of Marangoni stresses on wetting failure, we assume that θ_{mic} is neutral at the DCL (i.e., $\theta_{mic} = 90^o$) and remains unchanged by surfactants. In addition, when comparing curtain coating in the absence and presence of surfactants, the mean surface tensions σ_m are kept the same.

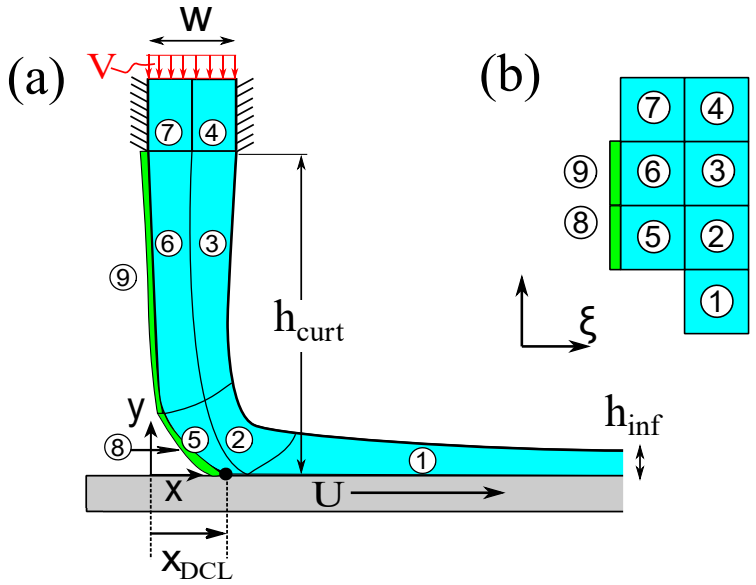

Figure 4.3: Schematic of (a) physical coating domain and (b) computational domain composed of seven liquid regions (1)-(7), air region (8), and surfactant-transport regions (8) and (9).

4.2.3 Solution method

The Navier-Stokes equations (4.1), 1D description of the receding air flow (4.2), surfactant transport equation (4.11), and associated boundary and integral conditions (i.e., (4.4)-(4.10),(4.12)-(4.13)) are solved with the Galerkin finite element method. The liquid domain is partitioned into seven quadrangular regions and the air flow is only discretized in the 1D region (8) near the DCL (Figure 4.3(a)). Regions (8) and (9) represent the 1D domain on which surfactant transport along the upstream fluid interface is solved.

To solve the free-boundary problem, the physical domain (Figure 4.3(a)) is mapped to a computational domain whose coordinates are η and ξ (Figure 4.3(b)). The mapping function satisfies the elliptic mesh generation equations [148, 145]. Biquadratic basis functions are used for position and velocity variables, and linear discontinuous basis functions are used for pressure in the liquid phase. The air pressure and the surfactant concentration are also described by biquadratic basis functions.

We found that mesh quality is best when the contact-line position x_{DCL} (Figure 4.3(a)) is located directly underneath the upstream tip of the slot die ($x_{DCL} = 0$). When

the DCL moves downstream ($x_{DCL} > 0$), elements near the DCL are stretched as the curtain is pulled (Appendix 4.8.1). In contrast, when $x_{DCL} < 0$ elements are stretched both near the DCL and near the upstream interface, where the curtain contacts a liquid heel that forms (Appendix 4.8.1). These mesh distortions make it very difficult to obtain discretization-independent steady-state solutions as the substrate speed U increases (at a fixed feed flow velocity V). To mitigate this numerical issue, we fix x_{DCL} (as a flow parameter) and calculate V (as a dependent variable) as we trace solution paths to higher substrate speeds U (using first-order continuation). As expected, V must increase as U increases to hold the DCL position fixed (Appendix 4.8.2).

Since the interface bends sharply near the DCL (Figure 4.3(a)), a larger number of elements near the DCL is required to resolve large gradients in the interface curvature. These gradients become larger as Ca increases. As a consequence, we found that element sizes near the DCL need to be less than $10^{-3} l_{slip}$ to obtain mesh-independent solutions. Convergence is tested by systematically varying the number of elements to verify that solutions are mesh independent (i.e., less than 2% variation in Ca^{crit} predicted from solution paths in Sec. 4.3).

4.2.4 Model parameters

Because we are most interested in how flow behavior changes as the substrate speed increases for fixed fluid properties, it is convenient to choose a representative set of dimensional parameters. Motivated by experimental data, we take $\mu_{adv} = 25$ cP, $\mu_{rec} = 0.018$ cP, $\sigma = 70$ mN/m, and $\rho = 1000$ kg/m^3. In addition, since we would like to isolate the effects of substrate speed and feed flow rate, we assume a neutral microscopic contact angle of $\theta_{mic} = 90°$. We note that even for this value of θ_{mic}, predictions of the hybrid model for the parallel-plate geometry are in excellent agreement with results from a model that uses a full 2D description of both the air and liquid phases [83]. For this reason, we expect that a 1D description of the air flow is sufficient for accurately describing the behavior of curtain coating.

To avoid prohibitive computational costs that come with having too large a flow domain, we fix the curtain height at $h_{curt} = 1$ cm. Although this is smaller than typical curtain heights ($\sim$ 2 to 25 cm), we expect that the results reported here will show the same qualitative behavior as results for larger curtain heights.

Since smaller values of the slip length mean more elements near the DCL and a higher computational cost, a relatively large slip length $l_{slip} = 10^{-5}$ m is selected for numerical convenience. Other runs we have performed (not shown here) and our previous work with the parallel-plate geometry [83] indicate that an increase in the slip length only increases the Ca^{crit} values without changing the qualitative nature of the solutions. We note our choice of l_{slip} leads to a situation where the slip length is larger than the thickness of the air film. However, this was also the case in our previous work on the parallel-plate system [31], yet the hydrodynamic model yielded predictions consistent with key experimental observations. This suggests that slip in the air phase, while necessary to include, may not play a dominant role in determining the main aspects of dynamic wetting failure for the flows considered in [31].

We consider values of U (substrate speed) from ~ 0.1 to 10 m/s and V (feed flow velocity) from ~ 0.1 to 1 m/s, and take the slot width w to be 1 mm. With the parameter choices listed above, this yields values of h_{inf} from ~ 0.1 to 1 mm (Appendix B). In addition, Ca varies from ~ 0.1 to 2.5, Re varies from ~ 1 to 40, Bo varies from $\sim 10^{-3}$ to 10^{-1}, and the dimensionless slip length λ varies from $\sim 10^{-2}$ to 10^{-1}. Note that since the liquid properties are fixed, Ca, Re, Bo, and λ change as the substrate speed and feed flow velocity are varied.

4.3 Influence of receding phase and comparison with parallel-plate system

In this section, the influence of the receding phase on wetting failure in curtain coating is studied. A comparison of the critical capillary number Ca^{crit} is also made between curtain coating and the parallel-plate system examined in our previous work[23, 31, 26, 83] (Figure 4.1(b)) to demonstrate the influence of the curtain flow on the onset of wetting failure.

The macroscopic contact angles θ_M (Figure 4.2) are determined as a function of the capillary number Ca to construct steady-state solution paths (Figure 4.4(a)). Solution paths are computed for zero and non-zero viscosity ratios $\chi = \mu_{rec}/\mu_{adv}$ in curtain coating to demonstrate the influence of the viscosity in the receding phase μ_{rec}.

For $\chi > 0$ ($\chi = 10^{-2}$, blue squares and 7.2×10^{-4}, black diamonds), θ_M increases

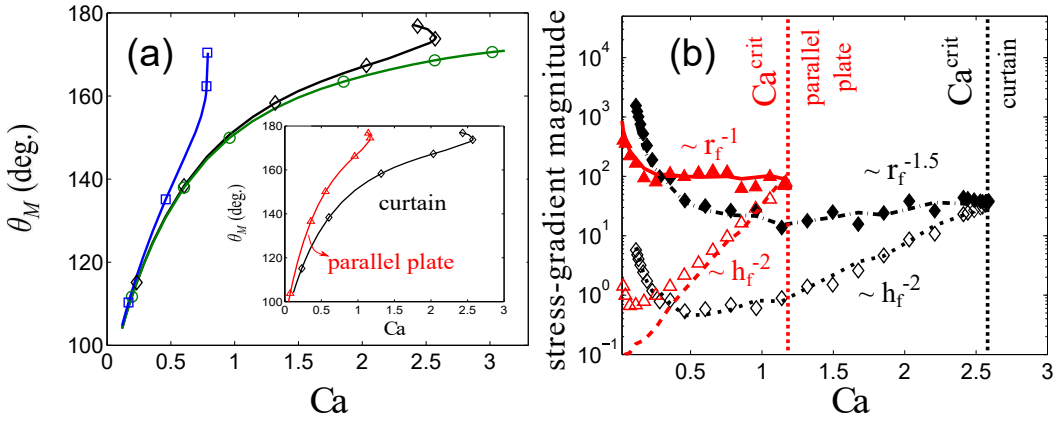

Figure 4.4: (a) Solution paths for various viscosity ratio χ values: $\chi = 10^{-2}$ (blue squares), $\chi = 7.2 \times 10^{-4}$ (black diamonds), and $\chi = 0$ (green circles) in curtain coating. *Inset*: Solution paths for $\chi = 7.2 \times 10^{-4}$ in curtain coating (black diamonds) and the parallel-plate system (red triangles). (b) Magnitude of stress gradients at the interface inflection point (IP) for curtain coating (black diamonds) and the parallel-plate system (red triangles) for $\chi = 7.2 \times 10^{-4}$. The capillary-stress gradients (filled symbols) match the air-pressure gradients (open symbols) at Ca^{crit} values denoted by dotted lines. Values of other parameters are $x_{DCL} = 0$ and $\theta_{mic} = 90^o$. For the parallel-plate system, the scaled slip length $\lambda = 10^{-2}$. For curtain coating when $\chi = 7.2 \times 10^{-4}$, λ varies from 0.0096 to 0.095 as Ca increases.

with Ca until reaching a limit point at a critical capillary number Ca^{crit} (Figure 4.4(a)). Beyond this Ca^{crit} value ($Ca > Ca^{crit}$), we are unable to find any 2D steady-state solutions. We assume that this corresponds to the point where the system develops 3D or transient flows resulting in wetting failure [31, 100]. However, if the receding air is not accounted for ($\chi = 0$, green circles), the system appears to maintain steady 2D wetting with $\theta_M \to 180^o$ as the substrate speed approaches infinity ($Ca \to \infty$). Similar behavior is also predicted in fluid displacement between parallel plates [31] and in plunge coating [110, 25].

Figure 4.4(a) clearly demonstrates the influence of the receding flow on the Ca^{crit} values. With a high-viscosity receding gas ($\chi = 10^{-2}$), the system tends to have wetting failure at a smaller substrate speed, which is consistent with prior studies in parallel-plate geometries [31, 93, 97, 32]. However, the onset of wetting failure is completely missed when neglecting stress contributions from the receding phase ($\chi = 0$). Therefore, it is crucial to incorporate the stresses from the receding phase to even predict the onset of wetting failure in curtain coating. Although curtain coating has been studied in previous work [15, 13, 10, 149, 142], to the best of the authors' knowledge this is the first work that predicts the onset of wetting failure in this important flow.

As mentioned in Sec. 4.1.2, the flows in curtain coating and the parallel-plate system are significantly different. The main difference lies in the impinging liquid curtain that may lead to high hydrodynamic pressure near the DCL (Figure 4.1). The inset of Figure 4.4(a) demonstrates the influence of the liquid curtain on Ca^{crit} and θ_M. At this particular set of conditions, the critical capillary number in curtain coating is almost twice that obtained in the parallel-plate system. (Inertial and gravitational effects are neglected in the parallel-plate system. For curtain coating, $Re = 30.37$, and $Bo = 1.54 \times 10^{-3}$ at $Ca = Ca^{crit}$.)

This delay in the onset of wetting failure in curtain coating agrees with prior experimental observations: by manipulating the flow in curtain coating, the critical coating speed (i.e., air entrainment) is delayed and the dynamic contact angles are reduced in comparison with plunge coating [14, 138, 137, 139]. The term "hydrodynamic assist" is used to describe the delay of air entrainment caused by manipulation of the flow (Sec. 4.1.1) [14]. In Sec. 4.4, we will propose a physical explanation of hydrodynamic assist by using a stress-gradient analysis near the DCL.

Although the values of the dimensionless slip lengths are comparable in the two systems, their definitions are not the same (one is scaled by the gap width H between the two plates (Figure 4.1) and the other is scaled by Q/U). Therefore, to study the mechanism of hydrodynamic assist, the analysis in Sec. 4.4 will only focus on curtain coating.

In prior work on wetting failure in the parallel-plate geometry, we proposed that wetting failure occurs when capillary-stress gradients can no longer provide the pressure gradient required to pump the receding fluid away from the DCL [31]. To examine whether this wetting-failure mechanism is still valid in curtain coating, capillary-stress gradients (filled symbols) and air-pressure gradients (open symbols) at the interface inflection point (IP) in curtain coating (black diamonds) and the parallel-plate system (red triangles) are plotted as a function of Ca in Figure 4.4(b). The critical capillary number Ca^{crit} in each system corresponds to the flow condition where the capillary-stress and air-pressure gradients match, indicating that the physical mechanisms that govern wetting failure in both systems are similar despite the significant difference in geometry and flow fields. Note that the pressure gradient in the receding phase grows faster than the capillary-stress gradient as Ca increases, thereby imposing a limitation to dynamic wetting.

Use of lubrication theory and the slip boundary condition yields the prediction that the magnitude of the capillary-stress gradient $\sim r_f^{-1}$, where r_f is the distance to the IP (Figure 4.2) [31, 83]. This scaling is obeyed by the data from the parallel-plate system, but the data from curtain coating show a stronger dependence on the IP location ($\sim r_f^{-1.5}$) (Figure 4.4(b)). In both systems, the air-pressure gradient $\sim h_f^{-2}$ (Figure 4.4(b)), where h_f is the IP height, consistent with lubrication theory [31, 83].) The stronger dependence of the capillary-stress gradient on the IP location in curtain coating can be attributed to the hydrodynamic pressure exerted by the impinging curtain (see Sec. 4.4 for more details).

4.4 Hydrodynamic assist in curtain coating

As mentioned in Sec. 4.1.1, hydrodynamic assist is the manipulation of curtain coating to assist dynamic wetting and delay the onset of wetting failure (i.e., air entrainment)

[14, 10]. Prior experimental observations show that hydrodynamic assist is sensitive to the DCL position x_{DCL} [14, 138, 137, 140, 150, 151, 152]. In this section, we first show the flow fields for different x_{DCL} and connect these with prior experimental observations [14, 150, 151, 152]. We then propose a physical mechanism for hydrodynamic assist based on these flow fields and a stress-gradient analysis.

4.4.1 Flow fields with different x_{DCL}

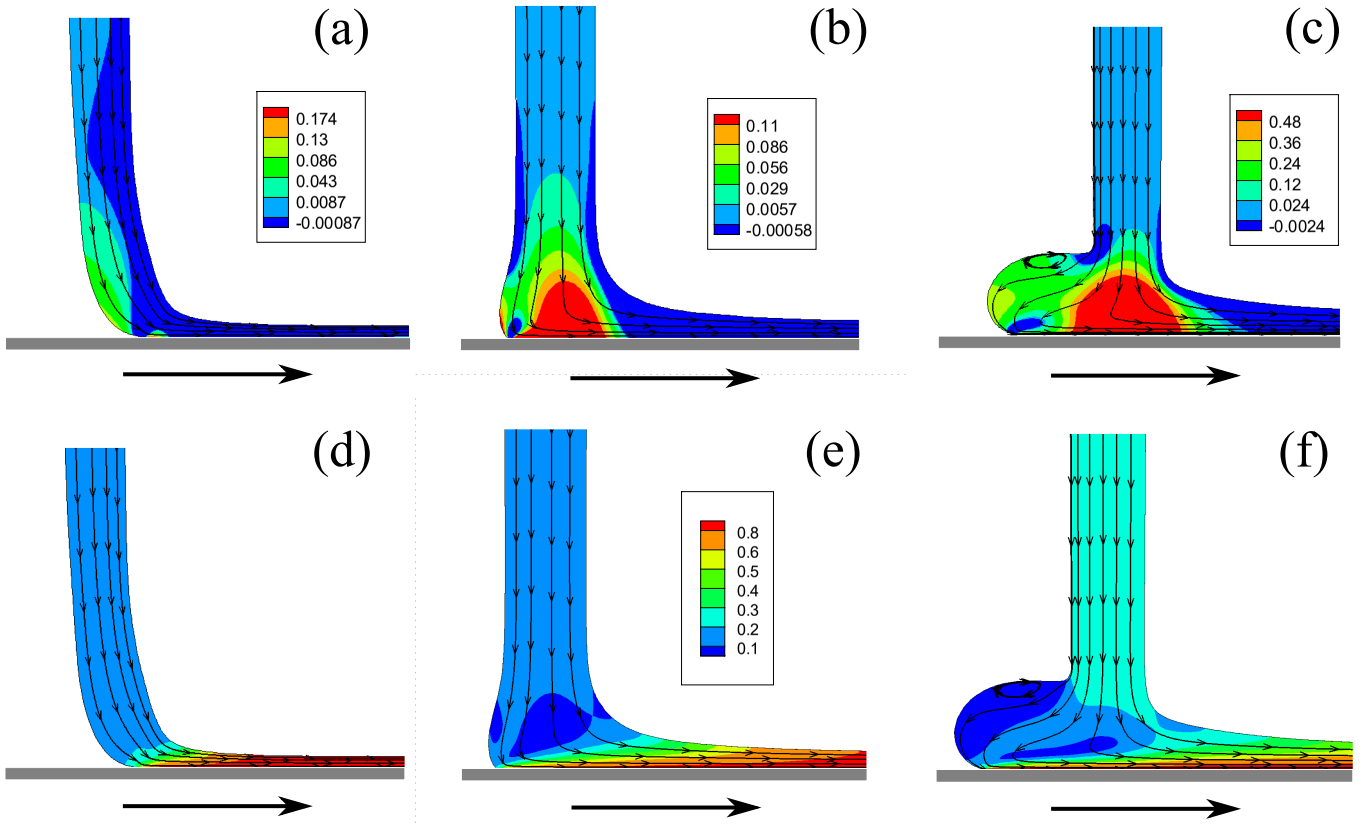

Figure 4.5: (a)-(c) Pressure contours and (d)-(f) velocity-magnitude contours for various x_{DCL} values: $x_{DCL} = 1$ ((a),(d)), $x_{DCL} = 0$ ((b),(e)), and $x_{DCL} = -1$ ((c),(f)). Values of other parameters are viscosity ratio $\chi = 7.2 \times 10^{-4}$ and $\theta_{mic} = 90^o$. Here, $Ca = 1.33$ ($x_{DCL} = 1$), 2.59 ($x_{DCL} = 0$), and 1.36 ($x_{DCL} = -1$). Note that $Ca = Ca^{crit}$ except the case of $x_{DCL} = -1$. In addition, $Re = 11.99$, ($x_{DCL} = 1$), 30.37 ($x_{DCL} = 0$), and 34.93 ($x_{DCL} = -1$), and $Bo = 9.12 \times 10^{-4}$ ($x_{DCL} = 1$), 1.54×10^{-3} ($x_{DCL} = 0$), and 7.33×10^{-3} ($x_{DCL} = -1$).

Air/liquid displacement ($\chi = 7.2 \times 10^{-4}$) in curtain coating is studied at various positions of x_{DCL}, which is controlled by the feed flow velocity V in experiments at fixed substrate speed U and curtain height h_{curt} [14, 10, 152, 147]. Decreasing V allows the substrate to drag the DCL downstream, whereas increasing V tends to move the DCL upstream.

Figure 4.5 shows pressure contours ((a)-(c)) and velocity-magnitude contours ((d)-(f)) for three flow configurations (corresponding to three x_{DCL} values) in curtain coating [14, 10, 152, 151, 150]: bead pulling ((a),(d); $x_{DCL} > 0$), DCL right beneath the liquid curtain ((b),(e); $x_{DCL} = 0$), and heel formation ((c),(f); $x_{DCL} < 0$). Because it is easiest to compare different cases when the spatial scales are the same, all lengths have been rescaled by the slot width w in this plot and subsequent ones. Note that the first two cases are at their respective critical capillary numbers Ca^{crit}, whereas the last one is not. This is because in the last case mesh distortion is so strong that it prevents us from obtaining converged solutions before Ca^{crit} can be clearly identified. Impinging liquid pressurizes the flow underneath the curtain, with the effect being most prominent when the DCL is right beneath the liquid curtain and in the heel-formation configuration. The effect is not as prominent in the bead-pulling configuration since the curtain is dragged by the substrate.

Prior experimental observations suggest that hydrodynamic assist is most influential (i.e., the substrate speed U^{crit} is maximum) when the contact line is right beneath the liquid curtain [14, 138, 140, 15]. Our results show that when $x_{DCL} = 0$, Ca^{crit} is the largest and its value is almost twice that when $x_{DCL} = 1$ (Figure 4.5(a)-4.5(b)). The degree of hydrodynamic assist is related to the distance between the DCL and the curtain impingement position (i.e., right beneath the upstream tip of the slot die) (Figure 4.5(a)-4.5(c)). Hydrodynamic pressure due to the inertia of the liquid curtain has the strongest effect when the impingement position overlaps the DCL (i.e., $x_{DCL} = 0$) because dynamic wetting and wetting failure take place at the DCL (i.e., air bubbles break off vertices of the sawtooth-shaped DCL) [6, 26].

In contrast, in the bead-pulling configuration, the effect of hydrodynamic assist is weakened because the high-pressure region is not as prominent and the DCL is away from the impingement position (Figure 4.5(a)). In the heel-formation configuration, although hydrodynamic pressure is enhanced under the curtain, the increased distance

between the impingement position and the DCL results in weak hydrodynamic assist (Figure 4.5(c)).

In all the flow configurations, liquid must accelerate near the DCL to match the substrate velocity (Figure 4.5(d)-4.5(f)). Consequently, liquid pressure decreases sharply near the DCL, providing a pressure gradient that draws liquid toward the moving substrate (Figure 4.5(a)-4.5(c)). The low-pressure zone paired with the high-pressure region under the curtain allows the $x_{DCL} = 0$ case to achieve high coating speeds (Figure 4.5(b)). In the heel-formation configuration, however, the high pressure under the curtain is located far from the DCL and directs liquid upstream (Figure 4.5(c)). This results in a recirculation region (Figure 4.5(f)), similar to what is observed experimentally [141].

4.4.2 Mechanism of hydrodynamic assist

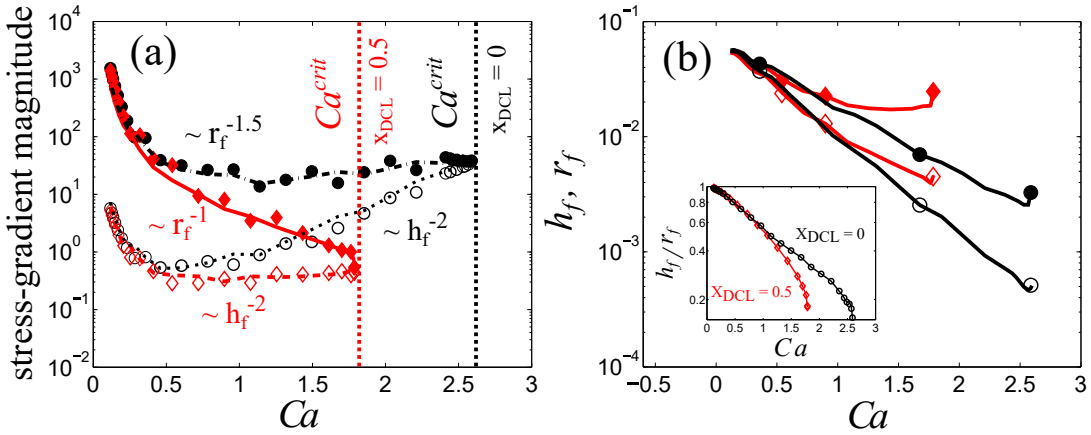

Figure 4.6: (a) Magnitude of capillary-stress (filled symbols) and air-pressure (open symbols) gradients at the inflection point (IP) for $x_{DCL} = 0$ (black circles) and $x_{DCL} = 0.5$ (red diamonds). (b) IP radial distance r_f (filled symbols) and height h_f (open symbols) as a function of Ca for $x_{DCL} = 0$ (black circles) and $x_{DCL} = 0.5$ (red diamonds). *Inset*: The ratio between the two length scales for $x_{DCL} = 0$ (black circles) and $x_{DCL} = 0.5$ (red diamonds). Values of other parameters are viscosity ratio $\chi = 7.2 \times 10^{-4}$ and $\theta_{mic} = 90^o$.

As noted in Sec. 4.3, the mechanism of wetting failure is similar in curtain coating and the parallel-plate system. Here, we investigate the influence of hydrodynamic assist on the wetting-failure mechanism. Figure 4.6(a) shows the capillary-stress gradient

(filled symbols) and air-pressure gradient (open symbols) at the interface inflection point (IP) as a function of Ca for $x_{DCL} = 0$ (black circles) and $x_{DCL} = 0.5$ (red diamonds). Notably, when $x_{DCL} = 0$ the capillary-stress gradient is larger and has a stronger dependence on the inflection point (IP) location ($\sim r_f^{-1.5}$) in comparison with the case when $x_{DCL} = 0.5$ ($\sim r_f^{-1}$). We point out that the r_f^{-1} behavior observed when $x_{DCL} = 0.5$ is similar to that in the previously examined parallel-plate geometry (Figure 4.4(b)). Therefore, the stronger dependence of the capillary-stress gradient on r_f when $x_{DCL} = 0$ can be attributed to the presence of hydrodynamic assist.

Figure 4.6(b) shows the change of the interface inflection point (IP) height h_f (filled symbols) and radial distance r_f (open symbols) with Ca (see Figure 4.2 for h_f and r_f definitions). For both $x_{DCL} = 0$ (black circles) and $x_{DCL} = 0.5$ (red diamonds), the IP migrates toward the DCL (i.e., h_f and r_f decreasing) as Ca increases because the interface curvature needs to increase to balance the increasing viscous stresses from the air. Notably, the IP for $x_{DCL} = 0$ is closer to the DCL than that for $x_{DCL} = 0.5$ as Ca approaches the onset of wetting failure, meaning that the interface curvature for $x_{DCL} = 0$ is larger than that for $x_{DCL} = 0.5$. As a result, the capillary-stress gradient for $x_{DCL} = 0$ is larger than that for $x_{DCL} = 0.5$, which is consistent with what is shown in Figure 4.6(a).

The inset of Figure 4.6(b) shows the ratio between h_f and r_f for $x_{DCL} = 0$ and $x_{DCL} = 0.5$. This ratio is related to the angle of the wedge formed in the receding phase (Figure 4.2); a larger ratio corresponds to a smaller macroscopic contact angle θ_M. The inset of Figure 4.6(b) shows that this ratio is larger when $x_{DCL} = 0$. This is a consequence of the strong hydrodynamic pressure near the DCL when $x_{DCL} = 0$, which suppresses the penetration of air film. Therefore, the model results suggest that the macroscopic contact angle θ_M in curtain coating is reduced by hydrodynamic assist, which is consistent with experimental observations that hydrodynamic assist leads to a reduction in the dynamic contact angle θ_D [138, 141, 137, 142]. In Sec. 4.5, we will discuss the influence of air stresses on the contact-angle behavior.

Altogether, Figure 4.5 and Figure 4.6 suggest that hydrodynamic assist can be attributed to the strong pressure generated by the inertia of the impinging curtain. This pressure creates large gradients in the interface curvature near the DCL, which in turn enhances the capillary-stress gradient there and lowers the the dynamic contact angle.

These larger capillary-stress gradients more effectively pump air away from the DCL and delay the onset of wetting failure.

4.5 Variation of dynamic contact angle with feed flow rate

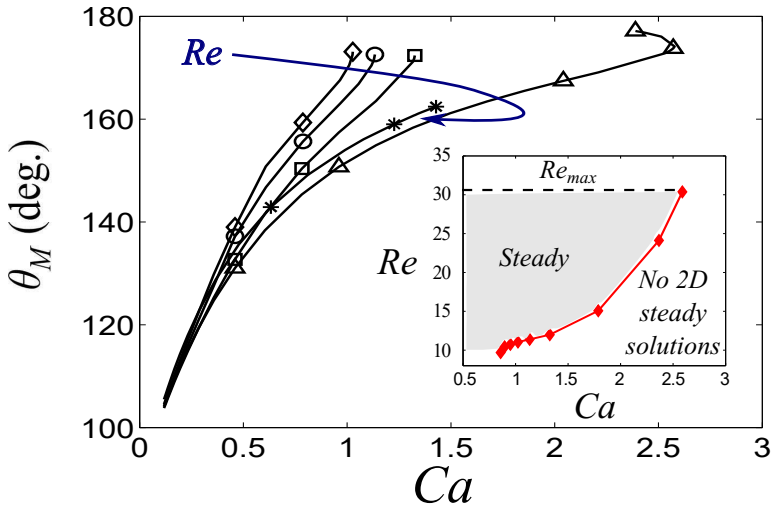

Figure 4.7: Solution paths for various x_{DCL} values (i.e., feed flow rates) when viscosity ratio $\chi = 7.2\times10^{-4}$: $x_{DCL} = 3$ ($Re = 11.04$, diamonds), $x_{DCL} = 2$ ($Re = 11.39$, circles), $x_{DCL} = 1$ ($Re = 11.99$, squares), $x_{DCL} = 0$ ($Re = 30.37$, triangles), and $x_{DCL} = -1$ ($Re = 34.93$, asterisks). Note that the listed Re values are those for the largest Ca in the respective solution paths. *Inset*: Coating window with Re_{max} corresponding to the flow condition where $x_{DCL} = 0$. Values of other parameters are $\chi = 7.2 \times 10^{-4}$ and $\theta_{mic} = 90^o$. The corresponding values of Bo are 1.30×10^{-3}, 1.12×10^{-3}, 9.12×10^{-4}, 1.54×10^{-3}, and 7.33×10^{-3}.

As mentioned in Sec. 4.1.1, varying the feed flow rate $Q = wV$ in curtain coating can delay the onset of wetting failure (i.e., increase the critical capillary number Ca^{crit}). Flow visualizations show that the dynamic contact angle also varies with Q [14, 138]. In this section, we examine the influence of Q on Ca^{crit} and the macroscopic contact angle θ_M. Because the Reynolds number $Re = \rho V w/\mu_{adv}$ is directly proportional to the feed flow velocity V, we use it as a proxy for the feed flow rate.

Steady-state solution paths for various values of x_{DCL} are shown in Figure 4.7. As mentioned in Sec. 4.2.3, we fix the value of x_{DCL} and calculate Re as we trace the solution paths to higher capillary numbers Ca. The results show that at the largest Ca

for each x_{DCL}, the corresponding Re (i.e., feed flow rate) increases as the DCL moves upstream (i.e., decreasing x_{DCL}).

Due to strong mesh distortion, the solution path for the heel-formation configuration ($x_{DCL} = -1$, asterisks in Figure 4.7) does not reach a limit point and thus the corresponding Ca^{crit} can not be computed. However, it is clear that when $x_{DCL} = -1$, the macroscopic contact angles θ_M are increased in comparison with $x_{DCL} = 0$ (triangles), suggesting that wetting failure occurs at a smaller Ca^{crit}. Therefore, Figure 4.7 implies that Ca^{crit} increases first and then decreases as the feed flow rate increases. To the best of the authors' knowledge, this is the first time the non-monotonic behavior of Ca^{crit} (i.e., air entrainment) in curtain coating has been predicted.

Among the various cases shown in Figure 4.7, the solution path for $x_{DCL} = 0$ shows the maximum Ca^{crit}, which is similar to experimental observations that the maximum hydrodynamic assist occurs when the DCL is right beneath the curtain [14, 138, 140]. Figure 4.7 also shows that at a given Ca, increasing the feed flow rate leads to a non-monotonic behavior of θ_M (i.e., the angle decreases first then increases), which has been predicted by Wilson et al. [15, 143] in simulations that do not account for the air phase and will be discussed further below.

A coating window can be predicted by our model, as shown in the inset of Figure 4.7. Here, Re is plotted as a function of Ca to demonstrate the high-speed limit (i.e., air entrainment) in curtain coating. The shaded area represents a steady coating regime, where Re_{max} corresponds to flow conditions at the maximum Ca^{crit} ($x_{DCL} = 0$). As Re increases, Ca^{crit} increases and the regime of steady coating (at a fixed Re) enlarges, suggesting that inertia is essential in curtain coating for maintaining steady wetting at higher speeds. However, because critical capillary numbers could not be computed for $Re > Re_{max}$ (associated with the heel-formation configurations, $x_{DCL} < 0$), this plot only shows part of coating window usually observed in experiments [138, 137, 78, 147, 151].

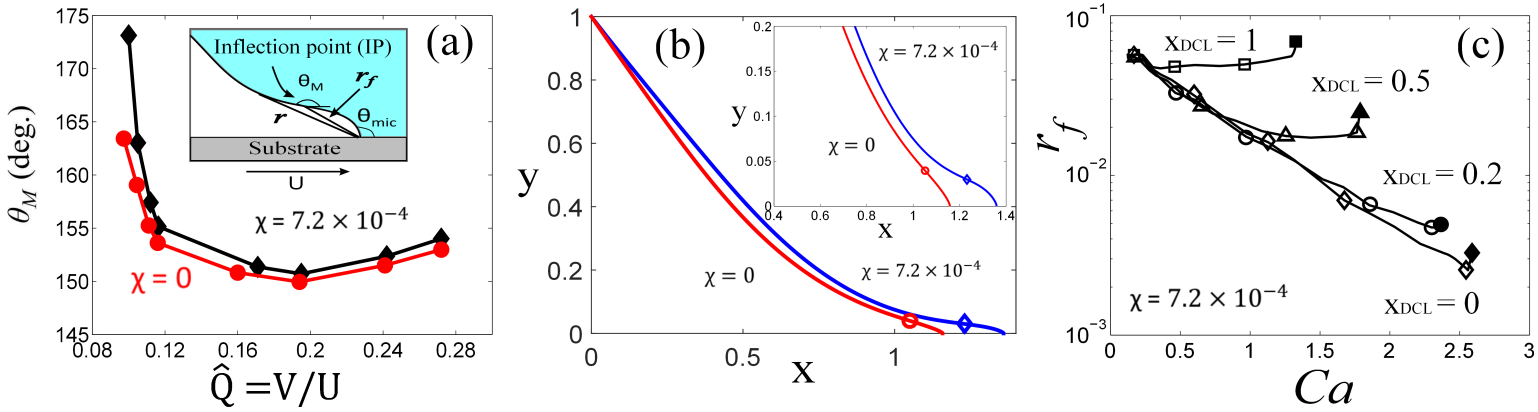

Figure 4.8: (a) Variation of macroscopic contact angles at the interface inflection point (IP) with $\hat{Q}$ for viscosity ratio $\chi = 7.2 \times 10^{-4}$ (diamonds) and $\chi = 0$ (circles). (b) Interface profiles for $\chi = 7.2 \times 10^{-4}$ (blue diamond) and $\chi = 0$ (red circle) when $\hat{Q} = 0.1$. The dynamic contact line (DCL) is at $y = 0$ and symbols mark the IPs. *Inset*: Interface profiles near $y = 0$. (c) IP radial distance r_f as a function of Ca for various x_{DCL} values when $\chi = 7.2 \times 10^{-4}$: $x_{DCL} = 1$ (squares), $x_{DCL} = 0.5$ (triangles), $x_{DCL} = 0.2$ (circles), $x_{DCL} = 0$ (diamonds). Values of other parameters are $\theta_{mic} = 90^o$ and $Ca = 0.96$.

As noted in Sec. 1.1, the predictions reported by Wilson et al.[15, 143] show that the reduction in the apparent contact angle (i.e., interface angle calculated 20 μm from the DCL) is much smaller ($< 10^o$) than that in dynamic contact angle θ_D ($\sim 20^o$) observed experimentally by Blake et al.[138] Since their model does not consider the contribution of air stresses, here we investigate how the presence of air stresses influences the variation of θ_M with feed flow rate.

The variation of macroscopic contact angle θ_M with feed flow rate is shown in Figure 4.8(a), where θ_M is plotted as a function of $\hat{Q} = V/U$ at $Ca = 0.96$ (i.e., fixing substrate speed U and varying feed flow velocity V). Curves of θ_M in both air/liquid ($\chi = 7.2 \times 10^{-4}$, diamonds) and void/liquid ($\chi = 0$, circles) systems show a minimum corresponding to the smallest θ_M. This trend is consistent with the non-monotonic behavior of the dynamic contact angle θ_D observed experimentally [138, 141].

Although the curtain height ($h_{curt} = 1$ cm) in our model is not the same as that studied by Wilson et al. ($h_{curt} = 3$ cm)[15, 143], the largest angle reduction predicted by our model in air/liquid displacement is around 20^o (diamonds in Figure 4.8(a)), which is very close to the experimental value reported by Blake et al. ($\sim 20^o$) [138]. In contrast, the angle reduction in void/liquid displacement ($\sim 15^o$) is smaller than that in air/liquid displacement. If we calculate an apparent contact angle at a distance of 20 μm from the DCL as done by Wilson et al.[15, 143], the angle reductions are smaller and closer. For air/liquid displacement it is $\sim 8^o$, whereas for void/liquid displacement it is $\sim 7^o$.

The larger reduction of θ_M in air/liquid displacement suggests that the air phase plays a crucial role in curtain coating. This is because air stresses also contribute to determining the shape of the interface near the DCL [31, 93] and the value of θ_M, especially near the onset of wetting failure (Figure 4.4(a)). Figure 4.8(b) shows the influence of the receding-phase viscosity on the interface profile. At large scales, the interface profiles in the presence and absence of air look very similar, as illustrated in the main panel. At smaller scales, however, the inset shows that the air has a significant influence on interface shape. The interface inflection point (IP) is closer to the DCL and interface is more elongated when the air viscosity is included.

The migration of the IP for various feed flow rates (i.e., x_{DCL}) is shown in Figure 4.8(c). The solid symbols in each curve represent the radial distance r_f of the IP (Figure

4.2) at the respective Ca^{crit}. The IP for $x_{DCL} = 0$ (diamond) is closer to the DCL than those in other cases, consistent with a lower value of θ_M (Figure 4.7). As the DCL moves away from $x_{DCL} = 0$ (i.e., $x_{DCL} > 0$), the IP migration paths deviate from that for $x_{DCL} = 0$ and stop at smaller Ca^{crit} values, consistent with higher values of θ_M. In dimensional terms, the radial distance to the IP at $Ca = 0.96$ varies from ∼18 μm for $x_{DCL} = 0$ to ∼50 μm for $x_{DCL} = 1$. These distances are comparable to what can be resolved experimentally.

Although the predicted Ca^{crit} values are of a similar order of magnitude as prior experiments ($0.3 < Ca < 50$) [138, 137, 147], the difference in curtain height between our model and experimental setups prevents us from drawing more definitive conclusions. However, our results suggest that accounting for the air stresses near the DCL is necessary to properly describe experimental observations reported by Blake et al. [138].

4.6 Influence of insoluble surfactants on curtain coating

Motivated by the experiments of Marston et al. [78] discussed in Sec. 4.1.3, we examine here the influence of Marangoni stresses on wetting failure in curtain coating. Marston et al. [78] observed that U^{crit} could be reduced by up to $\sim 66.7\%$ upon the addition of surfactants, which corresponds to a reduction in Ca^{crit} of $\sim 36\%$. We examine here whether Marangoni stresses could be a possible mechanism for this.

Based on the parameters reported by Marston et al. [78], we estimate that the Marangoni number M at the onset of wetting failure is $O(1)$ or smaller and the Peclet number Pe is $O(10^5)$ (see M and Pe definitions in Sec. 4.2.2). Thus, $M = 0.15$ and $Pe = 10^3$ are chosen as representative Marangoni and Peclet numbers in our calculation. Based on our previous work in the parallel-plate geometry, $Pe = 10^3$ is large enough to be in the convection-dominated limit [83].

4.6.1 Solution paths

The solution paths for different Marangoni numbers when $x_{DCL} = 0$ are shown in Figure 4.9. We choose to fix $x_{DCL} = 0$ because this is where hydrodynamic assist is maximum, both in the presence and absence of surfactants. The solution path for $M = 0$ (circles) corresponds to the case where surfactants are absent (Figure 4.7). Notably, the presence

of Marangoni stresses ($M > 0$) decreases Ca^{crit} and promotes the onset of wetting failure, suggesting a possible mechanism for the experimental observations of Marston et al. [78]. Figure 4.9 also demonstrates that increasing the strength of Marangoni stresses (i.e., higher M or surfactant concentration) will further decrease Ca^{crit}, which was also experimentally observed by Marston et al. [78].

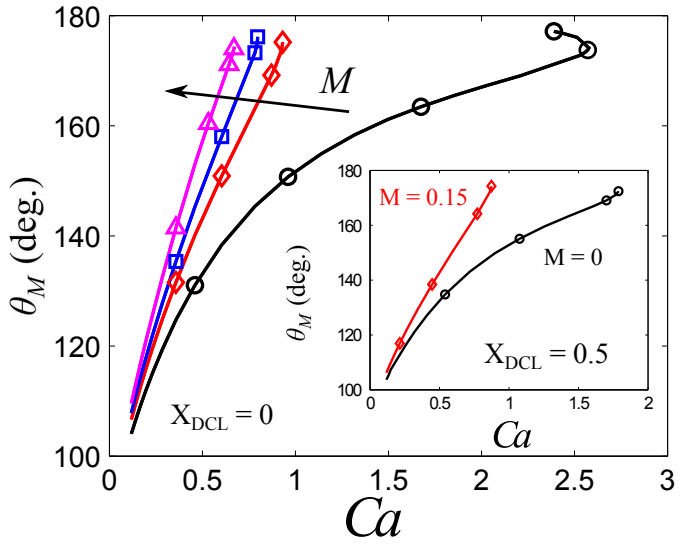

Figure 4.9: Solution paths for various M when $x_{DCL} = 0$: $M = 0$ (black circles), $M = 0.15$ (red diamonds), $M = 0.3$ (blue squares), and $M = 0.75$ (magenta triangles). *Inset*: Solution paths for $M = 0$ (black circles) and $M = 0.15$ (red diamonds) when $x_{DCL} = 0.5$. Values of other parameters are viscosity ratio $\chi = 7.2 \times 10^{-4}$ and $\theta_{mic} = 90^o$. For $x_{DCL} = 0$, $Re = 30.37$, and $Bo = 1.54 \times 10^{-3}$ at $Ca = Ca^{crit}$ when $M = 0$. For $x_{DCL} = 0.5$, $Re = 15.07$, and $Bo = 7.94 \times 10^{-4}$ at $Ca = Ca^{crit}$ when $M = 0$.

The inset of Figure 4.9 shows the solution paths for $M = 0$ and $M = 0.15$ at $x_{DCL} = 0.5$. As noted in Sec. 4.5, the feed flow rate at Ca^{crit} decreases as the DCL moves downstream. Therefore, the feed flow rates for solution paths in the inset of Figure 4.9 are smaller than those leading to $x_{DCL} = 0$ in Figure 4.9. Notably, in going from $x_{DCL} = 0$ to $x_{DCL} = 0.5$, Ca^{crit} decreases 30% for the surfactant-free case (i.e., $M = 0$). In contrast, the reduction in Ca^{crit} for $M = 0.15$ is only 6.3%, suggesting that the influence of the feed flow rate on the critical substrate speeds (i.e., the degree of hydrodynamic assist) is weakened by Marangoni stresses. This decreased degree of hydrodynamic assist is similar to what is observed by Marston et al. [78], again

indicating that Marangoni stresses may play an important role in curtain coating.

4.6.2 Mechanism of influence of surfactants

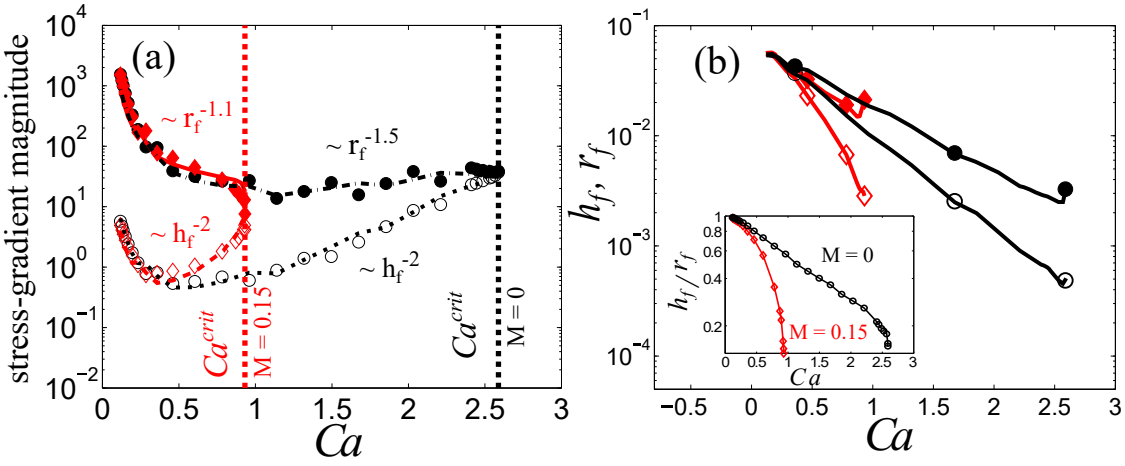

Figure 4.10: (a) Magnitude of stress gradients at the interface inflection point (IP) for $M = 0$ (black circles) and $M = 0.15$ (red diamonds). The capillary-stress gradients (filled symbols) match the air-pressure gradients (open symbols) at Ca^{crit} values denoted by dotted lines. (b) IP radial distance r_f (filled symbols) and height h_f (open symbols) as a function of Ca for $M = 0$ (black circles) and $M = 0.15$ (red diamonds). *Inset*: The ratio between the two length scales for $M = 0$ (black circles) and $M = 0.15$ (red diamonds). Values of other parameters are $x_{DCL} = 0$, viscosity ratio $\chi = 7.2 \times 10^{-4}$, and $\theta_{mic} = 90^o$.

Our previous work on the parallel-plate system (Figure 4.1(b)) suggests that Marangoni stresses promote the onset of wetting failure by thinning the air film between the fluid interface and the substrate [83]. However, since curtain coating has a significantly different geometry, it is not obvious that it shares the same physical mechanism. To address this issue, we perform a stress-gradient analysis.

Capillary-stress gradients (filled symbols) and air-pressure gradients (open symbols) at the interface inflection point (IP) are plotted as a function of Ca in Figure 4.10(a) when Marangoni stresses are absent ($M = 0$, black circles) and present ($M = 0.15$, red diamonds). Similar to what we found in our previous work on the parallel-plate geometry [83], the presence of Marangoni stresses tends to increase the air-pressure gradient (red open diamonds) such that it matches the capillary-stress gradient (red

filled diamonds) at a smaller Ca^{crit} compared to when $M = 0$.

Flow along the interface carries surfactant toward the DCL, creating large concentration gradients there (Figure 4.11). The surfactant concentration is largest near the DCL, leading to a Marangoni stress directed away from the DCL. Stronger shear stresses in the air phase are required to balance Marangoni stresses along the fluid interface (see (4.6)), and this requires air velocity changes over a smaller distance (du/dy) near the DCL. Therefore, the air film near the DCL is thinned (i.e., h_f decreases), increasing the magnitude of the air-pressure gradient, which scales as h_f^{-2} [31, 83].

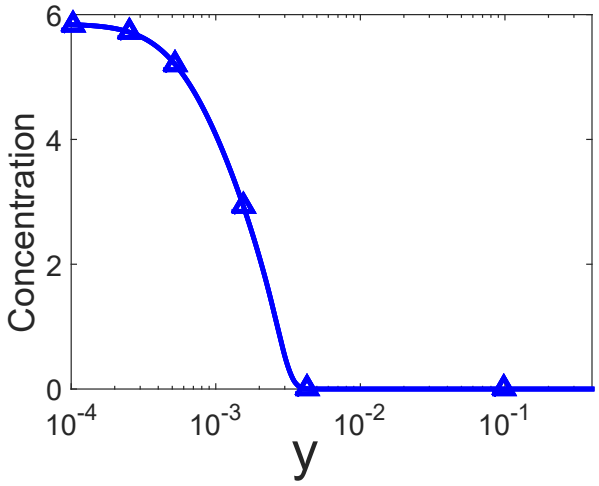

Figure 4.11: Surfactant concentration profile for $M = 0.15$ and $Ca = 0.93$. The dynamic contact line (DCL) is at $y = 0$. Values of other parameters are $x_{DCL} = 0$, viscosity ratio $\chi = 7.2 \times 10^{-4}$, and $\theta_{mic} = 90^o$.

Figure 4.10(b) demonstrates the migration of the inflection point (IP), where the characteristic length scales (r_f, filled symbols; h_f, open symbols) are plotted as a function of Ca. Notably, both r_f and h_f are smaller when $M = 0.15$ (diamonds) compared to when $M = 0$ (circles), indicating that the size of the air film shrinks in the presence of Marangoni stresses. Although smaller r_f values indicate a larger interface curvature and a stronger capillary-stress gradient, the decrease of h_f (with Ca) when $M = 0.15$ is so drastic that the air-pressure gradient increases rapidly and becomes equal to the capillary-stress gradient at a smaller Ca than that when $M = 0$.

The ratio between the two length scales (h_f/r_f) for $M = 0$ (circles) and $M = 0.15$

(diamonds) is shown in the inset of Figure 4.10(b). Due to the large reduction in h_f, the ratio for $M = 0.15$ is much smaller than that for $M = 0$. A smaller ratio corresponds to a larger macroscopic contact angle θ_M at the IP (Figure 4.2), which is consistent with the larger values of θ_M in the solution paths when $M > 0$ (Figure 4.9).

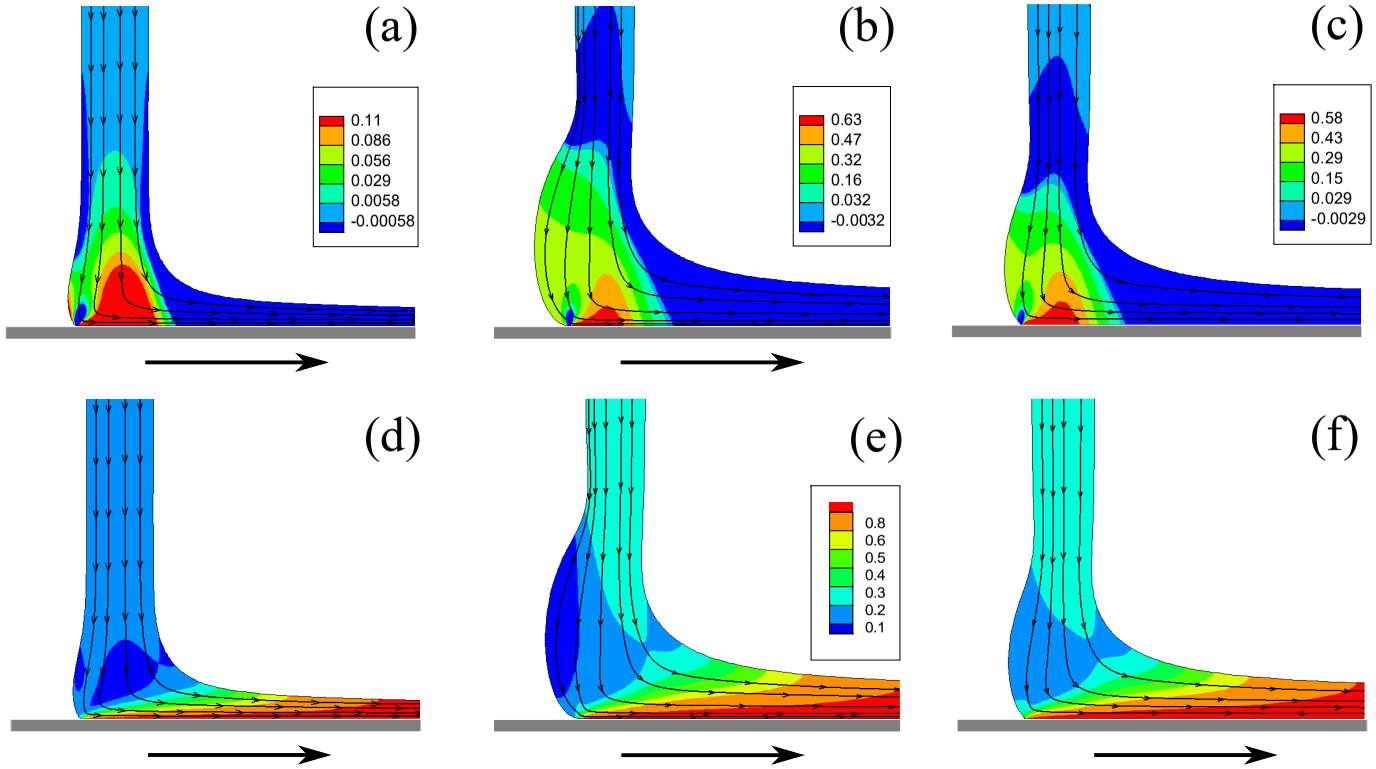

Figure 4.12: (a)-(c) Pressure contours and (d)-(f) velocity-magnitude contours for $M = 0$ ((a),(c),(d),(f)) and $M = 0.15$ ((b),(e)) at the onset of wetting failure. Values of other parameters are $x_{DCL} = 0$, viscosity ratio $\chi = 7.2 \times 10^{-4}$, and $\theta_{mic} = 90^o$. (a),(d) $Ca = 2.59$, $Re = 30.37$, and $Bo = 1.54 \times 10^{-3}$. (b),(e) $Ca = 0.93$, $Re = 21.41$, and $Bo = 5.89 \times 10^{-3}$. (c), (f) $Ca = 0.96$, $Re = 20.94$, and $Bo = 5.3 \times 10^{-3}$.

As discussed in Sec. 4.4, when Marangoni stresses are absent ($M = 0$), the strong dependence of the capillary-stress gradient on r_f when $x_{DCL} = 0$ can be attributed to the large pressure changes near the DCL ($\sim r_f^{-1.5}$ in Figure 4.10(a)). When Marangoni stresses are present ($M = 0.15$), Figure 4.10(a) shows that the dependence of capillary-stress gradients on r_f is weakened ($\sim r_f^{-1.1}$). To understand the reason for this, flow fields at the onset of wetting failure (i.e., at the respective Ca^{crit}) for $M = 0$ and $M = 0.15$ are presented in Figure 4.12.

Figure 4.12 shows pressure contours ((a)-(c)) and velocity-magnitude contours ((d)-(f)) for $M = 0$ and $M = 0.15$. Panels (a)-(b) and (d)-(e) are at the onset of wetting failure, and we note that the value of Ca^{crit} when $M = 0$ is larger than that when $M = 0.15$. Thus, panels (c) and (f) are for $M = 0$ at a value of Ca comparable to Ca^{crit} for $M = 0.15$. In all cases, $x_{DCL} = 0$.

When $M = 0$ (Figure 4.12(a), 4.12(d)), the curtain remains nearly perpendicular to the substrate and the impinging liquid pressurizes the flow underneath the curtain. In contrast, a liquid bulge is formed at the upstream fluid interface near the DCL when $M = 0.15$ (Figure 4.12(b), 4.12(e)). This liquid bulge results from the presence of Marangoni stresses, which counteract the impinging liquid and slow down the liquid velocity near the fluid interface and the DCL (Figure 4.12(e)). We note that the bulge is not as prominent when $M = 0$ and Ca has a comparable value to Ca^{crit} for $M = 0.15$ (Figure 4.12(c), 4.12(f)). The low-speed region when $M = 0.15$ (Figure 4.12(e)) indicates that inertial forces near the DCL are weakened, suggesting a weaker influence of the impinging liquid on the DCL compared to when $M = 0$. This weakened influence may explain the weaker dependence of the capillary-stress gradient on r_f when $M = 0.15$ (Figure 4.10(a)) and also the decrease in the degree of hydrodynamic assist observed by Marston et al. [78].

Finally, we comment on several other phenomena that may be present in the experiments but are not accounted for in our calculations. First, the surfactants used in the experiments of Marston et al. [78] were soluble, whereas our model assumes that the surfactants are insoluble. We expect that surfactant solubility will weaken Marangoni effects since surfactants could desorb from the fluid interface into the bulk. Second, our model does not account for the possibility that surfactants may adsorb to the substrate. Third, the introduction of surfactants will lower the mean surface tension and

the microscopic contact angle, which were taken as constant in the above calculations to isolate the influence of Marangoni stresses. Lowering θ_{mic} would be expected to raise the value of Ca^{crit} since the substrate would be more wettable. As this is the opposite of what is observed in the experiments, it is likely not the cause of the decrease in Ca^{crit}. Accounting for these phenomena as well as larger curtain heights will be important to more fully understand the experimental observation that surfactants significantly promote the onset of wetting failure.

4.7 Conclusions

We have used a novel hybrid formulation of a hydrodynamic model to study dynamic wetting failure and hydrodynamic assist in curtain coating. The use of a 1D description of the air phase has allowed, for the first time, an examination of the influence air stresses on this complicated coating flow. Indeed, without using a 1D description for the air phase, a full 2D description of the both the air and liquid phases would be computationally prohibitive.

Our model shows that inclusion of the air stresses is necessary to even predict the onset of wetting failure (Section 4.3). Once air stresses are included, our model is able to predict the non-monotonic behavior of the critical capillary number with feed flow rate that has been observed experimentally [138] (Section 4.5). Inclusion of air stresses also leads to a larger variation of dynamic contact angle with feed flow rate, suggesting that accounting for air stresses is important to accurately describe experimental observations of the dynamic contact angle [138]. In particular, our results raise the possibility that much of the behavior observed in curtain-coating experiments can be qualitatively understood by accounting for air stresses and assuming a constant microscopic contact angle.

Our model also allows us to gain insight into the phenomenon of hydrodynamic assist (Section 4.4). Similar to what is observed experimentally, we find that the degree of hydrodynamic assist is largest when the dynamic contact line is right beneath the liquid curtain. The hydrodynamic pressure generated by the inertia of the impinging curtain leads to larger gradients in interface curvature near the dynamic contact line. These larger curvature gradients lead to stronger capillary-stress gradients that are more

effective at pumping air away from the dynamic contact line, thus delaying the onset of wetting failure.

The influence of Marangoni stresses created by insoluble surfactants was also investigated, and we find that these stresses promote the onset of wetting failure and reduce the degree of hydrodynamic assist (Section 4.6). These findings are consistent with recent experimental observations [78] and suggest that Marangoni stresses are a possible mechanism. The Marangoni stresses thin the air film and increase the air-pressure gradients, making it more difficult for the capillary-stress gradients to pump the air away from the dynamic contact line.

Due to computational limitations, some of the the parameter values used in our model are quite different from those in experiments. Nevertheless, the model predictions are consistent with key experimental observations. We note that our assumption that the air can be described as a continuum in local thermodynamic equilibrium may break down as the air film becomes very thin [111]. It may also be important to account for slip at the air-liquid interface [111]. However, because the air film is long and slender, it may still be possible to describe its influence efficiently and accurately by using a 1D model.

The hybrid approach used here is limited principally by the degree to which the flow in the liquid phase can be resolved. Improvements in computational capacity will enable predictions of flows with parameters more representative of experimental setups (e.g., larger curtain heights), and thus allow for more quantitative comparisons with experimental data. If extended to 3D and transient flows, as well as to liquids with more complicated rheology, the hybrid approach may prove to be a computationally feasible way to accurately account for air stresses in these complex flows. Such an extension would be of interest not only for coating flows, but also for other problems in fluid mechanics such as rapid droplet spreading where there is a thin air layer near a dynamic contact line.

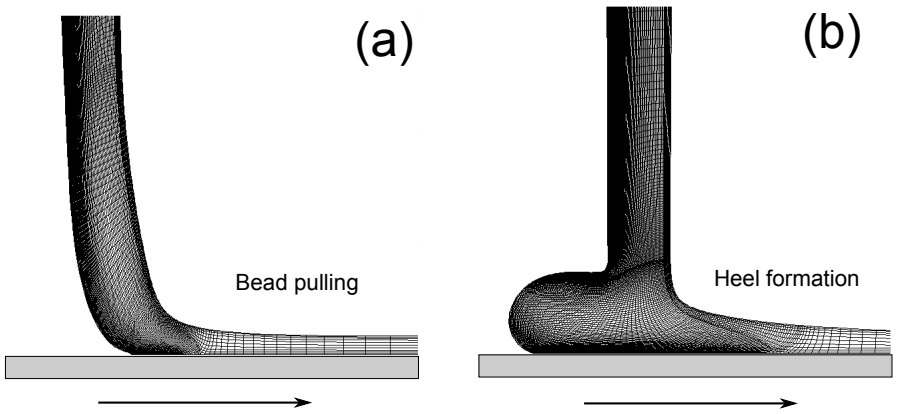

Figure 4.13: Mesh used in curtain coating for two flow configurations: (a) bead pulling and (b) heel formation.

4.8 Appendix

4.8.1 Finite element mesh

Figure 4.13 shows typical quadrilateral element meshes for two flow configurations: bead pulling (i.e., $x_{DCL} > 0$) and heel formation (i.e., $x_{DCL} < 0$). The highest concentration of elements is in the liquid domain near the DCL to resolve strong velocity and curvature gradients there. In the bead-pulling configuration, elements are stretched near the DCL. In contrast, in the heel-formation configuration elements are stretched both near the DCL and near the transition between the falling curtain and the heel. For the same initial element arrangement, calculations do not converge in the heel-formation configuration when $Ca \to Ca^{crit}$ because the mesh is strongly distorted. For this reason, we are not able to obtain Ca^{crit} values in the heel-formation configuration.

4.8.2 Dimensional velocities and film thicknesses

As noted in Sec. 4.2.3, we fix x_{DCL} as a flow parameter and calculate V (as a dependent variable) as we trace solution paths to higher U. As expected, the feed flow velocity V needs to increase as the substrate speed U increases to hold the DCL position fixed

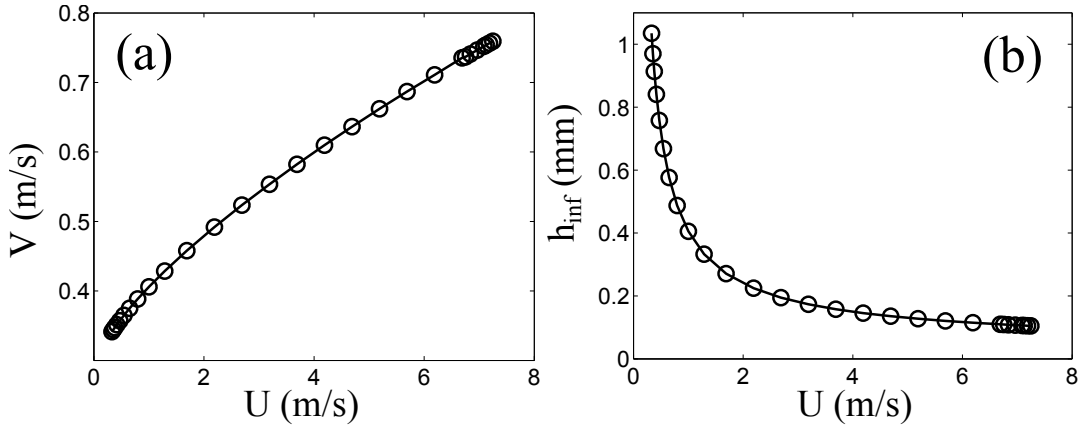

Figure 4.14: (a) Dependence of feed flow velocity V on substrate speed U in the absence of surfactants when $x_{DCL} = 0$. (b) Corresponding coating-film thickness h_{inf} from the balance of rates shown in (a). The parameters used for these calculations are given in Sec. 4.2.4.

(Figure 4.14(a)). However, V does not grow as fast as U, resulting in a decrease in coating-film thickness ($h_{inf} = wV/U$) as U increases (Figure 4.14(b)).

Chapter 5

Conclusions

In this thesis, the influence of surfactants on the onset of dynamic wetting failure has been investigated. Both experimental and computational approaches are used to address this problem. Mechanisms of surfactant effects on wetting failure are proposed, providing physical insights into prior experimental observations and our experimental data. In this chapter, a summary of this thesis and a discussion of future research directions are presented.

5.1 Thesis Summary

In Chapter 2 the influence of insoluble surfactants on dynamic wetting failure is investigated. A hydrodynamic model describing steady Stokes flows of dilute surfactant solutionst in a rectangular channel is developed. Three approaches are used to evaluate the model, which shows that steady wetting fails at a critical substrate speed corresponding to a critical capillary number Ca^{crit}. It is found that the 1D approach overestimates Ca^{crit} and incorrectly predicts the direction of surfactant concentration gradients when the receding phase has a viscosity much less than the advancing phase. On the other hand, the asymptotic theory of Cox [85] is found to match well predictions from the 1D/2D hybrid approach over a wide range of viscosity ratios. Analysis of our results reveals that the physical mechanisms for wetting failure is similar in the absence and presence of Marangoni stresses. Wetting failure occurs when the fluid interface cannot provide the pressure gradients needed to pump air away from the contact line.

The presence of Marangoni stresses promotes the onset of wetting failure by thinning the air film, which increases receding-phase pressure gradients near the contact line but does not significantly change the capillary-pressure gradients there.

In Chapter 3 a hydrodynamic model and complementary experiments are used to understand how soluble surfactants influence the onset of dynamic wetting failure. The model results demonstrate that surfactant solubility weakens the influence of Marangoni stresses, which we have shown in Chapter 2 would promote the onset of wetting failure. The influence of adsorption of surfactants to the substrate is studied as well. Our experiments show that Ca^{crit} increases with surfactant concentration. Comparison of the model predictions to the experimental observations reveals that for the more viscous solutions we used, the increase in Ca^{crit} with surfactant concentration can be largely attributed to the changes to the mean surface tension and static contact angle appear when surfactants are present. However, for the lowest viscosity solution used, the comparison shows that other surfactant-induced phenomena (such as nonlinear rate laws for surfactant adsorption) may become important.

In Chapter 4 a hybrid formulation of a hydrodynamic model is developed to study dynamic wetting failure and hydrodynamic assist in curtain coating. In this model air is described by a one-dimensional formulation and liquid by a 2D formulation. The model results show the need to account for the air stresses in order to predict the onset of wetting failure. The mechanisms of hydrodynamic assist in curtain coating is elucidated: the hydrodynamic pressure generated by the inertia of the impinging curtain leads to a strong capillary-stress gradient that pumps air away from the DCL and thus increases the critical substrate speed for wetting failure. Our model is able to capture key experimental observations, including (i) the non-monotonic behavior of the critical capillary number with feed flow rate and (ii) the condition that results in the largest hydrodynamic assist. The influence of insoluble surfactants is also investigated, and the results show that Marangoni stresses tend to thin the air film and increase air-pressure gradients near the DCL, thereby promoting the onset of wetting failure.

5.2 Future Direction

In this thesis we have studied surfactant effects on dynamic wetting failure using two model geometries which are motivated by industrial coating techniques. For the rectangular channel (see Chapter 2 & 3), a discrepancy exists between the model predictions and the experimental observations of the lowest viscosity solution used. This suggests that other surfactant-induced phenomena may become important in the experiments. For example, the slip length may vary with surfactant concentration, or the Navier-slip law (applied at the moving substrate near the DCL) with constant microscopic contact angle may break down in the presence of surfactants. To fully resolve this issue, measurements of surfactants along the fluid interface and the substrate are required. In addition, surfactant adsorption kinetics in a system consistent with our experimental conditions (e.g., liquid viscosity, surfactant concentration) are needed for more accurate model predictions.

In the curtain coating study (Chapter 4), although model results are able to show key experimental observations, some of the the parameter values used in the model are different from those in experiments due to computational limitations. These limitations also prevent us from obtaining the complete coating window for curtain coating. Note that the inset of Figure 4.7 only shows the lower part of coating window commonly seen in experiments. To address the issue, a model with a curtain height consistent with prior experimental conditions is under development where mesh numbers are increased and mesh sizes near the DCL are refined. In addition, it would be interesting to see how changes in mean surface tension of liquids influence the shape of coating windows. Our work in Chapter 4 mainly focuses on the Marangoni effects on wetting failure, but the comparison between model predictions and experimental data in Chapter 3 suggest that in more viscous liquids Maragnoni stresses may not be significant. This proposed work may provide insight into the experimental observations reported by Marston et al. [78].

Throughout this thesis, we have only considered Newtonian liquids (i.e., surfactant concentration is dilute and no non-Newtonian behaviors have been induced). In practice, coating liquids are a mixture of solvents, polymers, colourants, and surfactants

[153], exhibiting complex non-Newtonian characteristics (e.g., shear dependent viscosity, viscoelasticity, etc.). Due to the wide range of properties of non-Newtonian fluids, less systematic studies of dynamic wetting of non-Newtonian liquids have been published compared with those of Newtonian liquids [154, 41, 27, 155, 156]. Prior work in a simple flow geometry (i.e., drop spreading on a substrate) suggests that dynamic wetting strongly depends on the type of rheological properties of the non-Newtonian liquids studied [157, 158, 159]. In addition, it is found that the macroscopic flow geometry can also influence dynamic wetting of non-Newtonian liquids via changing the distribution of shear rate and viscosity in liquid flows [160]. Therefore, it is not clear how non-Newtonian characteristics influence the onset of dynamic wetting failure in different coating geometries.

5.3 Final remarks

In this thesis, we have studied the effects of surfactants on dynamic wetting failure by using experimental and computational approaches. Through these two approaches, the mechanisms by which surfactants influence dynamic wetting failure have been proposed. We believe that our work sheds light on the surfactant's role in coating flows and builds a solid foundation for future studies of wetting failure in complex liquids. Finally, we hope that this thesis provides some valuable insights into the coating formulation and the design of coating processes that can operate at higher speeds and waste less material.

References

[1] P. M. Schweizer and S. F. Kistler, editors. *Liquid Film Coating*. Springer Netherlands, 1997.

[2] S. F. Kistler. Hydrodynamics of wetting. In John C. Berg, editor, *Wettability*, pages 311–429. Marcel Dekker, Inc., 1993.

[3] L. E. Scriven and C. V. Sternling. The Marangoni effects. *Nature*, 187:186–188, 1960.

[4] R. T. Perry. *Fluid mechanics of entrainment through liquid-liquid and liquid-solid junctures*. PhD thesis, University of Minnesota, 1967.

[5] G Inverarity. Dynamic wetting of glass fibre and polymer fibre. *Brit. Polym. J.*, 1, 1969.

[6] T. D. Blake and K. J. Ruschak. A maximum speed of wetting. *Nature*, 282(5738):489–491, 1979.

[7] R. Burley and B. S. Kennedy. An experimental study of air entrainment at a solid/liquid/gas interface. *Chem. Eng. Sci.*, 31:901–911, 1976.

[8] R. Burley and R. P. S. Jolly. Entrainment of air into liquids by a high speed continuous solid surface. *Chem. Eng. Sci.*, 39(9):1357–1372, 1984.

[9] E. B. Gutoff and C. E. Kendrick. Dynamic contact angles. *AlChE J.*, 28(3):459–466, 1982.

[10] K. Miyamoto and Y. Katagiri. Curtain coating. In S.F. Kistler and P. M. Schweizer, editors, *Liquid Film Coating*, pages 463–494. Chapman & Hall, 1997.

[11] D. R. Brown. A study of the behaviour of a thin sheet of moving liquid. *J. Fluid Mech.*, 10(02):297–305, 1961.

[12] D. J. Hughes. Method for simultaneously applying a plurality of coated layers by forming a stable multilayer free falling vertical curtain. US Patent 3508947, 1970.

[13] S. F. Kistler. *The fluid mechanics of curtain coating and related viscous free surface flows with contact lines.* PhD thesis, University of Minnesota, 1985.

[14] T. D. Blake, A. Clarke, and K. J. Ruschak. Hydrodynamic assist of dynamic wetting. *AIChE J.*, 40(2):229–242, 1994.

[15] M. C. T. Wilson, J. L. Summers, Y. D. Shikhmurzaev, A. Clarke, and T. D. Blake. Nonlocal hydrodynamic influence on the dynamic contact angle: Slip models versus experiment. *Phys. Rev. E*, 73(4):041606, 2006.

[16] D. R. Otis, M. Johnson, T. J. Pedley, and R. D. Kamm. Role of pulmonary surfactant in airway closure: a computational study. *J. Appl. Physiol.*, 75(3):1323–1333, 1993.

[17] M. Griese. Pulmonary surfactant in health and human lung diseases: state of the art. *Eur. Respir. J.*, 13:1455–1476, 1999.

[18] J.-C. Baret. Surfactants in droplet-based microfluidics. *Lab Chip*, 12(3):422–433, 2012.

[19] P. Somasundaran and L. Zhang. Adsorption of surfactants on minerals for wettability control in improved oil recovery processes. *J. Pet. Sci. Eng.*, 52(1-4):198–212, 2006.

[20] S. Iglauer, Y. Wu, P. Shuler, Y. Tang, and W. A. Goddard. New surfactant classes for enhanced oil recovery and their tertiary oil recovery potential. *J. Petrol. Sci. Eng.*, 71:23–29, 2010.

[21] S. Rajaram. Global markets and advanced technologies for paints and coatings. *BCC Research*, (CHM049E):1–336, 2010.

[22] T. D. Blake. The physics of moving wetting lines. *J. Colloid Interface Sci.*, 299(1):1–13, 2006.

[23] E. Vandre, M. S. Carvalho, and S. Kumar. Delaying the onset of dynamic wetting failure through meniscus confinement. *J. Fluid Mech.*, 707:496–520, 2012.

[24] H. Benkreira. The effect of substrate roughness on air entrainment in dip coating. *Chem. Eng. Sci.*, 59(13):2745–2751, 2004.

[25] H. Benkreira and J. B. Ikin. Dynamic wetting and gas viscosity effects. *Chem. Eng. Sci.*, 65(5):1790–1796, 2010.

[26] E. Vandre, M. S. Carvalho, and S. Kumar. Characteristics of air entrainment during dynamic wetting failure along a planar substrate. *J. Fluid Mech.*, 747:119–140, 2014.

[27] O. Cohu and H. Benkreira. Entrainment of air by a solid surface plunging into a non-Newtonian liquid. *AIChE J.*, 44(11):2360–2368, 1998.

[28] W. L. Wilkinson. Entrainment of air by a solid surface entering a liquid/air interface. *Chem. Eng. Sci.*, 30(10):1227–1230, 1975.

[29] K. Miyamoto. On the mechanism of air entrainment. *Ind. Coat. Res.*, pages 71–88, 1991.

[30] G. F. Teletzke, H. T. Davis, and L. E. Scriven. Wetting hydrodynamics. *Revue Phys. Appl.*, 23(6):989–1007, 1988.

[31] E. Vandre, M. S. Carvalho, and S. Kumar. On the mechanism of wetting failure during fluid displacement along a moving substrate. *Phys. Fluids*, 25(10):102103, 2013.

[32] E. A. Vandre. *Onset of dynamic wetting failure: the mechanics of high-speed fluid displacement*. PhD thesis, University of Minnesota, 2013.

[33] S. Padmanabhan and A. Bose. The importance of direct measurement of dynamic contact angles during the wetting of solids by surfactant solutions. *J. Colloid Interface Sci.*, 126(1):164–170, 1988.

[34] O. V. Voinov. Hydrodynamics of wetting. *Fluid Dyn.*, 11(5):714–721, 1976.

[35] R. G. Cox. The dynamics of the spreading of liquids on a solid surface. Part 1. Viscous flow. *J. Fluid Mech.*, 168:169–194, 1986.

[36] Jens Eggers. Toward a description of contact line motion at higher capillary numbers. *Phys. Fluids*, 16(9):3491, 2004.

[37] J. H. Snoeijer. Free-surface flows with large slopes: Beyond lubrication theory. *Phys. Fluids*, 18(2):021701, 2006.

[38] P. G. Petrov and J. G. Petrov. A combined molecular-hydrodynamic approach to wetting kinetics. *Langmuir*, 8(7):1762–1767, 1992.

[39] J. H. Snoeijer and B. Andreotti. Moving contact lines: scales, regimes, and dynamical transitions. *Annu. Rev. Fluid Mech.*, 45:269–292, 2013.

[40] J. Eggers. Existence of receding and advancing contact lines. *Phys. Fluids*, 17(8):082106, 2005.

[41] Y Wei, E Rame, L M Walker, and S Garoff. Dynamic wetting with viscous Newtonian and non-Newtonian fluids. *J. Phys. Condens. Matter*, 21(46):464126, nov 2009.

[42] P. Gao and X.-Y. Lu. On the wetting dynamics in a Couette flow. *J. Fluid Mech.*, 724:R1, 2013.

[43] D. Bonn, J. Eggers, J. Indekeu, J. Meunier, and E. Rolley. Wetting and spreading. *Rev. Mod. Phys.*, 81(2):739–805, 2009.

[44] Y. D. Shikhmurzaev. Moving contact lines in liquid/liquid/solid systems. *J. Fluid Mech.*, 334:211–249, 1997.

[45] J. Lowndes. The numerical simulation of the steady movement of a fluid meniscus in a capillary tube. *J. Fluid Mech.*, 101(3):631–646, 1980.

[46] C. Huh and L. E. Scriven. Hydrodynamic model of steady movement of a solid/liquid/fluid contact line. *J. Colloid Interface Sci.*, 35(1):85–101, 1971.

[47] E. B. Dussan V. and S. H. Davis. On the motion of a fluid-fluid interface along a solid surface. *J. Fluid Mech.*, 65(1):71–95, 1974.

[48] E. B. Dussan V. The moving contact line: the slip boundary condition. *J. Fluid Mech.*, 77(4):665–684, apr 1976.

[49] E. B. Dussan V. On the spreading of liquids on solid surfaces: static and dynamic contact lines. *Annu. Rev. Fluid Mech*, 11:371–400, 1979.

[50] C. Neto, D. R. Evans, E. Bonaccurso, H.-J. Butt, and V. S. J. Craig. Boundary slip in Newtonian liquids: a review of experimental studies. *Rep. Prog. Phys.*, 68(12):2859–2897, 2005.

[51] E. Lauga, M. P. Brenner, and H. A. Stone. Microfluidics : the no-slip boundary condition. In J. Foss, Tropea C., and A. Yarin, editors, *Handbook of Experimental Fluid Dynamics*, pages 1219–1240. Springer, 2005.

[52] L. M. Hocking. A moving fluid interface on a rough surface. *J. Fluid Mech.*, 76(4):801–017, 1976.

[53] Y. Zhu and Granick S. Limits of the hydrodynamic no-slip boundary condition. *Phys. Rev. Lett.*, 88(10):106102, 2008.

[54] X. H. Zhang, X. D. Zhang, S. T. Lou, Z. X. Zhang, J. L. Sun, and J. Hu. Degassing and temperature effects on the formation of nanobubbles at the mica/water Interface. *Langmuir.*, 20(9):3813–3815, 2004.

[55] C. L. Henry, C. Neto, D. R. Evans, S. Biggs, and V. S. J Craig. The effect of surfactant adsorption on liquid boundary slippage. *Physica A*, 339(1):60–65, 2004.

[56] Y. Zhu and S. Granick. No-slip boundary condition switches to partial slip when fluid contains surfactant. *Langmuir*, 18(26):10058–10063, 2002.

[57] Yulii D Shikhmurzaev. Singularities at the moving contact line. Mathematical, physical and computational aspects. *Physica D.*, 217(2):121–133, 2006.

[58] H. Hu and R. G. Larson. Marangoni effect reverses coffee-ring depositions. *J. Phys. Chem. B*, 110(14):7090–7094, 2006.

[59] K. Y. Chan and A. Borhan. Surfactant-assisted spreading of a liquid drop on a smooth solid surface. *J. Colloid Interface Sci.*, 287(1):233–48, 2005.

[60] S. G. Yiantsios and B. G. Higgins. A mechanism of Marangoni instability in evaporating thin liquid films due to soluble surfactant. *Phys. Fluids*, 22(2):022102, 2010.

[61] U. Zoller. *Handbook of detergents, part E: applications*. Surfactant Science. CRC Press, 2008.

[62] M. Rieger and L. D. Rhein. *Surfactants in cosmetics*. Surfactant Science. Taylor & Francis, 1997.

[63] T. Stoebe, Z. Lin, R. M. Hill, M. D. Ward, and H. T. Davis. Surfactant-enhanced spreading. *Langmuir*, 12(2):337–344, 1996.

[64] T. D. Blake. Coating processes. US patent 5792515, 1998.

[65] Y.-M. Tricot. Surfactants: static and dynamic surface tension. In S.F. Kistler and P. M. Schweizer, editors, *Liquid Film Coating*, pages 99–136. Chapman & Hall, 1997.

[66] C. C. Ruiz, L. Diaz-Lopez, and J. Aguiar. Micellization of sodium dodecyl sulfate in glycerol aqueous mixtures. *J. Dispersion Sci. Technol.*, 29(2):266–273, 2008.

[67] Sabine Manet, Yevgen Karpichev, Dario Bassani, Roni Kiagus-Ahmad, and Reiko Oda. Counteranion effect on micellization of cationic gemini surfactants 14-2-14: Hofmeister and other counterions. *Langmuir*, 26(13):10645–10656, 2010.

[68] J. N. Israelachvili. *Intermolecular and Surface Forces*. Intermolecular and Surface Forces. Elsevier Science, 2011.

[69] C.-H. Chang and E. I. Franses. Adsorption dynamics of surfactants at the air/water interface: a critical review of mathematical models, data, and mechanisms. *Colloids Surf., A*, 100:1–45, 1995.

[70] O. E. Jensen and J. B. Grotberg. Insoluble surfactant spreading on a thin viscous film: shock evolution and film rupture. *J. Fluid Mech.*, 240:259–288, 1992.

[71] D. M. Campana and F. A. Saita. Numerical analysis of the Rayleigh instability in capillary tubes The influence of surfactant solubility. *Phys. Fluids*, 18(2):022104, 2006.

[72] C. W. Park. Effects of insoluble surfactants on dip coating. *J. Colloid Interface Sci.*, 146(2):382–394, 1991.

[73] J. Eastoe and J. S. Dalton. Dynamic surface tension and adsorption mechanisms of surfactants at the air - water interface. *Adv. Colloid Interface Sci.*, 85(2-3):103–144, 2000.

[74] S. Paria and K. C. Khilar. A review on experimental studies of surfactant adsorption at the hydrophilic solid-water interface. *Adv. Colloid Interface Sci.*, 110(3):75–95, 2004.

[75] M. D. Zeldes. Coating process employs surfactants. US patent 4508764, 1985.

[76] W. J. Knox. Photographic surfactant compositions. US patent 3514293, 1970.

[77] B. M. Deryagin and S. M. Levi. *Film coating theory: physical chemistry of coating.* The Focal Press, 1964.

[78] J. O. Marston, V. Hawkins, S. P. Decent, and M. J. H. Simmons. Influence of surfactant upon air entrainment hysteresis in curtain coating. *Exp. Fluids*, 46:549–558, 2009.

[79] P. R. Schunk and L. E. Scriven. Surfactant effects in coating processes. In S.F. Kistler and P. M. Schweizer, editors, *Liquid Film Coating*, pages 495–536. Chapman & Hall, 1997.

[80] H. A. Stone, A. D. Stroock, and A. Ajdari. Engineering flows in small devices: microfluidics toward a lab-on-a-chip. *Annu. Rev. Fluid Mech.*, 36(1):381–411, 2004.

[81] D. O. Shah and R. S. Schechter, editors. *Improved oil recovery by surfactant and polymer flooding.* Elsevier Science, 2012.

[82] S. J. Weinstein and K. J. Ruschak. Coating flows. *Annu. Rev. Fluid Mech.*, 36(1):29–53, 2004.

[83] C.-Y. Liu, E. Vandre, M. S. Carvalho, and S. Kumar. Dynamic wetting failure in surfactant solutions. *J. Fluid Mech.*, 789:285–309, 2016.

[84] D. Langevin. Rheology of adsorbed surfactant monolayers at fluid surfaces. *Annu. Rev. Fluid Mech.*, 46:47–65, 2014.

[85] R. G. Cox. The dynamics of the spreading of liquids on a solid surface. Part 2. Surfactants. *J. Fluid Mech.*, 168:195–220, 1986.

[86] M. S. Stay and V. H. Barocas. Coupled lubrication and Stokes flow finite elements. *Int. J. Numer. Meth. Fluids*, 43:129–146, 2003.

[87] M. K. Smith and G. P. Neitzel. Multiscale modelling in the numerical computation of isothermal non-wetting. *J. Fluid Mech.*, 554:67–83, 2006.

[88] G. Lavalle, J.-P. Vila, G. Blanchard, C. Laurent, and F. Charru. A numerical reduced model for thin liquid films sheared by a gas flow. *J. Comput. Phys.*, 301:119–140, 2015.

[89] S. Kumar and O. K. Matar. On the Faraday instability in a surfactant-covered liquid. *Phys. Fluids*, 16(1):39–46, 2004.

[90] E. Ramé. The spreading of surfactant-laden liquids with surfactant transfer through the contact line. *J. Fluid Mech.*, 440:205–234, 2001.

[91] R. V. Craster and O. K. Matar. Dynamics and stability of thin liquid films. *Rev. Mod. Phys.*, 81(3):1131–1198, 2009.

[92] E. B. Dussan V. The moving contact line: the slip boundary condition. *J. Fluid Mech.*, 77(4):665–684, 1976.

[93] T. S. Chan, S. Srivastava, A. Marchand, B. Andreotti, L. Biferale, F. Toschi, and J. H. Snoeijer. Hydrodynamics of air entrainment by moving contact lines. *Phys. Fluids*, 25(7):074105, 2013.

[94] D. N. Sibley, A. Nold, and S. Kalliadasis. The asymptotics of the moving contact line: cracking an old nut. *J. Fluid Mech.*, 764:445–462, 2015.

[95] A. Oron, S. H. Davis, and S. G. Bankoff. Long-scale evolution of thin liquid films. *Rev. Mod. Phys.*, 69(3):031–980, 1997.

[96] D. Jacqmin. Onset of wetting failure in liquidliquid systems. *J. Fluid Mech.*, 517:209–228, 2004.

[97] M. Sbragaglia, K. Sugiyama, and L. Biferale. Wetting failure and contact line dynamics in a Couette flow. *J. Fluid Mech.*, 614:471–493, 2008, arXiv:0812.3303v1.

[98] Y. Sui, H. Ding, and P. D.M. Spelt. Numerical simulations of flows with moving contact lines. *Annu. Rev. Fluid Mech.*, 46:97–119, 2014.

[99] Y. Sui and P. D.M. Spelt. Validation and modification of asymptotic analysis of slow and rapid droplet spreading by numerical simulation. *J. Fluid Mech.*, 715:283–313, 2013.

[100] R. Ledesma-Aguilar, A. Hernandez-Machado, and I. Pagonabarraga. Theory of wetting-induced fluid entrainment by advancing contact lines on dry surfaces. *Phys. Rev. Lett.*, 110(26):264502, 2013.

[101] D. Fell, G. K. Auernhammer, E. Bonaccurso, C. Liu, R. Sokuler, and H.-J. Butt. Influence of surfactant concentration and background salt on forced dynamic wetting and dewetting. *Langmuir*, 27(6):2112–2117, 2011.

[102] D. Fell, N. Pawanrat, E. Bonaccurso, H.-J. Butt, and G. K. Auernhammer. Influence of surfactant transport suppression on dynamic contact angle hysteresis. *Colloid Polym. Sci.*, 291(2):361–366, 2012.

[103] M. Anyfantakis, D. Fell, H.-J. Butt, and G. K. Auernhammer. Time-dependent dynamic receding contact angles studied during the flow of dilute aqueous surfactant solutions through fluorinated microtubes. *Chem. Lett.*, 41(10):1232–1234, 2012.

[104] A. Marchand, T. S. Chan, J. H. Snoeijer, and B. Andreotti. Air entrainment by contact lines of a solid plate plunged into a viscous fluid. *Phys. Rev. Lett.*, 108(20):204501, 2012.

[105] B. Tsai, M. S. Carvalho, and S. Kumar. Leveling of thin films of colloidal suspensions. *J. Colloid Interface Sci.*, 343(1):306–313, 2010.

[106] A. Q. Shen, B. Gleason, G. H. McKinley, and H. A. Stone. Fiber coating with surfactant solutions. *Phys. Fluids*, 14(11):4055, 2002.

[107] K. N. Christodoulou, S. F. Kistler, and P. R. Schunk. Advances in computational methods for free-surface flows. In Liquid Film Coating (ed. S. F. Kistler & P. M. Schweizer). Chapman & Hall, 297–367, 1997.

[108] P. Hood. Frontal solution program for unsymmetric matrices. *Int. J. Numer. Meth. Eng.*, 10:379–399, 1976.

[109] W. H. Press, S. A. Teukolsky, W. T. Vetterling, and B. P. Flannery. *Numerical recipes: the art of scientific computing*. Cambridge University Press, 3rd edition, 2007.

[110] H. Benkreira and M. I. Khan. Air entrainment in dip coating under reduced air pressures. *Chem. Eng. Sci.*, 63(2):448–459, 2008.

[111] J. E. Sprittles. Air entrainment in dynamic wetting: Knudsen effects and the influence of ambient air pressure. *J. Fluid Mech.*, 769:444–481, 2015, 1502.04571v2.

[112] O. K. Matar and R. V. Craster. Dynamics and stability of thin liquid films. *Rev. Mod. Phys.*, 81(3):1131–1198, 2009.

[113] N. Kumar, C. Maldarelli, and A. Couzis. An infrared spectroscopy study of the hydrogen bonding and water restructuring as a trisiloxane superspreading surfactant adsorbs onto an aqueous-hydrophobic surface. *Colloids Surf., A*, 277:98–106, 2006.

[114] B. Frank and S. Garoff. Origins of the complex motion of advancing surfactant solutions. *Langmuir*, 11(18):87–93, 1995.

[115] B. Bera, M. H. G. Duits, M. A. Cohen Stuart, D. van den Ende, and F. Mugele. Surfactant induced autophobing. *Soft Matter*, 12:4562–4571, 2016.

[116] C.-Y. Liu, E. Vandre, M. S. Carvalho, and S. Kumar. Dynamic wetting failure and hydrodynamic assist in curtain coating. *J. Fluid Mech.*, 808:290–315, 2016.

[117] T. D. Blake, J.-C. Fernandez-Toledano, G. Doyen, and J. De Coninck. Forced wetting and hydrodynamic assist. *Phys. Fluids*, 27(11):112101, 2015.

[118] O. E. Jensen and J. B. Grotberg. The spreading of heat or soluble surfactant along a thin liquid film. *Phys. Fluids A*, 5(1):58–68, 1993.

[119] A. Bose. Wetting by solutions. In John C. Berg, editor, *Wettability*, pages 149–181. Marcel Dekker, Inc., 1993.

[120] G. Karapetsas, R. V. Craster, and O. K. Matar. On surfactant-enhanced spreading and superspreading of liquid drops on solid surfaces. *J. Fluid Mech.*, 670:5–37, 2011.

[121] D. R. Beacham, O. K. Matar, and R. V. Craster. Surfactant-Enhanced rapid spreading of drops on solid surfaces. *Langmuir*, 25(24):14174–14181, 2009.

[122] D. M. Campana, S. Ubal, M. D. Giavedoni, and F. A. Saita. A deeper insight into the dip coating process in the presence of insoluble surfactants: A numerical analysis. *Phys. Fluids*, 23(5):052102, 2011.

[123] D. M. Campana, J. Di Paolo, and F. A. Saita. A 2-D model of Rayleigh instability in capillary tubessurfactant effects. *Int. J. Multiphase Flow*, 30:431–454, 2004.

[124] C.-H. Chang and E. I. Franses. Modified Langmuir-Hinshelwood kinetics for dynamic adsorption of surfactants at the air/water interface. *Colloids Surf.*, 69:189–201, 1992.

[125] L. Cantu, M. Corti, V. Degiorgio, H. Hoffmann, and W. Ulbricht. Nonionic micelles in mixed water-glycerol solvent. *J. Colloid Interface Sci.*, 116(2):384–389, 1987.

[126] N. Takisawa, M. Thomason, D. M. Bloor, and E. Wyn-Jones. Ultrasonic relaxation and electrochemical studies of the micellization of sodium decyl sulfate and decyltrimethylammonium bromide in glycerol/water mixtures. *J. Colloid Interface Sci.*, 157(1):77–81, 1993.

[127] B. A. Staggemeier, T. O. Collier, B. J. Prazen, and R. E. Synovec. Effect of solution viscosity on dynamic surface tension detection. *Anal. Chim. Acta*, 534:79–87, 2005.

[128] V. B. Fainerman, A. V. Makievski, and R. Miller. The measurement of dynamic surface tensions of highly viscous liquids by the maximum bubble pressure method. *Colloids Surf., A*, 75(6):229–235, 1993.

[129] C.-Y. Liu. *Onset of dynamic wetting failure in the presence of surfactants.* PhD thesis, University of Minnesota, 2017.

[130] N. J. Alvarez, D. R. Vogus, L. M. Walker, and S. L. Anna. Using bulk convection in a microtensiometer to approach kinetic-limited surfactant dynamics at fluid-fluid interfaces. *J. Colloid Interface Sci.*, 372(1):183–191, 2012.

[131] C. Cheikh and G. Koper. Stick-slip transition at the nanometer scale. *Phys. Rev. Lett.*, 91(15):156102, 2003.

[132] T. Sochi. Slip at fluid-solid interface. *Polym. Rev.*, 51(4):309–340, 2011, 1101.4421.

[133] C. Kunert and J. Harting. On the effect of surfactant adsorption and viscosity change on apparent slip in hydrophobic microchannels. *Prog. Comput. Fluid Dy.*, 8(1-4):197–205, 2008, 0610034.

[134] E. R. Swanson, S. L. Strickland, M. Shearer, and K. E. Daniels. Surfactant spreading on a thin liquid film: reconciling models and experiments. *J. Eng. Math.*, 94:63–79, 2015, 1306.4881.

[135] D. W. Fallest, A. M. Lichtenberger, C. J. Fox, and K. E. Daniels. Fluorescent visualization of a spreading surfactant. *New J. Phys.*, 12:073029, 2010, 0911.4160.

[136] T. D. Blake, R. Dobson, G. N. Batts, and W. J. Harrison. Coating processes. US Patent 5391401, 1995.

[137] T. D. Blake, R. A. Dobson, and K. J. Ruschak. Wetting at high capillary numbers. *J. Colloid Interface Sci.*, 279(1):198–205, 2004.

[138] T. D. Blake, M. Bracke, and Y. D. Shikhmurzaev. Experimental evidence of nonlocal hydrodynamic influence on the dynamic contact angle. *Phys. Fluids*, 11(8):1995–2007, 1999.

[139] M. Yamamura. Assisted dynamic wetting in liquid coatings. *Colloids Surf. A Physicochem. Eng. Asp.*, 311:55–60, 2007.

[140] M. Yamamura, S. Suematsu, T. Kajiwara, and K. Adachi. Experimental investigation of air entrainment in a vertical liquid jet flowing down onto a rotating roll. *Chem. Eng. Sci.*, 55(5):931–942, 2000.

[141] A. Clarke and E. Stattersfield. Direct evidence supporting nonlocal hydrodynamic influence on the dynamic contact angle. *Phys. Fluids*, 18(4):048106, 2006.

[142] S. P. Decent. A simplified model of the onset of air entrainment in curtain coating at small Capillary number. *Chem. Eng. Res. Des.*, 86(3):311–323, 2008.

[143] M. C. T. Wilson, J. L. Summers, P. H. Gaskell, and Y. D. Shikhmurzaev. Moving contact-line model and the effect of hydrodynamic assist of dynamic wetting. In A. C. King and Y. D. Shikhmurzaev, editors, *IUTAM Symposium on Free Surface Flows*, pages 345–352. Springer Netherlands, 2001.

[144] S. F. Kistler and L. E. Scriven. Coating flow theory by finite element and asymptotic analysis of the Navier-Stokes system. *Int. J. Numer. Meth. Fluids*, 4:207–229, 1984.

[145] J. Nam and M. S. Carvalho. Mid-gap invasion in two-layer slot coating. *J. Fluid Mech.*, 631:397–417, 2009.

[146] K. N. Christodoulou and L. E. Scriven. The fluid mechanics of slide coating. *J. Fluid Mech.*, 208:321–354, 1989.

[147] J. O. Marston, M. J. H. Simmons, and S. P. Decent. Influence of viscosity and impingement speed on intense hydrodynamic assist in curtain coating. *Exp. Fluids*, 42:483–488, 2007.

[148] M. S. Carvalho and L. E. Scriven. Flows in forward deformable roll coating gaps: comparison between spring and plane-strain models of roll cover. *J. Comput. Phys.*, 138(2):449–479, 1997.

[149] A. V. Lukyanov and Y. D. Shikhmurzaev. Effect of flow field and geometry on the dynamic contact angle. *Phys. Rev. E*, 75(5):051604, 2007.

[150] A. Clarke. The application of particle tracking velocimetry and flow visualization to curtain coating. *Chem. Eng. Sci.*, 50(15):2397–2407, 1995.

[151] J. O. Marston, S. P. Decent, and M. J. H. Simmons. Hysteresis and non-uniqueness in the speed of the onset of instability in curtain coating. *J. Fluid Mech.*, 569:349–363, 2006.

[152] H.-K. Chang, C.-J. Shih, T.-J. Liu, and C. Tiu. Curtain coating of dilute suspensions. *Polym. Eng. Sci.*, 52(1):1–11, 2012.

[153] M. J. Collins, R. A. Martin, and R. R. Stockl. Use of surfactants as plasticizers to reduce volatile organic compounds in water-based polymer coating compositions. US patent 6794434, 2004.

[154] G. Lu, X.-D. Wang, and Y.-Y. Duan. A critical review of dynamic wetting by complex fluids: from Newtonian fluids to non-Newtonian fluids and nanofluids. *Adv. Colloid Interface Sci.*, 236:43–62, 2016.

[155] X. Ding, T. F. Fuller, and T. A. L. Harris. A simulation model to approximate penetration of a non-Newtonian fluid into a porous media during slot die coating. *J. Coat. Technol. Res.*, 11(1):83–87, 2014.

[156] O.J. Romero, L.E. Scriven, and M.S. Carvalho. Slot coating of mildly viscoelastic liquids. *J. Nonnewton. Fluid Mech.*, 138(2-3):63–75, oct 2006.

[157] V. M. Starov, A. N. Tyatyushkin, M. G. Velarde, and S. A. Zhdanov. Spreading of non-Newtonian liquids over solid substrates. *J. Colloid Interface Sci.*, 257(2):284–290, 2003.

[158] S. Rafaï and D. Bonn. Spreading of non-Newtonian fluids and surfactant solutions on solid surfaces. *Physica A*, 358:58–67, 2005.

[159] Alain Carré and Pierre Woehl. Hydrodynamic behavior at the triple line of spreading liquids and the divergence problem. *Langmuir*, 18(9):3600–3603, 2002.

[160] Q. Min, Y. Y. Duan, X. D. Wang, Z. P. Liang, and C. Si. Does macroscopic flow geometry influence wetting dynamic? *J. Colloid Interface Sci.*, 362(1):221–227, 2011.